Lifetime prediction of high-performance fibre-reinforced polymer composites using Vibro-acoustic Modulation

Vom Promotionsausschuss der Technischen Universität Hamburg

zur Erlangung des akademischen Grades

Doktor-Ingenieur (Dr.-Ing.)

genehmigte Dissertation
(Monografie)

von
Erik Willmann

aus
Salzwedel

2025

Vorsitzender des Prüfungsausschusses:	Prof. Dr.-Ing. Benedikt Kriegesmann (Technische Universität Hamburg)
Gutachter:	Prof. Dr.-Ing. habil. Bodo Fiedler (Technische Universität Hamburg) Prof. Dr. rer. nat. habil. Marc Kreutzbruck (Universität Stuttgart)
Tag der mündlichen Prüfung:	28.02.2025

Technisch-Wissenschaftliche Schriftenreihe

Herausgeber:
Prof. Dr.-Ing. habil. Bodo Fiedler

Anschrift:
Technische Universität Hamburg
Institut für Kunststoffe und Verbundwerkstoffe
Denickestraße 15
21073 Hamburg

Band 48:
Lifetime prediction of high-performance fibre-reinforced polymer composites using Vibro-acoustic Modulation
DOI: https://doi.org/10.15480/882.15075

Erik Willmann
https://orcid.org/0000-0002-5757-3585

1. Auflage
Hamburg 2025

ISSN 2625-6029

Bibliographische Information der Deutschen Nationalbibliothek:
Die deutsche Nationalbibliothek verzeichnet diese Publikation in der Deutschen Nationalbibliothek; detaillierte Informationen sind im Internet über dnb.de abrufbar.

Acknowledgments

First and foremost, I would like to express my deepest gratitude to Prof. Dr.-Ing. habil. Bodo Fiedler, for his reliable support, guidance and encouragement throughout this research journey. His expertise, patience and insightful feedback have been invaluable in shaping both my academic growth and the development of this thesis.
Furthermore, I would like to thank Prof. Dr. rer. nat. habil. Marc Kreutzbruck for acting as the second assessor and Prof. Dr.-Ing. Benedikt Kriegesmann in his function of chairman. I am very grateful to all my colleagues at the Institute of Polymers and Composites for the very friendly working atmosphere and the many inspiring discussions. I would particularly like to acknowledge Jonas Drummer, Tobias Tiedemann, Benedikt Kötter, Dennis Gibhardt and Hans Wittich for the numerous scientific discussions and for providing both practical and moral support when needed most. The students I supervised, whose work contributed to the success of the research project, deserve my thanks.
I am deeply grateful to my parents Susanne and Klaus for their support, their trust and for their role model function. At the same time, I am pleased that I have also received support from my parents-in-law Katrin and Philipp. Finally, I would especially like to thank my wife Antonia for her patience, understanding and words of encouragement, which helped me to overcome many challenges.

Abstract

Fibre-reinforced polymer (FRP) composites are characterised by high density-specific stiffness and strength as well as high durability and corrosion resistance. However, the multi-scale and multi-phase structure of FRP also leads to a complex damage mechanism during operation. Any production deviation, such as voids or delaminations, negatively affects residual strength and service life. Monitoring the structural integrity during operation and quality assurance prior to operation is essential for reliable and safe use. Various approaches exist to detect damage at an early stage before failure-critical loads occur. This thesis investigates the applicability of vibro-acoustic modulation (VAM) as a damage detection method for carbon fibre reinforced polymer (CFRP) structures. VAM is a vibration-based non-destructive testing (NDT) method that employs high-frequency ultrasonic waves modulated as an introduced carrier signal by low-frequency vibrations with high amplitude. These modulations can be quantified and used to assess damage. In principle, the type of initiation of the low-frequency vibration can vary depending on the application, whereby the carrier signal is usually initiated by piezoceramic actuators. VAM offers great potential in large structures, especially due to its high sensitivity to cracks, simple measuring equipment, and long transmission paths. The complex – and thus well-known – material and damage behaviour of FRP is used in this work to develop a new test method using VAM. Various vibro-acoustic damage indicators are employed to predict the service life and degradation of FRP and to investigate the following research hypothesis:

Damage detection and determination of CFRP structures can be ensured through vibro-acoustic in-situ measurements, even retrospectively.

The VAM technique permits the monitoring of localised, concentrated damage in notched and impacted CFRP as well as statistically distributed damage in unnotched CFRP laminates. As evidenced by tensile and fatigue tests conducted under controlled conditions, the type and extent of damage could be identified from the VAM signal. Conventional measurement methods such as Acoustic Emission (AE), Ultrasonic testing (US), Digital Image Correlation (DIC) and X-ray analysis (XR) were also used to evaluate the VAM technique. In general, inter-fibre failures lead to an increase in modulation, accumulating over the service life to global delamination, which reduces modulation. Characteristic points, such as resulting damage-related VAM amplitude maxima, can be used for lifetime prediction. The sensitivity of the VAM method increases with increasing crack size. The linear correlation between the projected delamination area and the MI indicates that an estimation of the the impact damage has been achieved.

Artificially introduced defects such as PTFE films or contamination with release agent cannot initially be detected in scarfed (Sc) joints and single-lap shear (SLS) joints using VAM. To monitor the damage progression of the adhesive film due to permittivity changes, localised capacitance measurements of the adhesive film area can be used. An analytical model for determining crack length correlates with the VAM signal. The combination of both measurement methods demonstrated that, defects in Sc specimens with homogeneous stress distribution have a significant influence on the service life due to the resulting stress concentrations. In contrast, in SLS specimens, the stress concentrations at the overlap ends dominate the development of damage compared to the damage introduced, and thus do not affect the service life.

The results of this study demonstrate that the VAM method is a cost-effective in-situ technique for monitoring the structural integrity of CFRP structures. Implementation of the piezoceramic sensors required to introduce the carrier signal is simple and can be done on the surface, independent of the stress state of the structures. The influencing parameters, layer structure, and mechanical test procedures were adjusted, thereby facilitating enhanced comprehension of the measured signal and further advancement towards its implementation as a reliable NDT methodology.

Kurzfassung

Faser-Kunststoff-Verbunde (FKV) sind aufgrund ihres mehrphasigen und multiskaligen Aufbaus charakterisiert durch eine hohe dichtespezifische Steifigkeit und Festigkeit. Der multiskalige Aufbau von FKV kann jedoch auch während des jeweiligen Spannungszustandes im Betrieb zu einem komplexen Schadensmechanismus führen. Treten Fertigungsabweichungen wie z.B. Poren oder Delaminationen auf, beeinflussen diese negativ die Restfestigkeit und Lebensdauer. Demnach ist eine Überwachung der strukturellen Integrität während des Betriebs sowie eine Qualitätssicherung vor dem Betrieb für einen zuverlässigen und sicheren Einsatz unerlässlich. In der Literatur finden sich verschiedene vielversprechende Ansätze zur frühzeitigen Erkennung von Schäden vor versagenskritischen Belastungen. In dieser Arbeit wird die Anwendbarkeit der Vibro-akustischen Modulation (VAM) als Schadensdetektion an kohlenstoff-faserverstärkten Kunststoff-(CFK) Strukturen untersucht. Bei dieser schwingungsbasierten zerstörungsfreien Prüfmethode (engl.: non-destructive testing (NDT) method) werden hochfrequente Ultraschallwellen als eingeleitetes Trägersignal durch niederfrequente Vibrationen mit hoher Amplitude moduliert. Diese Modulationen sind quantifizierbar und dienen zur Schadensbewertung. Grundsätzlich kann die Art der Einleitung der niederfrequenten Schwingung je nach Anwendungsfall variieren, wobei das Trägersignal überwiegend durch piezokeramische Aktuatoren eingeleitet wird. Insbesondere durch ihre hohe Sensitivität gegenüber Rissen, lange Übertragungswege und einfaches Messequipment bietet die VAM ein hohes Potential in größeren Strukturbauteilen. Das komplexe, aber bekannte Material- bzw. Schädigungsverhalten von FKV wird in dieser Arbeit genutzt, um mittels VAM ein neues Prüfverfahren zu entwickeln. Dabei werden verschiedene vibro-akustische Schadensindikatoren genutzt, um die Lebensdauer und Degradation von FKV vorherzusagen und folgende Forschungshypothese zu untersuchen:

Die Detektion und Bestimmung von Schäden in CFK-Strukturen kann durch vibro-akustische In-situ-Messungen sogar nachträglich erfolgen.

Die VAM-Methode ermöglicht eine Überwachung lokaler, konzentrierter Schäden in gekerbtem und in schlagbelastetem CFK sowie von statistisch verteilten Schäden in ungekerbten CFK-Laminaten, was gestufte Zug- und Ermüdungsversuche zeigen. Durch eine systematische Variation des Lagenaufbaus konnte dem VAM-Signal die Art und der Umfang des Schadens zugewiesen werden. Zur Evaluierung der VAM-Methode wurden konventionelle Messverfahren wie Akustische Emissionsmessung (AE), Ultraschallaufnahmen (US), digitale Bildkorrelation-(DIC) und Röntgenmessungen (XR) herangezogen. Im Allgemeinen führen Zwischenfaserbrüche zum Anstieg der Modulation, die sich im Laufe der Lebensdauer zu globalen Delaminationen akkumulieren, welche die Modulation verringern. Charakteristische Punkte, wie z.B. resultierende, schadensbedingte VAM-Amplitudenmaxima, eignen sich zur Lebensdauervorhersage. Die Sensitivität der VAM-Methode steigt mit zunehmender Rissgröße. Die lineare Korrelation zwischen der projizierten Delaminationsfläche und des MI zeigt, dass das Maß der Schlageinwirkung abgeschätzt werden kann.

Künstlich eingebrachte Defekte wie PTFE-Folien oder Verunreinigungen mit Trennmitteln bei geschäfteten Klebeverbindungen (engl.: Scarfed (Sc) joints) und einfach überlappender Klebung (engl.: Single-lap shear (SLS)) bleiben mit VAM undetektiert. Anhand von lokalen Kapazitätsmessungen des Klebefilms lässt sich der Schadensverlauf des Klebefilms aufgrund von Permittivitätsänderungen überwachen. Ein analytisches Modell zur Risslängenbestimmung korreliert dabei mit dem VAM-Signal. Die Kombination beider Messmethoden zeigt, dass Defekte in Sc-Strukturen aufgrund der resultierenden Spannungskonzentrationen signifikant die Lebensdauer verringern. Konstruktionsbedingte Spannungskonzentrationen an den Überlappungsenden von SLS-Strukturen dominieren die Schadensinitiierung gegenüber eingebrachter Defekte, sodass die Lebensdauer nicht beeinflusst wird.

Die Ergebnisse dieser Arbeit zeigen, dass die vorgestellte VAM-Methode ein kostengünstiges In-situ-Verfahren zur Überwachung der strukturellen Integrität von CFK-Strukturen darstellt. Eine einfach Implementierung der zur Einleitung des Trägersignals notwendigen piezokeramischen Sensoren ist auf der Oberfläche möglich und unabhängig vom Spannungszustand der Strukturen gegeben. Anhand der Variation von Einflussparamtern, Lagenaufbau und mechanischer Testverfahren konnte das grundsätzliche Verständnis hinter den gemessenen Signal verbessert und ein weiterer Fortschritt in Richtung des sicheren Einsatz als zuverlässige Prüfmethode erzielt werden.

Contents

List of Abbreviations

AE	Acoustic emission
AM	Amplitude modulation
BVID	Barely visible impact damage
CAI	Compression after impact
CFRP	Carbon-fibre reinforced polymer
CT	Computer tomography
CP	Cross-ply
DIC	Digital image correlation
FAI	Fatigue after Impact
FAW	Fibre areal weight
FBG	Fibre Bragg grating
FCF	Finite cycle fatigue
FEM	Finite element method
FFT	Fast Fourier Transform
FOS	Fibre optic sensor
FRP	Fibre-reinforced polymer
FVC	Fibre volume content
GFRP	Glass-fibre reinforced polymer
HCF	High cycle fatigue
LCF	Low cycle fatigue
LVI	Low-velocity impact
MI	Modulation index
NAM	Non-linear acoustic modulation
NDT	Non-destructive testing
NTPT	North Thin Ply Technology
OHT	Open-hole tension
PM	Phase modulation
PTFE	Polytetrafluoroethylene
QI	Quasi-isotropic
RA	Release agent
SC	Scarfed joints
SHM	Structural health monitoring
SLS	Single lap shear
UD	Unidirectional
US	Ultrasonic
VAM	Vibroacoustic modulation
XR	X-Ray

1 Introduction

High-performance fibre reinforced polymers (FRP) find application in various fields, including aerospace, automotive, maritime, and sports equipment, where high weight-specific strength and stiffness are necessary. The damage behaviour of these composites, which includes matrix cracks, delamination, and fibre breakage, is typically complex and dependent on factors such as layer structure, load condition and material selection. Even when subjected to low static or cyclic loading, the matrix's low strength causes failure between the fibres. This failure typically occurs in the 90° layers that are orthogonal to the direction of loading. With increasing crack length and the associated stress maxima at the crack tip, delamination occurs, leading to a significant reduction in stiffness and service life [1–3]. Other types of damage, such as impact events caused by Foreign Object Damages (FODs) on aircraft components during ground handling and in the air, often cause damage that is not easily visible on the surface. Resulting delamination, inter-fibre failure and fibre failure, however, increase in the thickness direction and significantly reduce the residual strength and service life [4–7].

To improve the mechanical properties of carbon fibre reinforced polymers (CFRP), reducing the layer thickness is a viable strategy. This is achieved by producing a 'thin layer' using a spreading process that enhances the homogeneity of the fibre distribution and the quality of the prepreg. The failure mechanisms of CFRP depend heavily on the thickness of the layers. A thinner layer suppresses the formation of microcracks in the transverse direction and the delamination of the free edge at lower stresses, resulting in increased transverse tensile strength (in-situ effect). Under high stress conditions, thinply laminates exhibit significantly higher crack densities than thickply laminates. By reducing the layer thickness, the failure mode changes from a complex failure dominated by delamination to a brittle failure [8–12]. The reduced layer thickness and the resulting increase in the amount of layers while remaining the same laminate thickness allows more freedom in the directional design of the composite materials and can increase the service life of the components. The fastening of large composite structures or the repair of structural components typically involves welding, bolting, or riveting [13–19]. However, these conventional joining techniques often add additional weight to account for high local stress concentrations. Therefore, it is important to consider these effects when determining the service life of the structure. These stress concentrations, in combination with complex damage behavior and failure events, can lead to a variety of effects that are not observed with unnotched laminates. Bonded joints do not require a reduction in the load-bearing cross-section, which avoids notch effects and stress concentrations through uniform stress distribution. Due to the manufacturing process, however, porosities, cavities, adhesion-reduced areas or matrix cracks, for example, or high temperatures or the leakage of a hydraulic fluid due to operation, stress concentrations and a reduced service life can occur. [20, 21].

Especially in the efficiency-driven aircraft industry with high safety standards, it is crucial to detect and accurately assess any damage that could compromise structural integrity or increase required service intervals. A dependable in-service non-destructive testing methodology is essential for predictive maintenance, enabling the unambiguous assessment of structural integrity, including remaining useful life, for all technical applications. Transferring non-destructive testing methods from the laboratory to an industrial scale can be a time-consuming process, particularly for applications with high safety factors.
Irrespective of the application, radiographic testing is the most commonly used test method [22], which can be used to detect inter-fibre breaks, delaminations and fibre breaks within the fibre composite with high resolution. However, it can be expensive and slow, and cannot be performed during operation. Thermographic testing is a commonly used method, but it has a serious reliability issue: it cannot detect defects that are too deep below the surface of the component. Non-linear ultrasonic methods are particularly effective in achieving high sensitivity in the detection of small defects with a high sampling rate and the possibility of use during operation [23]. Vibro-acoustic modulation is a promising testing method based on the modulation of highly sensitive ultrasonic waves as high-frequency carrier excitation by the low-frequency pump vibration. The detection of damage can be achieved through various methods depending on the field of application and the type of damage. The incorporation of sensors into the material does not mechanically affect the component. One common research-related method involves introducing high-frequency ultrasonic waves through piezoceramic actuators and low-frequency vibrations using a servo-hydraulic tes-

ting machine. Due to the simple test setup compared to conventional non-linear methods, this method can be classified as cost-efficient [24, 25]. The damage state is characterised by evaluating the time and frequency range of the complex response signal modulation.

1.1 Aims and Scope

Some state-of-the-art measuring techniques, like acoustic emission, need to operate during damage-inducing events, e.g. Impacts, or require a baseline measurement, as is the case of electrical resistance methods. However, this means discontinuous damage measurements are not available at specified intervals. In this instance, the VAM method can be used both continuously and discontinuously and has already proven to be very sensitive in a series of research studies, including the detection of fatigue damage in metals and the detection of impact damage in composite materials [26–31]. However, predicting the structural behavior and resulting maintenance of technical components requires knowledge of both the damage behavior and the non-destructive testing methodology used. Consequently, this thesis concerns the further development of the VAM method based on the known material behaviour, with the objective of predicting the service life and degradation of FRP. Accordingly, the following global, central research hypothesis is analysed in the context of this thesis:

Damage detection and determination of CFRP structures can be ensured through vibro-acoustic in-situ measurements, even retrospectively.

Quality assurance over the entire product life cycle is essential for the sustainable and reliable operation of FRP composites. This requires routine checks at defined intervals to verify structural integrity before damage propagation reaches a critical level. Increased attention is paid to components with impact events such as tool drop, bird strike or disintegrated tyres, or structures that have already been repaired due to these events. To ensure the application of VAM in CFRP structures for different stress states in the tensile and compressive range, the influencing parameters of low-frequency vibration are first analysed on undamaged unidirectional (UD) CFRP laminates. The results of these investigations serve as the basis for the other sections. In stepwise-tensile tests, crossply (CP) and notched quasi-isotropic (QI) laminates with varying layup are analysed in order to detect statistically distributed damage as well as locally concentrated damage. As a logical further development, the correlation of the VAM signal of impacted test specimens with the extent of the locally concentrated impact damage is investigated. For this purpose, the geometry, the ply thickness, the impact energy and the low-frequency introduction are varied. The adhesion of bonded joints significantly influences the mechanical performance and is characterised by a variety of influencing parameters, including surface treatment. Accordingly, the detection of contamination or foreign particles, which reduce the effective bonding surface and thus the adhesive strength, is essential. For this purpose, CFRP bonded joints are provided with contaminants such as PTFE film and release agent, which are quite common in production, in order to investigate the applicability of the VAM for initial testing. These approaches are intended to verify the second working assumption:

1. Vibro-acoustic modulation allows early detection of defects in CFRP structures, providing a wide range of quality control applications for CFRP.

In fatigue tests, the local and global damage propagation over the service life is evaluated using VAM. For this purpose, the layer structure and geometries of the CFRP laminates are systematically varied to investigate the influence of changing damage mechanisms on the time and frequency domain. This involves varying the individual layer thickness of unnotched and notched test specimens, monitoring the impact behaviour under fatigue, as well as CFRP bonded joints with artificially introduced defects. For this purpose, the characteristic progressions of vibro-acoustic damage indicators are analysed in order to verify the following working assumption:

2. The remaining service life of CFRP structures can be predicted based on different vibro-acoustic damage indicators.

1.2 Thesis Outline

This dissertation is divided into following sections: Subsequent to the introduction, the state of the art chapter summarises carbon fibre reinforced polymer structures and their damage behavior in general as well as presenting an overview of existing structural health monitoring methods including vibro-acoustic modulation. Chapters 3 and 4 provide information on the materials used, manufacturing and testing methods, and specimen geometries on which the specific standard is based. The special features of the VAM measurements in relation to the specific mechanical test methods are explained. The subsequent chapter presents and discusses the results that verify the research hypothesis outlined above. To evaluate VAM and cover a wide range of applications, the laminate structure and damage mechanisms of CFRP laminates are systematically varied. The analysis focuses on detecting defects within bonded joints and impact damage, whether they are manufacturing or operational defects. The monitoring of mechanical connecting elements, such as adhesive joints and bolt connections, is achieved through the manufacture and fatigue testing of scarfed and single lap shear joints, as well as open-hole tension (OHT) laminates. The final chapter draws conclusions and provides an outlook for further research topics. Extracts of this thesis have previously been published in journal articles [32–34]

2 State of the Art

2.1 Carbon fibre reinforced polymers

CFRPs are often used in numerous high performance light-weight structures in e.g. aerospace or automotive equipment , where high density specific strength and stiffness are required. These properties are derived from their multi-scale nature, consisting of high-strength carbon fibres integrated in a polymer system. Primary functions of the polymer matrix are to ensure load transfer between the fibres, fixing the fibres, providing support in compression and preventing the fibres from external influences including chemicals or environmental conditions [35, 36]. The fibres in this context represent the load-bearing component, which consist of individual graphite layers containing carbon atoms connected by covalent bonds. Considerably weaker Van der Waals forces connect the graphite layers orthogonally to the fibre direction, which leads to anisotropic material properties in carbon fibres. Continuous fibre-reinforced polymers used in structural elements typically consist of stacked, unidirectional (UD) layers. The sequence and fibre orientation are adjusted according to the main load alignments to compensate for the anisotropy of each layer [37]. This thesis used UD prepregs are pre-impregnated fibres with an epoxy matrix and partially cross-linked using several hardeners. The design of FRPs must take into account the resistance against damages, which will vary depending on the structure geometry and the load direction in the plane of the structure. Laminate structure, layer thickness, stacking sequence, fibre volume content and the quality of the fibre-matrix interface are some of the most important influencing parameters [35, 38, 39]. The transversal strength of a single UD layer and the shear strength of the laminate increases significantly as the layer thickness decreases [10, 40–42]. Damage propagation within the matrix is reduced by neighbouring individual layers, which decrease the available elastic energy (in-situ-strength) [9, 43, 44].

2.2 Damage mechanisms of fibre reinforced polymers

Due to their multi-scale nature and various constituents, failure behaviours of composite materials are complex. Generally, composites are characterised by a brittle behaviour, whereby fatigue and high static loads can lead to sudden failure. According to [45, 46] the type of damages that occur in composite materials can be classified into four main types, each with increasing severity: micro-cracks, inter-fibre fracture, delamination and fibre fracture. Inter-fibre fractures are transverse cracks that can be caused by either matrix failure or fibre-matrix detachment [35, 47]. The origin and extent of these kind of damages will be discussed below.

A damage process at low mechanical stresses and thermally induced stresses typically involves the formation of micro-cracks within the matrix as cohesive failure or at the interface between the matrix and fibre as adhesive failure [48, 49]. Occurring defects or flaws favour the formation of micro-cracks. However, it should be noted that strength and stiffness are not significantly affected by micro-cracks. As static and/or fatigue load increases, these cracks grow on a macroscopic level, which are then referred to as inter-fibre fractures. Inter-fibre fractures typically occur in the individual layers whose fibre orientation differs from the load direction and are prevented to propagate in a multi-layer FRP by adjacent layers with different fibre orientations. Additionally, stress concentrations form in regions where inter-fibre fractures are localised and no force transmission exists as well. A stress redistribution to adjacent layers occurs. As a consequence, microscopic cracks are characterised by a significant reduction in stiffness [50–52]. High interlaminar shear stresses occur between the individual layers as a result of stress redistribution. If the applied stress exceeds the inter-laminar interface strength, the cracks expand over a large area between the individual layers, an effect known as delamination [53]. Delamination frequently occurs at free edges due to inter-laminar stresses and is one of the most critical types of damage in FRP. Edge delamination not only results in a significant loss of strength and stiffness but also complicates and affects the mechanical characterization typically at long test specimens. Several studies have addressed the prevention of edge delamination under loads. This can be achieved by modifying the laminate through ply substitutions [54, 55] or by local modifications to the material or geometry at the free ends [56–61]. Delaminated FRP subjected to compressive stress tend to buckle due to the reduced bending stiffness and inability of the matrix to absorb the compressive forces [45, 49]. Ultimate failure occurs by fibre fracture when the applied mechanical stress exceeds the fibre strength in cases where the fibre orientation is parallel to the load direction. In the case of compressive stress, kinking induced by bending can also lead to fibre breakage. The first to fail are fibres and filaments with defects or fibre angle deviations, which can result from the manufacturing processes. The stresses are then redistributed to adjacent fibres. Finally, entire fibre bundles fail, culminating in catastrophic failure. In the case of a longitudinal compressive load, the fibres may buckle micro-mechanically, known as shear buckling due to the low shear stiffness [62]. In most cases, however, there is a loss of stability of the structure itself or inter-fibre failure occurs before the development of micro-mechanical shear buckling within individual UD layers. Micro buckling in-phase causes the formation of a kink band with increasing load [63]. The high stiffness difference between the fibre and matrix can cause stress concentrations at the interface, leading to adhesive detachment of the matrix from the fibre [35, 36].

2.2.1 Damage mechanism under low-velocity impact

The inferior compression performance of FRP has been a major obstacle to wider application and a limitation in design since its introduction [64]. According to [65], the compressive strength of carbon fibres and carbon fibre composites is approximately 30 to 50% of their tensile strength. The micro-structure of the fibres primarily controls the degradation of properties, while the compressive strength of the composite depends on the manufacturing processes, laminate structure, voids [66–73] and other process-related defects like fibre misalignment [68, 70, 74, 75]. Operation-related defects, such as impact damage, may occur in typical applications of CFRP, such as wind turbine rotor blades or outer skin elements of airplanes. Hazards may include hail, birds, falling tools during maintenance or collisions with ground equipment. Impact damage is a critical exposure for CFRP due to the complex formation of inter-fibre breaks, delaminations, and fibre breaks caused by the energy applied [7, 76]. The low-velocity impact type, defined by an impact velocity of 10 to 20 m/s [77, 78], is used in this study. The damage at the entry point of the laminate surface is concentrated at a small area and is classified as either visible or barely visible impact damage based on visibility. However, it is difficult to estimate the residual compressive strength and fatigue behaviour because the damage is much more pronounced along the thickness direction. As shown in Fig. 2.1, the propagation of inter-fibre breaks, fibre breaks and delaminations as a damage shape along the thickness in multi-layer

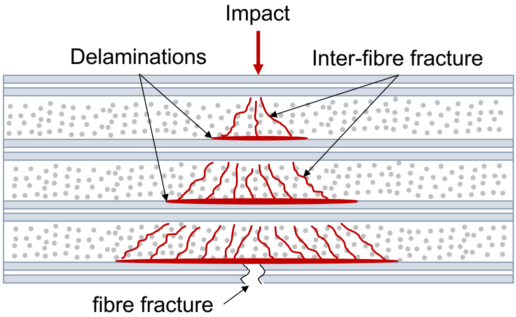

Figure 2.1: Schematic representation of low-velocity impact damage in a CFRP laminate. Resulting fibre breaks, inter-fibre breaks and delaminations are indicated in red.

laminates typically resembles the contour of a pine tree. The stress distribution of an impact damaged component is similar to a bending test, regardless of material. Thus, the entry surface experiences the highest compressive stresses, while the opposite laminate surface has the highest tensile stresses, resulting in inter-fibre fractures. Delamination occurs when the applied stress exceeds the inter-facial strength between the layers [35, 79]. High stress gradients also occur when the stiffness difference between the layers is particularly large, as is the case with 0 and 90° layers, which favour delaminations. The amount and size of inter-fibre fractures and delaminations increase as the distance from the entry point increases. If the maximum applied stresses exceed the strength of the fibres, the fibres will break on the back side. From a design perspective, compensating for the impact of FRP can be challenging. To reduce these stress concentrations, metal layers [80] or toughening thermoplastic particles in prepreg systems are used [81, 82].

2.2.2 Damage mechanism of notched laminates

The mechanical fastening of large composite structures by conventional joining techniques (e.g. welding, fastening and riveting [13–19]), is accompanied by additional weight to account for the high local stress concentrations. These stress concentrations in combination with complex damage behaviour and failure events result in a variety of effects that are not observed in unnotched laminates. The mechanical properties were shown to be influenced by laminate thickness,

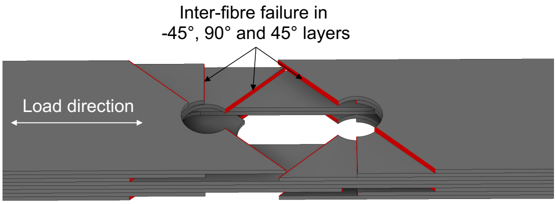

Figure 2.2: Schematic representation of the damage mechanism of notched composite laminates. Resulting inter-fibre failure in the -45°, 90° and 45° layers are indicated in red.

lay-up structure, notch size, processing quality and specimen width [83–85] and determines whether the failure is delamination- or fibre-dominated. A general schematic overview of the damage mechanism of notched specimens is shown in Fig. 2.2. Nixon et al. [86] and Green et al. [87] showed that in quasi-isotropic laminates with a commonly used layer thickness of 125 µm the initial crack of the matrix in the ±45° and 90° layers begins to propagate from the hole and leads to dominant delaminations at the layer interfaces throughout the specimen. Within the 0° layers splitting can initiate, which, coupled with delaminations at the hole, reduce the stress concentration as a blunting mechanism and prevent premature failure [87–89]. Decreasing the layer-thickness in open-hole tension (OHT) specimens converges the failure mode from a complex delamination-dominated failure to a brittle one [90]. Generally, reducing the layer thickness suppresses microcracking in the transverse direction and free edge delamination, which in contrast results in a decreased OHT strength [91–93]. Inter-laminar damage, such as delamination, does not cause crack weakening. Consequently, stresses at the notch cannot be redistributed to adjacent layers, leading to premature failure [8, 9, 94].

2.2.3 Damage mechanism under fatigue loading

The fatigue behaviour of FRP differs significantly from its behaviour under static loading – varied by the stress ratio, layer structure, and selection of material [95]. Regarding reliable and continuous structural monitoring, these present challenging peculiarities that differ significantly from the fatigue behaviour of metals. FRPs typically exhibit complex damage mechanisms that nucleate, accumulate and ultimately fail through partial micro-damage [35, 96]. These mechanisms interact with various damage initiation and propagation mechanisms [97–100]. A comparison between the typical degradation processes of FRP and metals is shown in Fig. 2.3. The damage D increases with the number of fatigue cycles N in proportion to the relative stiffness E/E_0 [52]. The development of degradation in FRP can typically be divided into three areas, which can be described by the Paris law [101]. The crack growth rate is related to the amount of energy released [102]. Damage initiation depends on how long a crack needs to grow to visible size. The initial area is characterised by the presence of micro-cracks along the fibre-matrix interface, with deviations in fibre parallelism to the load direction (e.g. 90° or 45°), within the matrix parallel to the fibre orientation, imperfections, and pre-damaged fibre breaks. Assuming a reproducible and high-quality production process, the 2-5% increase in damage is relatively low. The damage curve develops linearly in the second phase. Delaminations caused by inter-laminar shear stresses increase in number and size, while crack saturation occurs at the inter-fibre breaks [100]. Additionally, longitudinal cracks that are nearly irrelevant to stiffness occur in the 0° layers due to the transverse contraction hindrance of adjacent layers with deviating fibre orientation [50]. The initial fractures of fibres or filaments occur due to stress concentration along the crack flanks. The layers remaining at 0° are subjected to the highest load. During the third phase, the damage curve increases exponentially until the final failure occurs. The pronounced delamination, which is distributed over several layers, prevents a homogeneous and reliable stress distribution within the multi-layer composite. Furthermore, additional delaminations, transverse and longitudinal cracks occur. The stresses concentrate around the longitudinal fibres until individual fibre bundles tear. Then, the stresses distribute to adjacent fibre bundles until ultimate failure occurs. Typically, more than 50% of the damage occurs in the first 20% of the service life, whereas in metals, cracking starts with the onset of dislocation movement at more than 75% of service life [103]. Accordingly, the moment at which structural integrity is assessed by inspection is clearly differentiated. The type of damage in fibre composites is relevant, complicating inspection, whereas only the presence of damage is critical in metals. Under tensile-compressive loading, the degradation curves show a steeper increase in the second phase due to the buckling of the outer layers near the delaminations and the growth of the delaminations caused by transverse cracks under compressive loading [50, 95, 104]. Due to the combination of tensile and compressive loads, degradation is more pronounced and spreads more rapidly, resulting in earlier failure at a comparable load level [105–107]. Cyclic compressive loads are

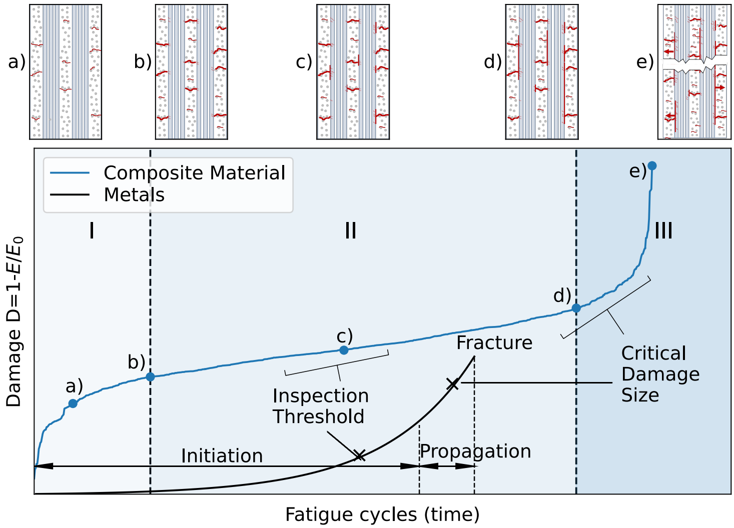

Figure 2.3: Schematic representative comparison of the damage behaviour of metals and a FRP cross-ply laminate under fatigue loading including composite specific damage mechanisms: a) micro-cracks within the matrix and fibre-matrix interface; b) Propagating cracks and transversal cracks as well as a minor amount of filament failures in the 0° layers due to stress redistribution; c) and d) Increasing and accumulating delaminations between the individual layers due to shear stresses; f) failure of fibre bundles until final failure

particularly critical for impacted samples, as buckling can occur during the first few cycles due to insufficient (matrix) stability and degradation is accelerated [4, 108–113]. In contrast, impacts have no significant effect on the service life or damage behaviour of specimens under pure tensile loading provided no fibre fracture has occured [108]. In the alternating tensile-compression load condition, the accumulation of damage is more pronounced due to the combination of buckling under compressive load and the opening of inter-fibre fractures under tension. Delamination development and propagation in tension can lead to compression buckling [113–116]. The amount of applied impact energy has a significant influence on the service life.

The service life of a component is typically represented in an S-N curve as a function of the load. When a specimen fails, the corresponding stress amplitude is plotted across the number of cycles to failure. The low cycle fatigue (LCF) range exceeds a load limit at which damage occurs. In the so-called finite life fatigue (FLF) range, there is an ever decreasing number of load cycles with increasing load until failure. This range is a straight line on a double logarithmic scale. Above a certain load, the range of high cycle fatigue (HCF) limit begins. From here on, the service life of the component is independent on the number of load cycles. According to the following Palmgren-Miner relationship [117, 118], the number of load cycles N at applied stress σ can be calculated as a function of the number of cycles above endurance limit $\mathrm{N_D}$, the applied stress above endurance limit σ_D and the fatigue strength exponent k :

$$\mathrm{N} = \mathrm{N_D}\left(\frac{\sigma}{\sigma_\mathrm{D}}\right)^{-k}; \sigma = \sigma_\mathrm{D}\left(\frac{N_D}{\mathrm{N}}\right)^{\frac{1}{k}} \tag{2.1}$$

2.2.4 Thinply carbon fibre reinforced polymers

Composites are known to exhibit a size effect, which refers to a change in strength with specimen dimensions [119]. As the volume decreases, e.g. due to thinner specimens or layers, the probability of defects within the specimen as damage initiation statistically decreases, and thus the strength increases [120]. According to linear elastic fracture mechanics (LEFM), the strength of a structure is inversely proportional to the square root of the crack length. In FRP, intralaminar cracks are the primary cause of damage and failure. These cracks are stopped by adjacent layers with different fibre orientations, resulting in a maximum crack length equivalent to the thickness of the individual layer. To enhance the mechanical properties of CFRP, one strategy is to decrease the thickness of each layer regarding the size effect. These kinds of layers are called *thinply*, typically defined as layer thicknesses below 100 µm, and are produced by a spreading process, which increases the fibre distribution homogeneity and, respectably, the quality of the prepreg. Layer thicknesses up to 18 µm are commercially available [9]. Increased design variety and more accurate layup design based on load dependency are benefits of using a thinner layer [9, 44, 121–123].

Failure mechanisms of Thinply composites

The layer thickness significantly influences the failure behaviour of CFRP. Reduced layer thickness suppresses micro-cracking in the transverse direction and free edge delamination resulting in increased transverse tensile strength (in-situ effect) [10] and compressive strength for unnotched quasi-isotropic thinply laminates [8, 9, 124]. Decreasing the layer thickness changes the failure mode from a complex delamination dominated one towards a brittle failure [8–12], which is further explained in Fig. 2.4. Thinply structures exhibit visible micro-cracks, while thickply structures with a low number of fatigue cycles produce a small number of large inter-fibre fractures. An increase in transverse tensile strength causes inter-fibre fractures to occur at higher levels of stress. However, this results in higher crack density. The phenomenon of in-situ effect is observed when transverse layers are supported by adjacent layers with different fibre orientations, resulting in higher transverse tensile or shear strength. This effect is exponentially increased with decreasing layer thickness and increasing stiffness of the neighbouring layers [40, 42, 125–130].

As the number of fatigue cycles increases, inter-fibre fractures in thickply structures increase, leading to delamination between the layers caused by high inter-laminar shear stresses. In contrast, in thinply structures, the first inter-fibre breaks occur, and the inter-laminar shear stress is lower due to the shorter crack length. Starting from the existing inter-fibre breaks, no delaminations can form. However, further breaks occur, resulting in an increase in crack density and a decrease in the distance between individual cracks [9, 10, 131]. Delamination clearly dominates the failure of thickply structures. The number and size of delaminations increase with fatigue cycles, leading to the separation of individual layers or even layer composites. In thinply structures, the crack density continues to grow and the 0° layers remain supported until a certain point in their service life, after which the material suddenly fails.

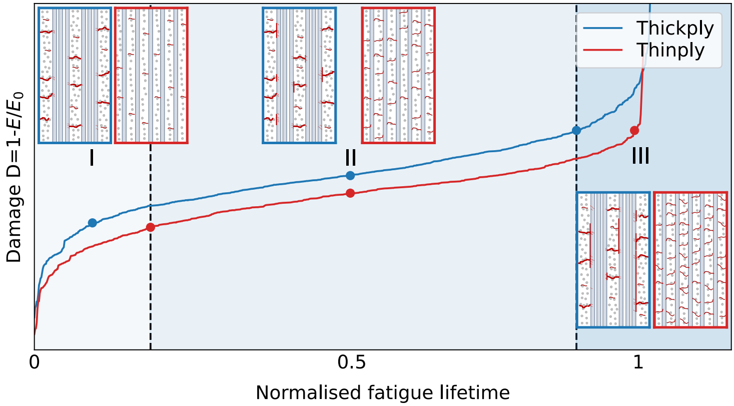

Figure 2.4: Schematic representation of the failure mechanism of Thickply (blue framed) and Thinply (red framed) composites under tensile fatigue load. Red lines indicate inter-fibre fractures and delaminations.

2.3 CFRP adhesive joints

2.3.1 Adhesion and cohesion

The strength of an adhesive bond is limited by the individual strength of the joining component, the adhesive layer or its interface. Within an adhesive bond, the bonding forces are divided into the strength of the adhesive-joint inter-facial contact (adhesion force) and the adhesive layer strength (cohesive force) [132, 133]. Adhesive bonds are based on a variety of mechanisms, which can be categorised as follows: specific adhesion, mechanical adhesion, and autohesion. Specific adhesion is based on physical, chemical, and thermodynamic principles, and the effects of these are interrelated. Mechanical adhesion is based on a inter-locking bonding force through the spreading and hardening of the liquid adhesive in pores, capillaries, and cavities. Autohesion, on the other hand, refers to the attraction forces at the boundary layer between two identical polymers. Cohesion refers to the intermolecular forces within a material and is based on the attraction and repulsion forces between atoms or unsaturated molecules, which are categorised into van der Waals forces and hydrogen bonds. These attractive forces are held together by primary and secondary valence bonds.

The typical failure modes are categorised into adhesive and cohesive failure and their mixed forms (see Fig. 2.5). Cohesive failure typically occurs within the

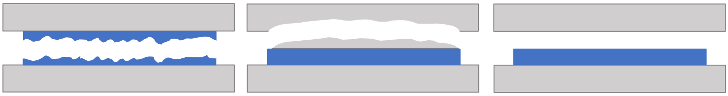

Figure 2.5: Schematic representation of the failure mechanism of bonded joints: Cohesive failure in the adhesive layer (left), cohesive failure in the adherend (center) and adhesive failure (left)

adhesive layer, leaving residues on both adherends. Cohesive failure within the adherends typically occurs at high stress concentrations or adherend strength. Adhesive failure at the interface between the adhesive and the adherend can be attributed to a number of factors, including incompatible surface chemistry, inadequate bond formation due to insufficient surface pre-treatment, and the presence of foreign substances such as grease or dust particles.

2.3.2 Surface treatment

The treatment of a bonded part's surface has a significant impact on the adhesion of the interface between the adhesive and the adherend. Finally, the surface is treated in further stages. Kaliske et al.[134] divide the surface treatment into three steps. Firstly, the joining parts are cleaned by grinding to remove solid layers such as grime, paint or production-related release agent through mechanical abrasion [135, 136]. Des weiteren eignen sich die Laservorbehandlung oder die Ätzung As a result of the polymer chains disrupting, a reactive surface is created [137] with a higher oxygen content and greater roughness than a untreated surface or cleaned with solvents [137–141]. The improvement in roughness and oxygen, as well as the removal of contaminants, contributes to the improved wetting observed in contact angle measurements [138, 140–142]. However, it is important to prevent damage to the fibres in order to maintain joint strength. Secondly, the parts are degreased using a solvent in order to remove microparticles and contamination caused by grinding. Methyl ethyl ketone (MEK), acetone or isopropyl alcohol (IPA) are commonly used solvent liquids [143]. In the second step, the surface is pretreated mechanically, physically, chemically or electro-chemically. The low-pressure plasma process, in which oxygen ionisation generates a functionalisation of the surface, is an example of a standard physical surface pretreatment used in this thesis. The functionalisation improved the wetting properties with an increased surface energy in contact angle measurements [138, 141, 144–149]. By utilising oxygen as a process gas, the polymer surface acquires polar properties through dipoles. These dipoles form primary valence bonds with the adhesive layer, which significantly increases the adhesive strength [137, 145, 150]. Prior to plasma treatment, removing contaminations and impurities with solvents can enhance adhesive strength, resulting in cohesive failure dominance [138, 144–147, 151]. Subsequently, the bonding process is carried out or, in the optional third step, an adhesion promoter is applied in order to increase the adhesive strength and ageing resistance as well as to carry out preservation and/or air conditioning of the bonded surface [133].

2.4 Stress distribution and damage mechanism in adhesive joints

2.4.1 Scarfed joints

In general, it is recommended to avoid tensile and peel stresses in bonded joints, as the strength of the joint is highest under shear stress. This chapter 2.4 focuses on the stress analysis and damage behaviour of shear loads within bonded joints, specifically scarfed (Sc) joints and single-lap shear (SLS) joints. Peel bonding is defined by the peel ratio or peel angle, which is determined by the joint part thickness and peel length. The bonding surface increases and bond strength improves in a quasi-static load as the peel ratio increases or the peel angle decreases, due to reduced peel stress [152–159]. Post-repair strength compared to initial strength can be as low as 10% at a 45° scarf angle [160], reaching up to 84% at a 1.9° scarf angle [157]. The influence on damage accumulation during fatigue loading was more pronounced than during static loading. Specimens with a 1.9° scarf angle exhibited significantly higher fatigue strength than those with a 2.9° scarf angle [157]. The aim is to achieve scarf angles of less than 3° for Sc joint repairs in CFRP [161]. However, using low scarf angles require long, difficult-to-machine scarfs, resulting in the removal of a significant amount of undamaged material. An alternative to Sc repairs are multi-stage, stepped repairs where the cutter needs to be less inclined [162]. However, post-processing such as grinding is required to flatten the steps and reduce stress concentrations at the joint/adhesive interface [163]. The stiffness of the joining parts and the scarf ratio influence the stress distribution of the adhesive bonding, which in turn affects the type of failure. If the joining parts have multiple layers, peel and shear stress concentrations may occur adjacent to the 0° layers due to the high stiffness gradient [164–167]. Hey-Griss et al. [167] demonstrated in their modelling approach that failure occurs in the adjacent 45° layers and propagates in the width direction. However, experimental results show that cracks initiate on the free sides and grow towards the width centre of the specimens [165]. Peel and shear stress as well as strain concentration, even if minor, are created at the end of the joint in the case of joined parts with unidirectional orientation [164, 166]. Delamination occurs in the interface to the 0° layers (0/90 or 0/45) due to the high stiffness gradient and stress concentration, initiated by failure in the QI layers starting from the 90° layer, which has the lowest strength [166, 168, 169]. Delamination occurs in the interface to the 0° layers (0/90 or 0/45) due to the high stiffness gradient and stress concentration, initiated by failure in the QI layers starting from the 90° layer, which has the lowest strength [168]. The strength of the bonded joint is determined by the adhesive and is identified by a mixed fracture of adhesive and cohesive failure in the adhesive and adherend part [157, 168, 170]. As Kumar et al. [171] have demonstrated for Sc UD parts, the proportion of cohesive failure in the adherend parts increases as the scarf angle decreases. The stress concentration at the ends of UD joints results in failure initiation [166].

2.4.2 Single-lap shear joints

Single-lap shear (SLS) bonds are the most commonly used adhesive bonds due to the simple setup. The stress distribution of a SLS bond is based on the analyses of Volkersen and Roland Geissner [172–174] . The shear stress maxima occur at the overlap ends of an SLS bond, which decrease with increasing overlap length [35]. Due to an eccentric application of force, the parts to be joined and the adhesive bend, which also leads to higher peeling stresses at the ends of the overlap and initiates cracks in these areas. [175–178]. In order to reduce these stress maxima, geometric and material modifications have been made to the bonded parts or adhesives. Adhesive rounding [179], rounding or chamfering of the parts to be joined [180, 181] lead to a homogenised stress distribution.

2.4.3 Defects in adhesive joints

A large number of defects can occur within bonded joints due to the manufacturing process. These are typically categorised according to their scaling:

Porosity, voids and delamination [182], whereby the effective, stress-bearing adhesive layer area decreases and the strength of the bond decreases [183]. Due to external stress during operation, the defect can expand in size. Defects with a larger extent include kissing bonds, where there is direct contact between the adhesive and the bonded part, but no adhesive strength is present. Shear stresses are not transferred, but compressive stresses may be present [182–185]. Unlike separations and delaminations, kissing bonds cannot be directly measured in terms of volume. Therefore, commercial non-destructive testing (NDT) methods, such as ultrasonic examinations, are unable to detect kissing bonds [185]. The reduced adhesion caused by kissing bonds is caused by chemical interactions at the atomic level. The boundary layer reactions that form the bonding forces between the adhesive and the bonded part occur at molecular or atomic distances between 0.1 and 1 nm. However, the wavelength of the ultrasonic waves is several orders of magnitude longer, so that they are not able to detect the kissing bonds [186]. Insufficient cohesive strength due to incomplete or premature curing of the adhesive layer and the effects of moisture during storage or manufacturing can also reduce the strength of the bond. Surface impurities such as grease, oil, and particles can cause uneven wetting of the joining part surface. To prevent contamination, surface treatment methods such as mechanical abrasion and solvent treatment can be employed. Additionally, exceeding the adhesive's pot life can also result in insufficient surface wetting [133]. The literature examines the effect of manufacturing defects on bond strength and detectability, including felt-tip markers or PTFE films [155, 187, 188], silicone grease or release agents [21, 185, 189, 190] and hydraulic oil [191]. Regarding the silicone grease, even if the entire surface was contaminated, the adhesive strength was only reduced by 17 % [185]. However, for the release agent, almost no residual load-bearing capacity of the samples could be determined, and the adhesive strength was less than 1 MPa. While Hayes-Griss et al. [155] reported a reduction in strength of over 20 % when the effective defect area of PTFE film was 10 %. However, a 50 % increase in the effective defect area results in a 25 % reduction in strength [169]. Additionally, a 100 % adhesive failure was found in the case of the release agent.

2.5 Non destructive testing methods of composites

Ensuring the safe and reliable operation of FRP and accurately assess their integrity and condition, non-destructive testing (NDT) methods are necessary. In this context, Structural health monitoring (SHM) describes the process of detecting, locating and quantifying the extent of damage [192]. It is crucial to identify any damage and its type in-situ at an early stage, before a component is subjected to failure-critical loads, and throughout its entire life cycle. This enables retrospective assessment of structural integrity. Ideally, structural safety is significantly increased, and inspection costs, as well as machine downtimes are reduced. The integration of sensors, certain materials and equipment for data acquisition, transmission and processing into the structure is necessary depending on which method is used for SHM [193]. Generally, NDT methods can be classified into passive and active methods. Passive NDT refers to monitoring a structure using sensors only. When actuators are used in addition to the sensors, which excite the structure in a certain way, this is referred to as active NDT. Most NDT methods have a supporting effect during certain maintenance intervals of the component, e.g. ultrasonic inspection or x-ray examination, but detect the damage late, when it is already pronounced.

Digital image correlation [194], thermography [195] or 3D computed tomography [123] for composites need an elaborate and expensive testing setup and can also just detect damage when already pronounced since measurement cannot be performed continously.

A very promising NDT method, sensitive to damages and other material non-linearities is the vibro-acoustic modulation (VAM) method. It has a simple setup and without expensive hardware components needed for conventional non-linear methods [24, 25]. The high sensitivity in fatigue damage detection of metals and impact detection of composites has already been demonstrated [26–31]. However, a systematic change of the laminate structure of CFRP to show the influence of composite typical failure mechanisms to the vibro-acoustic signal is missing in literature. This approach contributes to the understanding of the vibro-acoustic signal in fibre composite materials. This chapter provides a concise overview of existing, well-established non-destructive testing (NDT) methods and categorises the VAM method within these. For this purpose, a brief extract of methods from Fig. 2.6 is described, preceded by an examination of the limitations and potential applications of the VAM method.

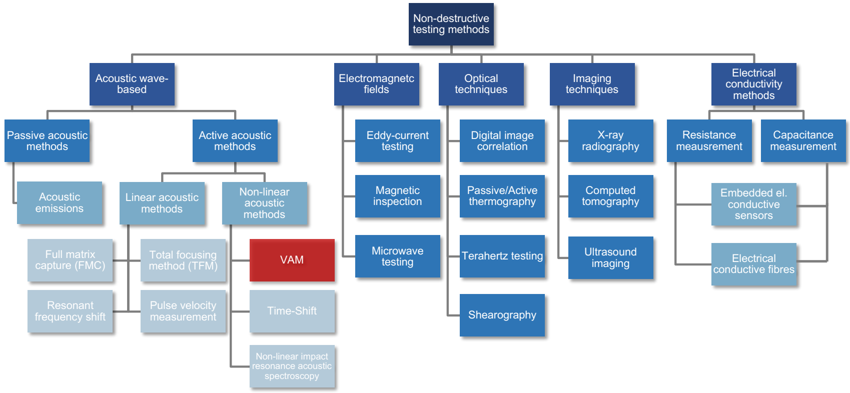

Figure 2.6: Overview and classification of non-destructive testing methods.

Acoustic emission

Acoustic emission (AE) measurement as a passive NDT analysis is used to detect the energy release during damage initiation with surface mounted piezoelectric sensors via acoustic signals in the form of elastic waves [196]. Accordingly, a measurement during operation is necessary and a prediction of the damage behaviour is simply impossible. Matrix cracks, delaminations and fibre breaks generate a characteristic signal in terms of amplitude, energy, oscillation period and frequency and can be sensitively detected in real time [197, 198]. However, this differentiation requires a conscientious analysis of the existing boundary conditions, such as background noise, load condition, and response signal, which is not generally valid for different materials. In terms of structural monitoring, AE measurement is limited and can only be used as a supplement, as it cannot characterize the initial state of a component [197, 199].

Electrical conductivity methods

Existing NDT methods such as electrical measurement of carbon nanofiller film sensors in composites [200, 201] enable monitoring strains and damages but require sensor integration during manufacturing. Electrical resistance- and capacitance-based measurements in fibre reinforced polymers (FRP), based on the intrinsic electrical conductivity of carbon fibres, without requiring further sensor networks, provide strain and damage detection [202–206]. Matrix cracks, delaminations and fibre failures are also detectable if conductive paths are interrupted within the material [202, 203] or if carbon fibre conductor spacing changes [207–209]. For capacitance measurement, it must be considered that usually a modification of the material with electrically insulating films must be carried out and however, a direct quantitative correlation between cracks and capacity changes in CFRP remains a challenge. All electrical measurements involve the requirement of direct contact between the measuring equipment and the conductive materials, which appears to be suitable for laboratory applications, but may encounter limitations in industrial applications. Furthermore, it is necessary to ensure that an insulation exists between the carbon fibres and other electrically conductive elements in the component in order to measure only the resistance or the capacitance of the fibres. Additionally, CFRP components in combination with metallic bolt or rivet connections can lead to contact corrosion [210–216], which would be promoted by applying an electrical signal.

Fibre optic sensors

In light conducting fibres used as fibre-optic sensors, length variations of the fibres can be measured, which influence the distance of the Fibre Bragg Grating (FBG) and hence change the power spectrum of the reflected light [217, 218]. Damages such as the development of transverse cracks in composite materials can also be observed with FBGs [218, 219]. Consequently, strain monitoring is possible under consideration of suitable temperature compensation [217, 220]. However, application in composites requires expensive, thin fibre-optic sensors without influencing the mechanical properties [219, 221].

Guided waves

NDT measurements based on wave propagation of mechanical waves such as guided, elastic lamb waves demonstrated an ability to determine elastic constants [222–225] and damage detections [221, 226–228] due to influencing wave propagation [229]. Especially the decrease of the phase velocity [52], or changes in output voltages or signal amplitudes [230–233] manifest itself when testing CFRP specimen in a fatigue experiment. Guided Wave testing has the potential to propagate long distances in the structure by using the structure itself as a waveguide, compared to a limited testing area in Ultrasonic (UT) methods. Guided waves are defined as waves that transport energy through an elastic medium, following Hooke's law and Newton's second law. They exhibit an infinite number of wave modes that can interact with each other, leading to mode transformations within multi-layer composites [234]. Guided waves are referred to as Lamb waves (LW) when the structure being analysed is plate-shaped and has a thickness within the wavelength range. Lamb wave induction produces both symmetrical and antisymmetrical wave modes, depending on the product of plate thickness h and excitation frequency f respectively the wave number k (see Equation 2.3 and 2.2). The dispersion diagram typically demonstrates the influence of the multimodal origin of the Lamb waves. At low frequencies, the fundamental modes A0 and S0 are present, characterized by simple bending/compression modes. As the excitation frequency increases, higher order Lamb wave modes also occur, with more complex amplitude shapes until a decreasing amplitude with increasing plate thickness. These specific wave propagations within the Lamb wave modes are fundamentally useful for detecting different types of damage, with S0 modes as shear waves having a more sensitive effect with regard to internal damage and A0 modes as bending waves with regard to superficial damage.

$$S - mode : \frac{\tan(\mathrm{qh})}{\tan(\mathrm{ph})} = \frac{-4\mathrm{k}^2\mathrm{pq}}{(\mathrm{q}^2 - \mathrm{k}^2)^2} \tag{2.2}$$

$$A - mode : \frac{\tan(\mathrm{qh})}{\tan(\mathrm{ph})} = \frac{(\mathrm{q}^2 - \mathrm{k}^2)^2}{-4\mathrm{k}^2\mathrm{pq}} \tag{2.3}$$

$$additional : \mathrm{q}^2 = \frac{\omega^2}{\mathrm{c}_\mathrm{T}^2} - \mathrm{k}^2; \mathrm{p}^2 = \frac{\omega^2}{\mathrm{c}_\mathrm{L}^2} - \mathrm{k}^2 \tag{2.4}$$

The longitudinal $\mathrm{c_L}$ and transverse propagation velocity $\mathrm{c_T}$ depend on the young's modulus E, the Lamé constant λ and Poisson's ratio ν, resulting in complex propagation behaviour with regard to anisotropic multilayer systems such as fibre composites.:

$$\mathrm{c_L} = \sqrt{\frac{\mathrm{E}(1-\nu)}{\rho(1+\nu)(1-2\nu)}} = \sqrt{\frac{2\nu(1-\nu)}{\rho(1-2\nu)}}; \mathrm{c_T} = \sqrt{\frac{\mathrm{E}}{2\rho(1+\nu)}} = \sqrt{\frac{\mu}{\rho}} \tag{2.5}$$

Active Thermography

Thermography measurements are used to detect damage by identifying local changes in the surface temperature of a component. This is achieved through the use of infrared sensors or thermal imaging cameras. However, it is important to note that the temperature being detected is above room temperature, which requires active energy input. Various methods are known for detecting damage in CFRP, including optical, electrical, eddy current, and ultrasonic excitation [235–240]. The measured temperature gradient can be used to identify defects or material flaws. The temperature change is caused by the alteration in the mechanical property, which in turn affects the thermal property. [235]

2.6 Vibro-acoustic modulation

Vibro-acoustic modulation (VAM) refers to a non-linear acoustic measurement. The use as a non-destructive testing method was first applied by Donskoy and Sutin et al. [25, 241–243], based on the work of Zaitsev et al. [244] as a proposal to detect cracks in metal. This approach has since been widely adopted in various fields and is known by various names: non- linear Ultrasound Vibro-Acoustic Modulation Technique (VMT or NUVM) [245], cross-modulated vibro-acoustics (CMVA or CM) [28, 245, 246] , non-linear wave modulation spectroscopy (NWMS) [247], non-linear acoustic modulation (NAM) [248].

The VAM method involves the simultaneous excitation of a high-frequency ultrasonic probe resp. carrier wave (f_{C}) and a low-frequency pump vibration (f_{P}). These waves are significantly different in their frequency (ω » Ω) and amplitude ($A\omega$ « $A\Omega$). The pump vibration induces changes in the stress state within the specimen, leading to alterations in the probe wave, as explained by Dorendorf et al. [249]. The propagation of high-frequency ultrasonic waves is influenced by existing non-linearities [25, 31, 241–243, 247, 250]. Figure 2.7 provides a visual representation of the fundamental principles of VAM and demonstrates how inhomogeneities impact both the time and frequency domains. In the time domain, a frequency/phase modulation (FM/PM) and amplitude modulation (AM) of the probe wave is observable. A completely linear structure would result in a pure superposition of $X\omega$ and $X\Omega$. An increase in the number of inhomogeneities within the material, such as defects caused by manufacturing processes and phase transitions, results in an increase in either FM or AM, as described by Donskoy et al. [251]. The frequency range is analysed using the Fast Fourier Transform, and significant modulation leads to the appearance of sidebands of considerable amplitude. In signal processing, it is known that AM produces one positive and one negative sideband ($f_{\mathrm{C}} \pm f_{\mathrm{P}}$). In contrast, with

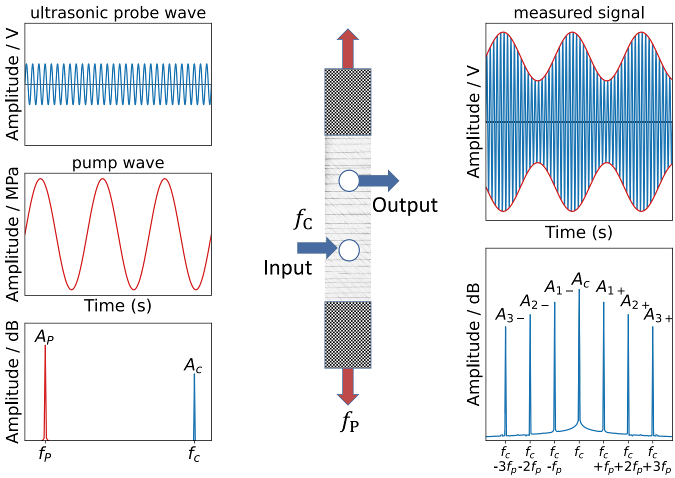

Figure 2.7: Illustration of the VAM measurement principle for fibre-reinforced composite structures. Due to damages and inhomogeneities in the fibre reinforced polymers the input signal is modulated. Two piezo-ceramic actuators were applied to the surface in the middle

FM, the number of sidebands is not restricted ($f_C \pm n \cdot f_P$) as elaborated by Oppermann et al. [252] and Ramezani et al. [253]. This characteristic allows the extent of phase modulation to serve as an indicator of damage. The measured signal comprises both AM and PM/FM components. It is possible to partially separate phase modulation from the signal using the short-time Fourier transform, as outlined in Oppermann et al.'s work [252]. One commonly used damage assessment metric is the modulation index (MI), as defined in Equation 2.6. The MI is calculated as the ratio between the amplitudes of the first sideband components and the amplitude of the carrier frequency, which encompasses both AM and PM. The calculation of the MI_n, related to higher-order sidebands, is provided by

$$\mathrm{MI_n} = \frac{A_{n+} + A_{n-}}{2 \cdot A_{\mathrm{Ca}}}; \qquad \mathrm{MI_n(dB)} = 20 \cdot \log_{10}(\mathrm{MI_n}) \tag{2.6}$$

where n indicates the order of the sidebands. It is frequently observed that an increased number of damages, such as cracks or delaminations, leads to an increasing MI [25, 254, 255].

Piezoceramic actuators are typically used to introduce high-frequency waves, while various approaches are employed to introduce low-frequency waves. Donskoy et al. [25] categorised the excitation of low-frequency vibration into vibro-modulation (VM) and impact modulation. Ambient modulation, on the other hand, is based on existing vibrations of the component during operation. Vibro-modulation involves continuous excitation through the use of electromagnetic shakers, servo-hydraulic testing machines, or piezoelectric actuators. During excitation with electromagnetic shakers, the test structures are typically excited orthogonally (transversally). This introduces bending mode shapes that can influence the stress state of cracks and modulate the high-frequency signal [26, 30, 256]. Servo-hydraulic testing machines allow for both longitudinal and transverse excitation of low-frequency oscillation. However, longitudinal excitation has been the focus of most of the work so far [30, 32, 33, 187, 249, 257–259]. The expansion of damage due to longitudinal excitation increases the modulation during the initiation and growth of local damage [30, 31, 260–262].
One method for detecting damage using piezoelectric actuators involves the use of two carrier signals and the Luxemburg-Gorky effect, also known as cross-modulation [263, 264]. The opening of existing cracks is triggered by a modulated carrier signal. Another piezo ceramic introduces a second unmodulated signal. The energy losses occurring at the defect transfer the modulation of the first carrier signal to the second carrier signal, generating sidebands along the frequency of the second carrier signal. Sohn et al. [265] and Miró et al. [266] introduced two unmodulated, linear carrier signals, which generated a non-linear modulation due to fatigue cracks. Pieczonka et al. [267] detected and localised impact damage in CFRP laminates by introducing the pump frequency using a piezoceramic actuator whose frequency matched the resonant frequency of the damage.

The impact modulation method provides for discontinuous, sudden excitation, such as by a hammer [30, 256], electromagnetic shaker or piezoceramic actuators [268–271]. However, the occurrence of sideband amplitudes requires a sufficient duration of the initial beat excitation. Environmental modulations may occur due to existing frequencies, such as external environmental vibrations (e.g. wind, traffic, maritime vibrations) or during operation (e.g. pumps, motors [30]). This enables the monitoring of the fatigue behaviour of rolling bearing systems, among other things [272–276].

3 Manufacturing Processes

The materials, the manufacturing process and the quality assurance methods employed are introduced in the following chapter. Advanced information on manufacturing processes, laminate structures, sample preparation, test preparation and test methods, which only apply to particular types of specimens, are directly in the respective chapter.

3.1 Materials

3.1.1 Carbon fibre reinforced polymer

Two different CFRP prepreg systems were used in this study. Table 3.1 shows the used layups and prepreg materials for the specific test methods. The prepreg system HexPly M21/35%/268/ T800S from Hexcel, which consist of an epoxy matrix (M21) with toughening thermoplastic particles and carbon fibres (T800s), was used to investigate the vibro-acoustic response signals of unidirectional manufactured aerospace-grade laminates. Quasi-isotropic (QI) specimens with low fibre area weights ($30\,\mathrm{g/m^2}$, $60\,\mathrm{g/m^2}$ and $120\,\mathrm{g/m^2}$) were manufactured using NTPT ThinPreg 402 epoxy resin from North Thin Ply Technology (NTPT), Switzerland and Toray T700SC-12K-60E fibres from Toray Industries, Japan. As a comparison to higher fibre area weights, the Hexply prepreg system with $268\,\mathrm{g/m^2}$ was also used for QI specimens.

3.1.2 Epoxy adhesive film

The adhesive film FM300-2M.03PSF from Solvay (Brussels, Belgium) with a nominal thickness of $0.13\,\mathrm{mm}$ and a nominal weight of $147\,\mathrm{g/m^2}$ used in this thesis for SLS and Sc joints is an epoxy resin system. The carrier film contains randomly oriented polyamide fibres that ensure a homogeneous adhesive layer thickness, resulting in a tensile shear strength of $40.7\,\mathrm{MPa}$ [277].

3.2 Manufacturing of CFRP specimen

The UD prepreg layers were brought into shape by a CNC cutter (Aristomat TL1625 from ARISTO Graphic Systeme GmbH & Co. KG i.I., Germany) and manually laminated. During layup an intermediate vacuum was applied to every fourth layer in the stacking sequence to compact the layers and prevent air inclusions. Curing was realised in an autoclave process (Scholz, Germany). The specific curing parameters were used according to the manufacturer's recommendation. Thickply prepreg was cured at 180 °C for 4 h with a pressure of 7 bar. Thinply prepregs were cured at 160°C for 4 h, also with a pressure of 7 bar. Each produced laminate was submitted to a quality control with ultrasonic C-Scans to detect manufacturing deviations.

Stress concentrations and premature failure in the clamping area during quasi-static or fatigue load application was reduced by adding glass fibre reinforced polymer (±45° layup) and aluminium tabs with a thickness of each 1 mm onto the specimens. These tabs cover 50 mm on both ends and were bonded with UHU Endfest Plus 300, cured at 80° C for 40 minutes and 30 kN in a hot press. All laminates were cut by a diamond blade on a high precision saw (ATM Brillant 265 from QATM, Germany) to dimensions according the respective test standard. Table 3.1 and Table 3.2 shows the geometries of the respective sample configurations and test method investigated in this study. In case of the OHT specimens, a double-edged diamond milling cutter with a diameter of 1.8 mm was used on a CNC milling machine (Isel EuroMod MP 30 from isel Germany AG, Germany) to mill the hole in the middle of the specimen. To supress edge effects caused by high surface roughness, which leads to damage initiation under static and fatigue loading, the specimens were polished with abrasive paper with a grain size of 600 and 1200 in two steps and cleaned using isopropanol.

Low velocity impact tests

Two different specimen geometries and prepreg materials were selected for the impact tests in this study and are shown in Table 3.1.

In preliminary tests for the Fatigue after Impact (FAI) specimens, the ply structure with HexPly M21/35%/268/T800S prepreg was also used, and impact energies of 8, 12, and 14 J were applied. However, this caused severe edge delamination due to high interlaminar stresses resulting from the tensile-compressive loading (refer to Figure 3.1). Due to the pronounced convexity of the individual

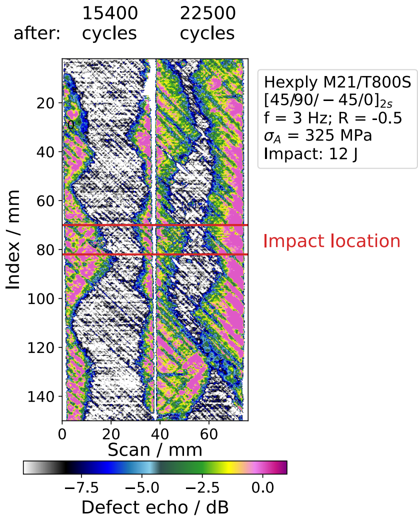

Figure 3.1: Ultrasonic C-Scan images of impacted CFRP Hexply M21/T800s specimens under tension-compression (R=-0.5) fatigue load with 325 MPa fatigue amplitude after 15400 and 22500 cycles. The impact location is indicated with red lines.

layers as a result of the edge delamination, it is almost impossible to adjust the aperture to record the edge delamination and the impact on the same side. Consequently, the location of the impact is also marked with red lines. A propagation of the introduced delaminations by the impact itself was not detected even at higher impact energies. Since it is known from other studies that the delamination area increases with decreasing ply thickness and thus the influence of the impact during fatigue loading increases, the thinply prepreg TP402+T700S was selected for the FAI-tests. These specimens are 250 mm long, 36 mm wide and 4.08 mm thick.

The Compression after Impact (CAI) specimen configuration employs a quasi-isotropic laminate of HexPly M21/35%/268/T800S with a thickness range of 4-6 mm and specimen geometry of 150x100 mm, according to ASTM D7136 [278].

Table 3.1: Laminate layups, prepreg materials and dimensions used for the specimens in different test methods.

Test Method	Prepreg	Areal weight in g/m^2	layup
Initial VAM	HexPly M21+T800S	268	$[0_4]_s$
Unnotched Fatigue	HexPly M21+T800S	268	$[0/90_7]_s$ $[0/90_6/0]_s$ $[0/90]_{4s}$ $[45/90/-45/0]_s$
	NTPT TP402+T700S	30 60 120	$[45/90/-45/0]_{12s}$ $[45/90/-45/0]_{6s}$ $[45/90/-45/0]_{3s}$
OHT	HexPly M21+T800S	268 536	$[45/90/-45/0]_{2s}$ $[45_2/90_2/-45_2/0_2]_s$
CAI	HexPly M21+T800S	268	$[45/90/-45/0]_{2s}$
FAI	NTPT TP402+T700S	30 60 120	$[45/90/-45/0]_{12s}$ $[45/90/-45/0]_{6s}$ $[45/90/-45/0]_{3s}$

Table 3.2: Overview of the test methods, specimen dimensions and load introduction elements

Test method	Tab material	Free test length in mm	Dimensions [LxWxT] in mm
Initial VAM	-	150	250x20x2.1
Unnotched Fatigue	1 mm GFRP + 1 mm Al	150	250x20x2.1
OHT	1 mm GFRP + 1 mm Al	150	250x36x4.08
CAI	-	120	150x100x4.08
FAI	-	250	250x36x2.88

3.3 Manufacturing of adhesively bonded CFRP joint specimens

The CFRP bonded joints were produced using an autoclave process, as detailed in chapter 3.2. The material utilised was the M21 prepreg system. Figures 3.3 and 3.4 illustrate the general structure of the sample types, including the specific layup of SLS and SC bonded joints.

3.3.1 Processing of the CFRP laminates

Milling process - Scarfed joints

The milling process for the Sc laminates on a CNC milling machine (Isel Euro-Mod MP 30 from isel Germany AG, Germany), using a diamond-toothed solid carbide milling cutter from Sorotec (Sorotec ID: LDV.0317) with a diameter of 3.175 mm, achieved a scarf ratio of 1:20, corresponding to a scarf angle of 2.86° (see Fig. 3.2). The spindle speed was set to 17,043 rpm, and the feed rate was 0.21 m/min, with the cutter axis perpendicular to the laminate centre plane and the milling direction parallel to the 0° layers. During the milling process, the milling cutter moves in 15 descending steps. Afterward, stress concentrations are reduced by levelling the steps with 320 grit sandpaper. Throughout the milling process, the laminate is fixed at the edges using a vacuum and double-sided adhesive tape.

Surface pre-treatment and solvent cleaning

The milling surface of the Sc laminates and the surface of the SLS laminates are cleaned using a cloth soaked in isopropanol in 0° fibre direction for several minutes until no further residue is visible on the cloth. The adherend parts at this point are placed in an ultrasonic bath for several minutes with the milled surface facing downwards to remove any remaining residues from the milling process. Subsequently, the laminates for both the Sc and SLS specimens are subjected to a further cleaning process involving isopropanol, with the objective of removing surface dirt and degreasing them. Finally, the adherend parts are pre-treated in a low-pressure plasma process for 90 s and 0.3 mbar at 300 W.

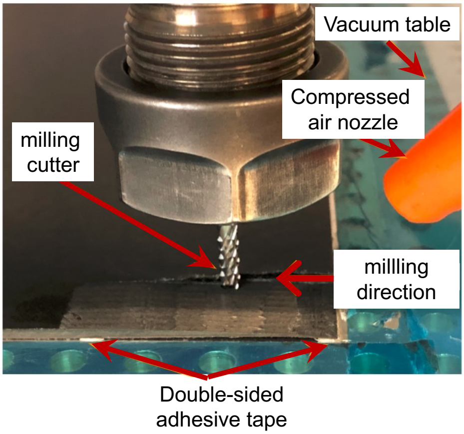

Figure 3.2: Milling process of the scarfed joints

3.3.2 Bonding Processes and defects inserts

Circular defects with a diameter of 7 mm, which corresponds to 5% of the adhesive film area, were artificially introduced at the centre of a adherend part's surface, following the method of Harder et al. [185] (see Fig. 3.3 and 3.5). To create a separation between the adhesive layer and the adherend part by a contaminant, a PTFE film (Goodfellow FP301100) with a thickness of 0.01 mm was applied. Additionally, the release agent W-64+ from Mikon was applied to generate a weak bond. The circular shape reduces stress concentrations on the defect based on geometry. Additionally, a stencil ensures accurate placement of defects at the center point, aligning them with the 0° layers in the case of scarfed joints. After the adhesive film has been applied to the SLS and Sc adherend parts, curing is carried out using an autoclave process. At two temperature dwell times, 100 °C for 30 min and 140 °C for 240 min, respectively, were applied. A relative pressure of 4 bar was reached in the autoclave oven and 0.80 bar in the vacuum bag. The test specimens were cut to a width of 25 mm using a diamond blade on a high-precision saw (ATM Brillant 265 from QATM, Germany).

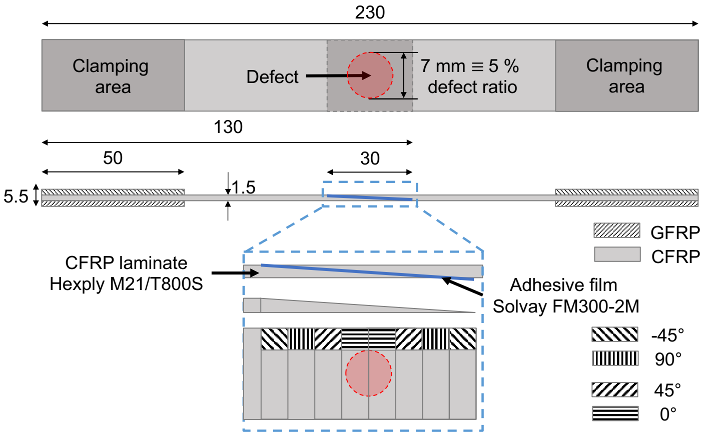

Figure 3.3: Specimen geometry of the Sc specimens including laminate layup, load introduction and dimensions in mm

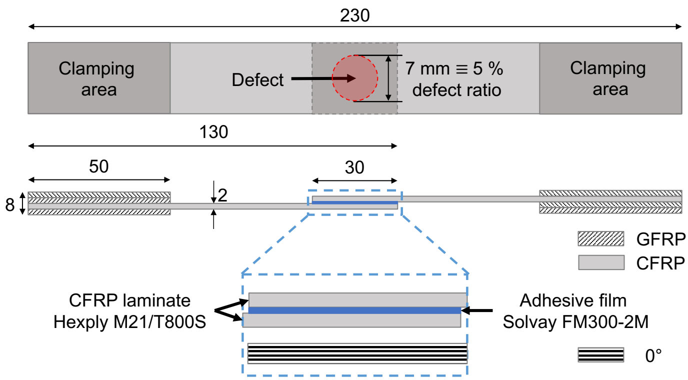

Figure 3.4: Specimen geometry of the SLS specimens including laminate layup, load introduction and dimensions in mm

3.4 Quality Assurance

Ultrasonic C-Scan

Manufactured specimens are inspected for defects and damage using a USPC 3040 DAC ultrasonic inspection system in an immersion ultrasonic process. The ultrasonic speed was assumed to be 2800 m/s for all specimens; however, this should only be regarded as an average value due to the presence of different layups and the general anisotropic characteristics of FRP. This may result in deviations from the expected measured depth. The excitation frequency is 20 MHz and the maximum amplification is 106 dB in 0.5 dB steps. The backwall echo data of the C-scan are used to calculate the projected delamiantion area. Using constant thresholding for all scans, the image was converted into a binary image. The area was then calculated by inverting the binary image and adding the black pixels of the area.

X-Ray Tomography

With excellent X-ray transmission, CRFPs are particularly suitable for the detection of defects and damage by X-ray tomography. The damaged samples were scanned with X-ray faxitron 43885 (Rohde & Schwarz USA, Inc, USA) using a zinc iodide contrast agent and digitised using a transmitted light scanner.

Acoustic Emission

To determine damage initiation of CFRP specimens, an acoustic emission (AE) analysis system was performed during specific mechanical tests. One micro-II multi-channel acquisition system (MISTRAS Group, Inc., USA) was used to record the AE data using two wideband differential sensors. These sensors are attached to one side of the free test length with a silicone grease as a transmission medium between between sensor and specimen surface. To eliminate noise caused by machine vibrations and ambient noise, internal filters and a static threshold are used. Table 3.3 shows the configuration of the AE detection system for performing step-wise tensile tests on unnotched cross-ply specimens and notched QI specimens.

Digital image correlation

Digital Image Correlation (DIC) was used for bonded CFRP laminates fatigue tests to determine three-dimensional specimen deformation during dynamic loading. The measurements were carried out using an ARAMIS 4M DIC system (GOM GmbH, Germany) in a stereoscopic setup. Since the measurement volume of 25x18 mm was limited for optical monitoring of the adhesive film, a

50 mm lens and 25 mm spacer rings were used. Prior to testing, a randomly applied high-contrast speckle pattern was sprayed onto the edge of the specimens using Satin Dupli-Color Platinum spray paint in white (RAL 9010) and in black (RAL9005) to enable the calculation of three-dimensional displacements using ARAMIS Professional 2016 software.

Light Microscopy

Micro-section and quality assurance were carried out using a VHX-6500 digital microscope (Keyence Corporation, Japan).

Capacitance Measurements

Capacitance measurements are performed on selected specimens used in the fatigue tests in bonded CFRP laminates. Copper strips are attached to both sides of the specimen to be tested and the capacitance is measured using the Peaktech 2170 LCR meter. A frequency of 10 kHz is set as the measurement frequency. To electrically isolate the copper tapes from the CFRP surface, a layer of adhesive tape is applied below the copper tapes. The length of the copper tapes is chosen to cover just the overlapping width of the adhesive bonding film. Idealised, this setup represents a straightforward plate condenser with the copper tapes acting as the plates. The capacitance of an ideal plate capacitor, C, can be calculated using Equation 3.1 [208, 279, 280]:

$$C = \epsilon_0 \cdot \epsilon_r \frac{A}{d} \tag{3.1}$$

Table 3.3: Configuration parameters of the AE acquisition system

Parametern	unnotched Cross-Ply	notched Quasi-isotropic
Samplingrate / MHz	5	5
Preamp gain / dB	20	40
Threshold / dB	45	45
Hit defintion time (HDT) / μs	250	150
Hit lockout time (HLT) / μs	800	800
Peak defintion time (PDT) / μs	150	50
Maximum hit duration / μs	100	100

Here, ϵ_0 refers to the permittivity of a vacuum, while ϵ_r represents the permittivity of the dielectric medium between the plates. A denotes the area of the plates, whereas d stands for the distance separating them. The parameters ϵ_0 and A remain constant throughout the experiments. Consequently, any alteration in capacitance is primarily attributable to changes in plate distance; this change is proportional to the difference in distance. Alternatively, a change in the permittivity of the dielectric medium causes the capacitance to alter. A space filled with air is created when a crack occurs in the specimen between the plates. This air then acts as an additional dielectric medium between the plates, which functions with an associated permittivity. Consequently, Equation 3.1 can be rephrased as follows:

$$C = \epsilon_0 \cdot A \frac{\epsilon_{r,CFK} \cdot \epsilon_{r,Luft}}{d_{CFK} \cdot \epsilon_{r,Luft} + d_{Luft} \cdot \epsilon_{r,CFK}} \tag{3.2}$$

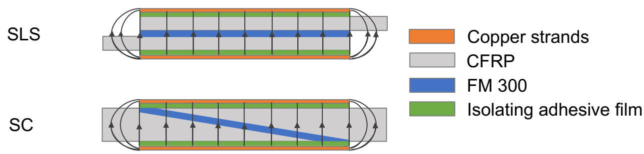

Figure 3.5: Schematic overview of the capacitive measurements of the CFRP adhesive joints including the electric field.

4 Experimental Methods

In this chapter, the experimental mechanical and vibro-acoustic methods used are presented. The suitability and sensitivity of the vibro-acoustic measurement are assessed, taking into account various layups, load cases, and types of damage. The parameters of the vibro-acoustic measurement are specified for certain mechanical test methods.

4.1 Mechanical Tests

4.1.1 Quasi-static and step-wise Tensile Tests

The static strength of each specimen and test configuration was performed on the universal testing machine Z100 from Zwick Roell (Ulm, Germany) according to DIN EN ISO 527-4 [281]. The specimens were clamped at a length of 50 mm. Strain measurement is carried out using multiXtens from ZwickRoell. The distance between the extensometer arms is 70 mm, the applied displacement rate depends on the standards of each quasi-static test. All tests were performed at an ambient temperature of 21°C and a humidity of 50 %. In general the tensile strength σ_t was calculated according to eq. 4.1 with failure load F, the specimen width w and the specimen thickness t.

$$\sigma_t = \frac{F}{wt} \tag{4.1}$$

To assess the shear strength of bonded CFRP joints, the effective bond area was measured at the fracture surfaces of the specimens. The shear strength σ_s results were obtained by dividing the failure load F by the specimen width w and overlap length l according to eq. 4.2.

$$\sigma_s = \frac{F}{wo} \tag{4.2}$$

The step-wise tensile investigations according to DIN EN ISO 527-4 [281] were carried out on a servo-hydraulic fatigue testing system 8802L2741 from Instron. The selected stress levels are based on the respective results of the quasi-static tensile tests.

4.1.2 Open-Hole Tensile Tests

The servo-hydraulic testing machine (Instron 8802L2741) was also used for OHT tests, following ASTM D5766 [282]. The near field stress σ_{nf} has been calculated with the force F, the hole diameter d, the specimen width w and the specimen thickness t in accordance with eq. 4.3.

$$\sigma_{nf} = \frac{F}{(w-d)t} \tag{4.3}$$

The step-wise tensile investigations according to DIN EN ISO 527-4 [281] were carried out on servo-hydraulic fatigue testing systems from Instron.

4.1.3 Fatigue tests

For all specimens without impact pre-damage, the fatigue test was performed using a servo-hydraulic universal testing machine (Instron 8802 L2741) at 3 Hz in tension-tension mode (stress ratio R=0.1)

4.1.4 Impact tests

The impact damages were introduced into the CAI and FAI specimens by a drop tower (Instron 9450). This machine was equipped with an anti-rebound device to prevent multiple impacts and utilized a hemispherical tip with a diameter of 12.5 mm. According to the LVI impact characteristics described by Richardson et al. [283] and Sjoblom et al. [284], for different impact energies, the drop height was varied at a constant impact acceleration and final weight with 4.43 kg. Impact energies of 5, 6.5, and 8 J were selected for the FAI specimens based on preliminary tests. Impact energies above 8 J generated delaminations that propagated to the specimen edge, and thus, the pre-damage increased dramatically. The clamping devices were restricted according to ASTM D7136-05 [278]. Four rubber tips held the specimen with a force of 1100 N during the impact tests.

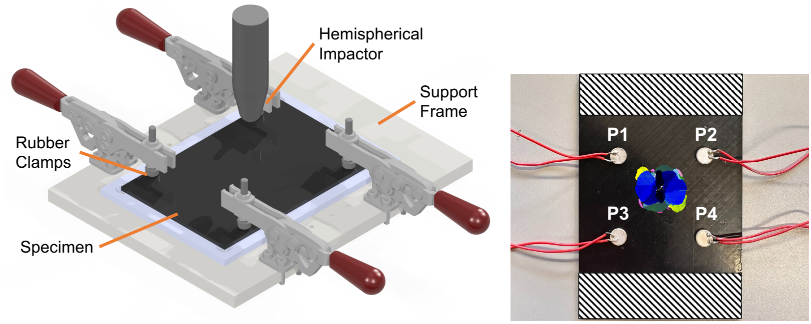

Figure 4.1: Clamping device for impact tests of CAI specimens (left) and contacting the piezoceramic actuator disks of the sensor network along the resulting impact damage (right)

The specimens are aligned by mechanical end stops (see Fig. 4.2 and Fig. 4.1).

Fatigue after Impact

The fatigue-after-impact experiments were carried out on a servo-hydraulic system (8802L2741) from Instron in stress-controlled mode at 3 Hz. In order to fix the specimens, servo-hydraulic clamps with a pressure of 120 bar were used. The deflection of the cylinder was used to calculate the strain of the specimens. Using a stress ratio of R=-0.5 in tension-compression regime, the maximum tensile loads are twice as high as the compressive loads. Assuming that fibre composites are typically designed for tensile loading and account for the majority of operational stresses, a stress ratio of R=-0.5 is generally realistic. This is especially true when considering the compressive strength, which reduces predamage in the form of impact. To prevent buckling and torsion during compressive load, the buckling support according to ASTM D6484 [285] was used (see Fig. 4.2 right). In order to analyse the occurence of damage and potential damage growth, exemplary tests were carried out on some specimens with a maximum fatigue load of 260 MPa and stopped at selected number of cycles using ultrasonic C-scan. The test procedures and data acquisition were carried out using WaveMatrix software (Instron) under constant climate conditions (23° C and 50 %).

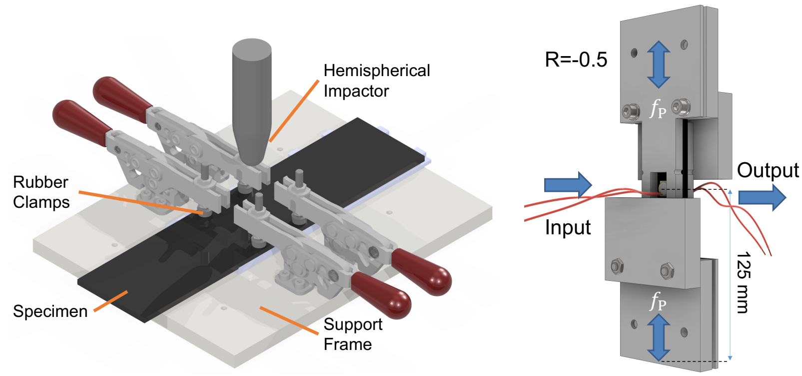

Figure 4.2: Clamping device for impact tests of FAI specimens (left) and contacting the input and output piezoceramic actuator disks during VAM measurement of FAI specimens at R=-0.5 including anti-buckling support (right)

4.1.5 Vibro-acoustic measurements

In general, the vibro-acoustic measurements were conducted with a similar setup to ref. [187, 249, 286]. A servo-hydraulic testing machine (8802L2741) from Instron is used to initiate the pump amplitude and piezoceramic actuator disks (PI-Ceramics PRYY+0863 10x2 mm with PIC255 ceramic) are responsible for the high-frequency oscillation. These piezoceramic disks were bonded to the specimen with double-sided tape (Tesa 56172; thickness 0.185 mm). This procedure results in a reduced signal strength of the measured lamb waves at 35-40 %compared to epoxy bonding and an MI offset of 3 dB is observable [33]. However, in case of damages, the MI increases for both bond-types with R^2=0.98, the signal-to-noise ratio remains similar, and it allows for the reuse of the piezoceramics. The data acquisition board used for carrier wave excitation and system response measurement was the NI-USB 6366 from National Instruments with a sampling rate of 2 MS/s and 16-bit resolution. The carrier signal was amplified using the WMA-300 high voltage amplifier from Falco Systems and an additional low-pass filter of 420 kHz to 50 V_{PP}. In order to select the optimum frequency band (185-230 kHz) for the excitation and measurement, a linear frequency chirp was applied to the probe signal. This chirp ranged from 1 to 300 kHz and was performed within 10 s at a constant amplitude of 50 V_{PP}. With an increment of 1 kHz, this results in 46 measurements of 2 s per specimen (see Fig. 4.3).

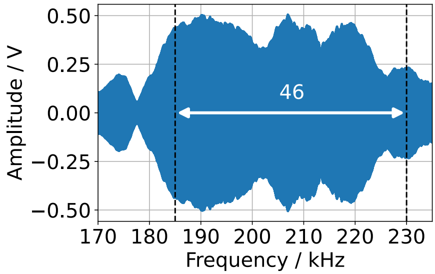

Figure 4.3: Resulting amplitude of a linear frequency chirp for a quasi-isotropic CFRP specimen over the frequency range of 170-235 kHz. The optimal frequency range of the piezoceramic actuators for excitation and measurement is highlighted, which amounts to 46 frequencies.

This measurement setup is used for initial measurements to determine the influencing parameters of low-frequency insertion and for suitable for pre-damaged impact test specimens or defect-induced CFRP bonded joints. Both the load introduction of the low-frequency vibration and the stress ratio R vary depending on the test and sample configuration. The Instron 8802L2741 was used to introduce the longitudinal pump wave under stress control mode at 3 Hz for every VAM measurement. A low-frequency vibration amplitude of 39.5 MPa is set manually, resulting in an longitudinal oscillation ranging from 7 MPa to 70 MPa with R=0.1 in case of step-wise tensile tests.

A sensor network of 4 piezoceramic actuators (labelled P1 to P4) was created symmetrically around the impact damage on the CAI samples (see exemplary Fig. 4.1). The purpose is to investigate the influence of the measurement direction on the VAM signal when additionally alternating the signal paths between receiver and transmitter for each specimen. To ensure reproducibility of results, a 3D-printed mould was used as a template that dictated the positioning of the piezoceramics. Boll et al. [187] have shown that a higher accuracy in the detection of weak bonds in single-lap shear joints can be achieved with an asymmetrical arrangement of the piezoceramics compared to the symmetrical arrangement. However, the damage was localised at a clearly defined point (the bond), resulting in the shortest propagation of lamb waves always through the defect. Investigating the positioning of the piezoceramics is essential in determining the localisation of impact-induced damage in FRP by VAM, which can often only be realised using a vibrometer.

In the fatigue tests, one pump amplitude and one fatigue amplitude with the same frequency (3 Hz) were introduced by the hydraulic testing machine for each specimen and controlled with the Instron WaveMatrix software. Each configuration was tested with different fatigue amplitudes in order to obtain a corresponding estimate of durability. Due to the multiphase and multilayer structure of CFRP, the relative movement of the individual layers to each other and between matrix and fibers is significant under fatigue load. Consequently, the energy dissipation increases due to the friction of the individual components and the visco-elastic behavior of the matrix and the material heats up [287]. In order to maintain this effect at a negligible level and also to prevent heating of the piezoceramics, the lower frequency is subsequently set to 3 Hz only. Resonant frequencies of Köhlbrand Bridge (2.441 Hz) [288] and offshore wind turbines are also in this range (0.35-2 Hz) [288, 289], increasing the practical relevance through the selected test setup. The environmental vibrations that exist in practice and could be used as low-frequency vibrations are superimpositions of 10-20 Hz on bridges [252, 288] and in the frequency range from 1-4 Hz to over 500 Hz on wind turbines [290]. The fatigue amplitudes were selected to be in the linear-elastic regime of the quasi-static tensile tests, carried out previously. For all specimens, without an impact pre-damage, the fatigue tests were performed in tension-tension mode (stress ratio R=0.1). The specimens for the impact experiments were dynamically loaded in the tension-compression regime, resulting in a tensile load that was twice as high as the compressive load (stress ratio R=-0.5). To prevent damages within the VAM measurement, a stress amplitude $\sigma_{\mathrm{A}} = 31.5\,\mathrm{MPa}$ is selected as pump amplitude under tension-tension load (R=0.1) respective tension-compression load (R=-0.5). Depending on the laminate layup, this pump amplitude equals lower 10 % of the tensile strength.

Figure 4.4 shows schematically the order in which the high and low frequency vibrations are introduced. Typically, in FRP initiation and growth of matrix cracks occur more frequently at the beginning of the service life, which lead to a rapid FRP degradation [52, 291–294]. In order to detect these stiffness-reducing damages via the VAM, an initial measurement is carried out before the first mechanical load initiation. Further VAM measurements at pump amplitude ($\sigma_{\mathrm{A}} = 31.5\,\mathrm{MPa}$) follow in logarithmically increasing number of fatigue cycles after 1 , 11, 111 and 1111 fatigue cycles. Subsequent measurements were each conducted after 3570 cycles of fatigue loading in a loop, corresponding to 20 min. Additionally, after each VAM measurement, the specimens are unloaded by the

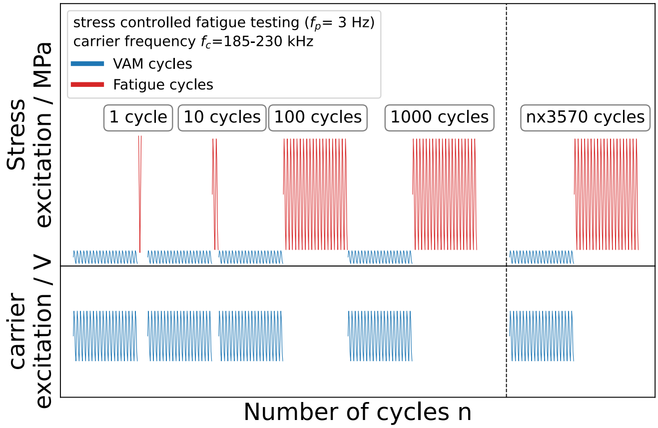

Figure 4.4: Schematic test procedure for fatigue tests with VAM measurement. First VAM measurement at initial state and after logarithmic increasing number of fatigue cycles, second measurement applied as repeating loops

servo-hydraulic testing machine in order to perform another linear chirp of 1-300 kHz for 10 s. This procedure serves to identify a possible frequency shift in the signal as well as to assess the general signal strength.

To record the elongation of the adhesive film during fatigue in CFRP-bonded joints, the DIC System was used. Each of these images was captured in the initial loads (1, 11, 111 and 1111 fatigue cycles) before the subsequent load cycles. From the start of the loop, 28 images were then recorded via a ring buffer to ensure that the failure of the test specimens was detected.

4.1.6 Data preparation

The piezoceramic receiver generates a signal which is stored in the time domain by a MATLAB script and then converted to the frequency domain using the Numpy FFT package in Python 3.9. To achieve high frequency resolution and reduce spectral leakage, a Hanning window was used. For each measured signal, the carrier and positive and negative sidebands were identified as maxima within their respective frequency ranges. The damage parameters MI, AM, and PM, complete time and frequency sections, as well as the negative and positive sidebands were extracted, depending on the test setup and evaluation method.

These parameters were then evaluated in data frames using Python scripts for data processing and visualization.

5 Results and Discussion

5.1 Initial measurements of UD specimens

In order to clarify which influencing factors play a role for VAM, the stress amplitude, mean value and stress ratio R of the low-frequency signal was systematically varied. For this purpose UD prepreg specimens were used to prevent damages within the material during measurement. The piezo ceramic actuators were arranged consistently on one surface at a distance of 70 mm.

The results of amplitude variation are shown in Fig. 5.1. The diagram on the upper left side illustrates the MI amplitude in blue of a representative UD specimen with increasing stress amplitude as increasing color intensity at a constant mean stress (58.5 MPa). The AM and PM Amplitude are shown at the upper right respectively at the lower left side. The variation of the stress amplitude was chosen from 11.5 MPa to 56.5 MPa, ensuring that the resulting stress maximum (115 MPa) should not cause any damage, according to the theoretical tensile strength of 3039 MPa. Figure 5.2 on the other hand shows the MI, AM and PM amplitude with increasing mean stress at a constant stress amplitude (22.5 MPa) as a function of the induced carrier frequencies. The mean stress was varied between 27.5 MPa and 72.5 MPa using the linear elastic range to prevent damage. In the selected frequency range of 185-230 kHz, the MI, AM and PM amplitude increases significantly with increasing stress amplitude, while the mean stress does not influence the modulation. This correlation is also significantly evident in the time domain. While the hills and valleys of the enveloping signal are more pronounced with increasing stress amplitude, they remain constant with varying mean stress. The amplitude modulation of the enveloping signal can be visualised, while the phase modulation only becomes visible with a higher time resolution due to the high carrier frequency. Compared to pure amplitude variation, mean amplitude variation at higher stresses causes a frequency shift of 1-2 kHz towards higher frequencies. This shift is clearly visible in the range between 220 and 230 kHz. The change in eigenfrequency of the test specimen

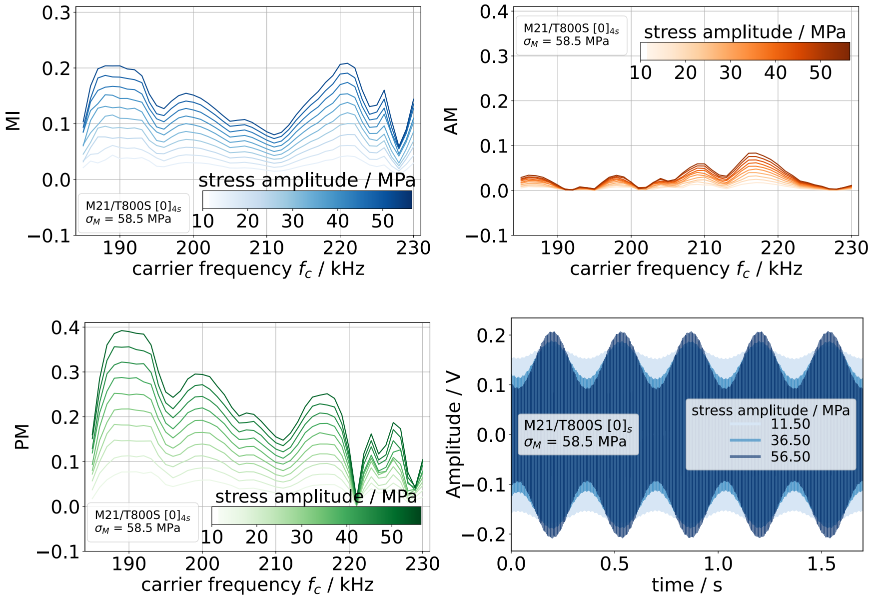

Figure 5.1: Vibro-acoustic response signal of an UD specimen with varied stress amplitude and constant mean stress $\sigma_\mathrm{M} = 58.5\,\mathrm{MPa}$ – top left: as MI; top right: as AM; bottom left: as PM in the frequency domain and bottom right: as modulated signal in time domain.

can be attributed to this behaviour. The selected stress amplitude of 22.5 MPa results in higher preloading of the specimen compared to tests with pure amplitude variation, similar to the preloading of a guitar string. Both a negative cross section and positive length change, as well as the increasing preload, are proportional to an increasing propagation velocity, which increases the eigenfrequency. However, due to the high stiffness of the T800s Carbon fibres within UD specimens, the change in cross-section and length at this low stress level is very small, which explains the slight frequency shift.

These stress-dependent VAM amplitudes agree well with the results of Donskoy et al. [295] and Ballad et al. [248]. However in both studies, the exact influence of the stress values was not evaluated, as both mean and amplitude stress were not isolated varied, resulting in a variation of the stress ratio R. Accordingly, the stress amplitude and mean stress were also increased in this work at a constant stress ratio R=0.1 (shown in Appendix 7.1 Fig. G.1). The stress amplitude was selected here between 22.5 MPa and 42.75 MPa, which is significantly lower than

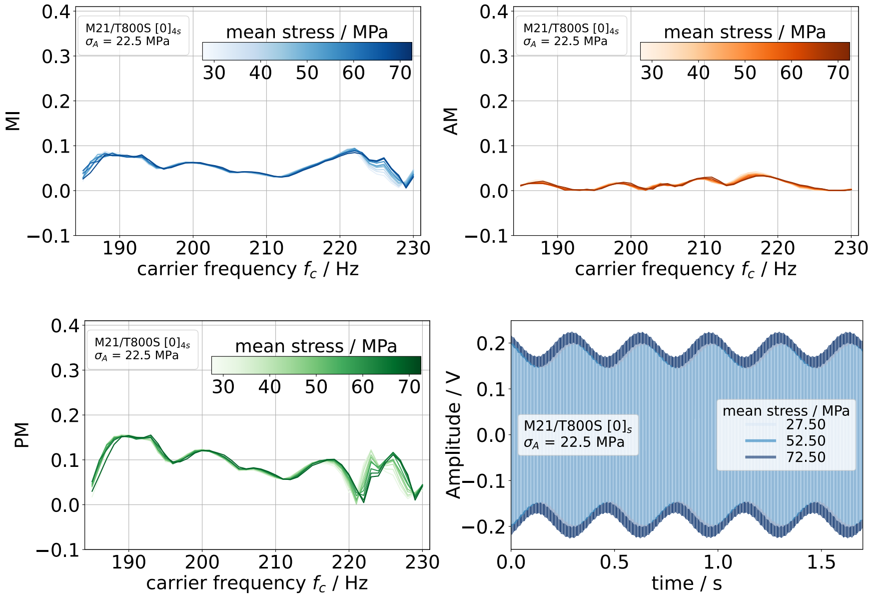

Figure 5.2: Vibro-acoustic response signal of an UD specimen with varied mean stress and constant stress amplitude $\sigma_A = 22.5\,\mathrm{MPa}$ – top left: as MI; top right: as AM; bottom left: as PM in the frequency domain and bottom right: as modulated signal in time domain.

with the pure variation of the stress amplitude from Fig. 5.1. This results in a smaller increase in MI, AM and PM as well as less pronounced peaks and valleys in the enveloping curve due to the excitation.

In order to investigate the influence of the stress introduction, the UD specimens were subjected to tension-tension and tension-compression loading, as shown in Fig. 5.3. The stress ratio was varied from 0.1 to 0.3 in the tension-tension regime and from -0.1 to -0.5 in the tension-compression regime. The variation of the stress amplitude in the tension-compression regime was chosen starting at 20.25 MPa up to 40.5 MPa, ensuring the resulting stress maximum (115 MPa) should not cause any damage, according to the theoretical compression strength of 1669 MPa [296]. As explained in Chapter 4.1.4, buckling of the specimens during compression loading was prevented by a buckling support.The resulting MI, AM and PM was shown as a plot of the stress amplitude. Also, PM and AM were included in order to quantify the ratios of the modulation components. The curves of the UD specimen under tension-tension load show that the AM is sig-

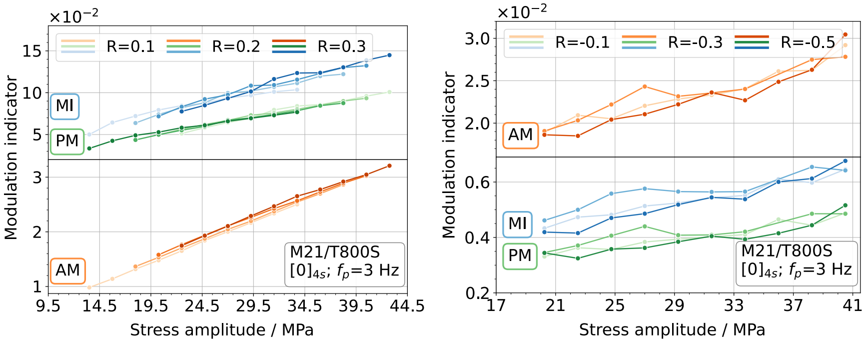

Figure 5.3: Plot for the determination of MI, AM and PM Amplitude of $[0]_{4s}$ CFRP with varying stress ratio R under tension-tension load (left) and under tension-compression load (right)

nificantly reduced compared to PM, which has the strongest contribution to the modulation. Both damage indicators increase with increasing stress amplitude, without any influence of the stress ratio R. The amplitude curves are identical. In the tension-compression regime, a significant linear correlation is also observed between the increasing damage indicators and the increasing stress amplitude. Here, the results confirm the observations made in the tension-tension regime, where the stress ratio does not influence the modulation. The PM is significantly reduced and the AM has the strongest contribution to the modulation. However, due to the use of the anti-buckling support, the measured amplitudes of MI and PM are more than a decade lower compared to the tension range. This can be explained by the fact that transverse deflection due to transverse contraction is naturally prevented during longitudinal excitation and the specimen stiffness increases immensely. This results in lower sideband amplitudes because the propagation of the high-frequency oscillations is weakened and a lower PM. The comparison of the FFT signals of tension-tension and tension-compression loaded specimens in Fig. 5.4 reveals more pronounced higher order sidebands in the tension-tension specimen, which can be attributed to the use of the buckling support for the tension-compression loaded specimens. This observation is consistent with the higher PM content. The AM, on the other hand, remains in the same range of magnitude as in the tension-tension regime.

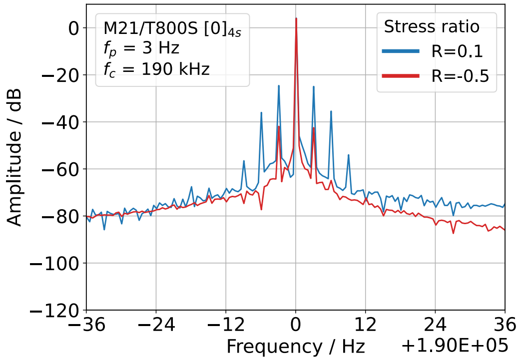

Figure 5.4: FFT signal of $[0]_{4s}$ CFRP laminates at 190 kHz carrier frequency and 3 Hz pump frequency under tension-tension load (R=0.1) and tension-compression load (R=-0.5)

The amplitudes of the vibro-acoustic measurement and the increase in amplitudes due to the increasing stress amplitude are not affected by the variation of the pump frequency from 3 to 9 Hz (see Fig. 5.5). However, the sideband amplitudes, which are shifted by the pump frequency, can be recognized in the FFT signal, but their level remains unaffected by the pump frequency. To ensure that the specimens do not heat up due to energy dissipation caused by friction and viscoelastic nature of the matrix at high frequencies, it is generally recommended to use a low frequency. Therefore, a frequency of 3 Hz was used in subsequent experiments. Boll et al. [297] confirming this results, demonstrating the vibro-acoustic signal can be synthesised using various statically approached discrete force levels. The pumping frequency can be scaled up or down after merging without affecting the general VAM signal.

Based on the initial VAM measurements for undamaged $[0]_{ns}$ laminates, it can be concluded that VAM is applicable under different stress states and demonstrates high flexibility under multiaxial loading. These findings suggest potential for detecting damage by VAM and warrant further testing. The increase of MI, as well as AM and PM, is affected by higher stress amplitudes respective deflection of the specimen. Therefore, an increase in specimen deflection indicates damage occurrence under constant stress application. This enables monitoring of the service life of CFRP laminates, both in cases of sudden damage and under fatigue, regardless of the stress state. Additionally, damage types that are critical under pressure, such as delaminations, could be tested initially using VAM

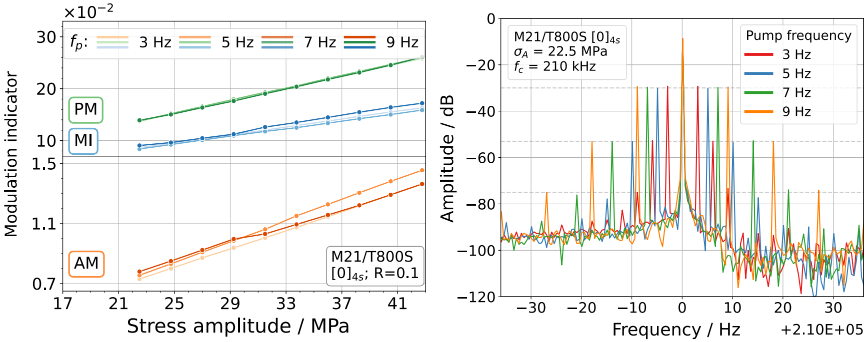

Figure 5.5: MI, AM and PM Amplitude (left) and FFT-Signal at 210 kHz (right) of $[0]_{4s}$ CFRP with stress ratio of R=0.1 depending on the LF frequency

on impact tests, and their damage growth could be assessed using fatigue tests. The final area of investigation concerns epoxy adhesive bonds, which typically exhibit brittle material behaviour due to their high stiffness and are expected to undergo minimal changes in length during fatigue. In this context, sensitivity to artificially introduced defects should also be examined.

5.2 Quasi-static and step-wise tensile tests

Unnotched tensile tests

In the following, series of tests are presented which examine the VAM test setup in the event of damage occurring. Fig. 5.6 represents mechanical behavior of representative cross-ply specimens via the stress-strain curves during quasi-static tensile tests. Each specimen exhibits a linear stress increase until brittle failure. The occurrence of cracks in the 90° layers shifts towards lower stresses and strains as the number of 90° layers resp. the resulting ply thickness increase, which is known as insitu strength [10]. These cracks are labelled as inserts with a slightly decreasing stress curve. Additionally, as the number of 0° layers increases, the modulus of elasticity also increases. The tensile strengths of the $[0/90]_{4s}$, $[0/90_6/0]_s$, and $[0/90_7]_s$ specimens are 1395.5 ± 60.49 MPa, 772.5 ± 68.06 MPa, and 339.5 ± 23.56 MPa, respectively. The corresponding elongation at break and tensile strength values, along with their standard deviations, are indicated by different colours on the stress curve.

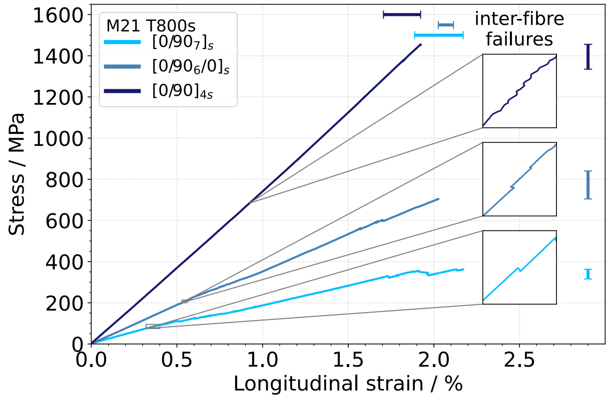

Figure 5.6: Stress-strain curves of the cross-ply specimens under tensile load. The mean and standard deviation of the ultimate tensile strength and elongation at break is marked for each specimen configuration respectively next to the corresponding axis

Fig. 5.7 shows the results of the VAM measurement including acoustic emission measurements during step-wise-tensile tests. The stress-strain curves are shown in red, and the corresponding hits in kHz during loading are indicated by blue dots. The emitted energy increases as the recorded hits become more blue, indicating a greater damage state. Due to the sensor's eigenfrequencies, the hits at 50, 100, 150, 200 and 250 kHz are excluded. In addition, the frequency range for the specific types of damage in CFRP observed by Gutkin et al. [198] was colour-coded. VAM parameters included modulation indices up to the third order. Initially, the MI's of the $[0/90]_{4s}$ specimen remain constant until 650 MPa applied stress, which can be interpreted as low damage, analogous to the linear-elastic range (see Fig. 5.6). The AE signal shows initial small damage with hits below 50 Hz and low cummulated energy below $0.6 \cdot 10^{\mathbf{9}}$ aJ, which can be attributed to initial small matrix cracks in the CFRP that are not fully induced across the specimen width [198, 298]. Further damage with high energy and frequencies of less than 50 kHz to around 170 kHz, which is attributed to matrix cracks and small delaminations [198, 298, 299], occurs from around 850 MPa. Comparable energy damage is introduced at each load step from 900 MPa. This correlates with a steady increase in the modulation indices. The highest energy damage is visible at loads between 1100 and 1280 MPa. Beyond this point, the emitted energy drops significantly and the increase in the modulation indices flattens out, which can be attributed to a reduction in fracture energy due to the onset of crack saturation. When examining the AE results of the stepped tensile test for the $[0/90_6/0]_s$ specimen, it is evident that the initial damage occurs much earlier at 250 MPa, which is consistent with the findings of the pure tensile test. Hits are detected in the frequency range up to 140 kHz with high emitted energy of up to $2.75 \cdot 10^{10}$ aJ, which can be attributed to complete matrix cracks and delamination. The modulation indices increase in this stress range. In the subsequent stages, additional damage occurs as the frequency and emitted energies of the delaminations increase. The VAM and AE measurements confirm that crack saturation also occurs in this range. A flattening of the VAM curves is noticeable at 750 MPa. As anticipated, the initial damage detectable with AE and VAM measurements is observed in the $[0/90_7]_s$ specimens between 125 and 160 MPa. The number of detected delaminations increases as the number of contiguous 90° layers increases. A clear increase in damage towards lower stress is recognisable. Fewer but larger cracks appear, whose growth cannot be prevented by neighbouring, differently oriented layers and whose emitted energy is higher. The modulation indices increase more significantly with a greater number of 90° layers, as a result of the high local strains caused by low-frequency excitation from the servo-hydraulic testing machine. It is possible to detect crack saturation in all CP laminates.

Fig. 5.8 shows the chirp signals of the CP laminates during the step-wise tests. The measured signal of the $[0/90]_{4s}$ specimens remains almost constant over the tested stress range, with a slight reduction in signal strength and a recognisable frequency shift occurring in the range between 230 kHz and 245 kHz. In the test specimens with layer structures $[0/90_6/0]_s$ and $[0/90_7]_s$, a significant signal attenuation is noticeable from the third stress level, which can be attributed to delamination. Even after the initial two load levels of the $[0/90_7]_s$ specimen, the frequency response of the chirp signal remains diffuse. No frequency shift is detectable in any range. These observations are realistic, as only a slight change in stiffness is expected.

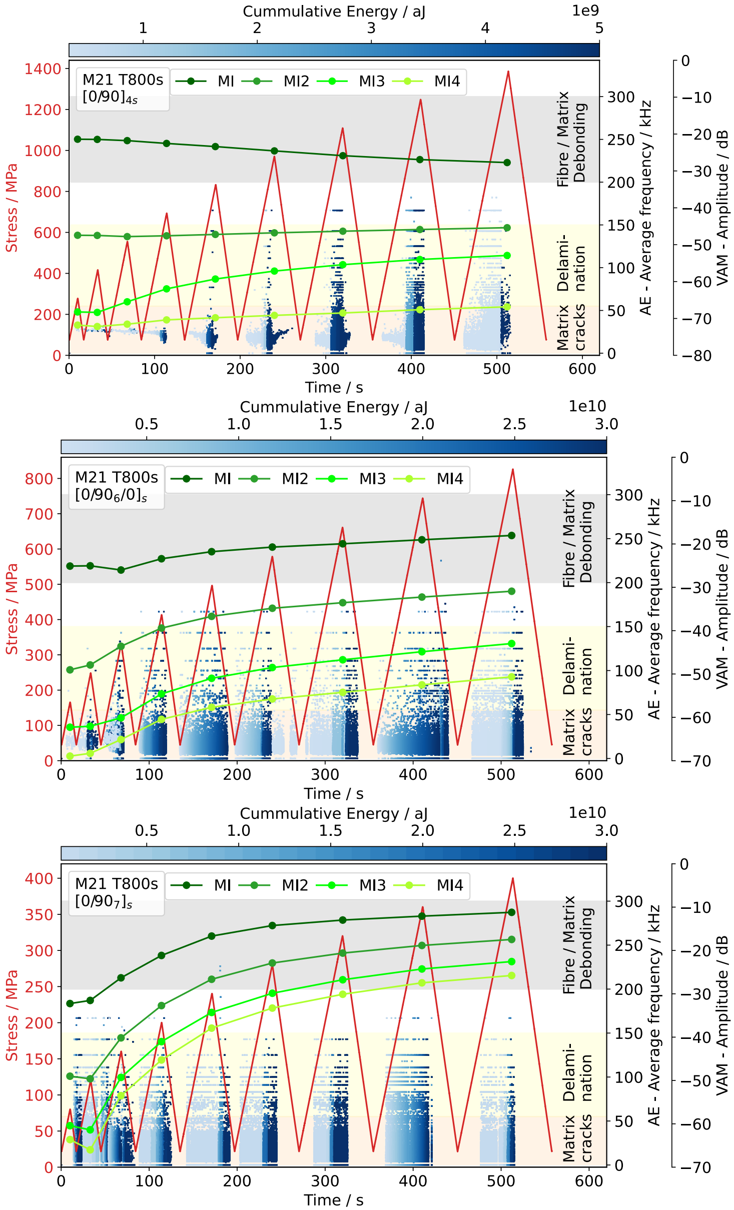

Figure 5.7: Representative results of step-wise tensile tests on CP specimens, including stress, modulation indices and acoustic emission measurements; top: $[0/90]_{4s}$; middle: $[0/90_6/0]_s$; bottom: $[0/90_7]_s$.

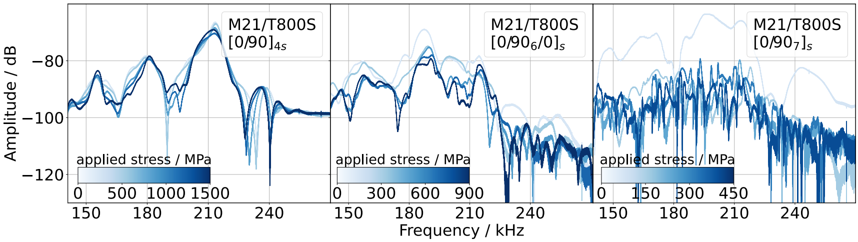

Figure 5.8: Chirp signal of CFRP cross-ply laminates at 3Hz pump frequency after initial and continuous stepped loading with $[0/90]_{4s}$ (left), $[0/90_6/0]_s$ (center) and $[0/90_7]_s$ (right) configuration.

The order of the sidebands increases under load as the number of 90° layers increases in the frequency range (see fig. 5.9). The $[0/90]_{4s}$ laminates produce sidebands up to the fifth order up to the last stress level, while the $[0/90_6/0]_s$ and $[0/90_7]_s$ laminates produce over 12 sidebands. As a result, the measured VAM signal experiences strong phase modulation. Fig. 5.10 shows that the MI and PM amplitudes of the CP laminates increase with load. The increase in these amplitudes is higher with a higher number of contiguous 90° layers. However, the AM component exhibits a significant decrease, which further reduces with increasing load.

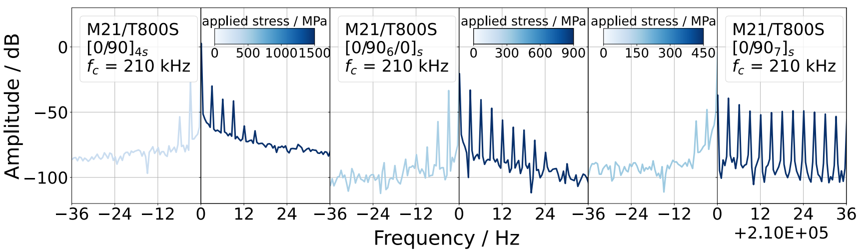

Figure 5.9: FFT signal of CFRP cross-ply laminates at 200 kHz and 3 Hz after initial and continuous stepped loading with $[0/90]_{4s}$ (left), $[0/90_6/0]_s$ (center) and $[0/90_7]_s$ (right) configuration. The FFT signal displays negative (left half-image) and positive sidebands (right half-image), which illustrate the damage propagation from the initial to the last loading stage.

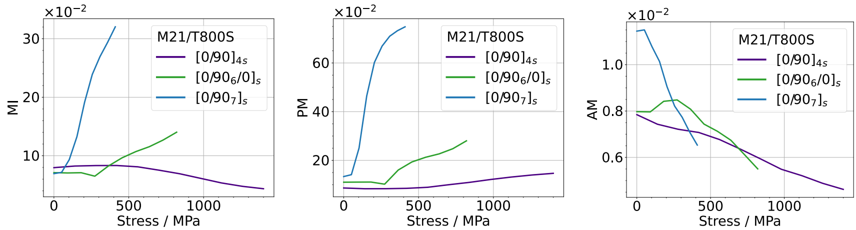

Figure 5.10: Modulation index (left), phase modulation (center) and amplitude modulation (right) of CFRP cross-ply laminates at 200 kHz carrier frequency and 3 Hz pump frequency after initial and continuous stepped loading with $[0/90]_{4s}$, $[0/90_6/0]_s$ and $[0/90_7]_s$ configuration.

Open-Hole Tensile Tests

Since the step-wise tensile tests on the CP specimens have shown that different types and degrees of damage in the form of matrix cracking and delamination can be monitored using VAM, the detection of damage in the OHT specimens is now being tested. Monitoring these structures is particularly important due to the stress concentrations and thus localised damage occur along the holes, which can lead to early failure. Additionally, conventional joining techniques such as welding, riveting, and fastening with additional weight are used to take into account these high local stress concentrations.

Figure 5.11 represents the stress-strain curves of quasi-isotropic OHT specimens during quasi-static tensile testing with ply- and sub-scaling lay-up. Overall, the three tested sub-scaling specimens exhibit a clearly defined linear-elastic behaviour. A small stress decrease corresponding to inter-fibre failure indicates the initial significant damage in the representative curve at 640 MPa, followed by several smaller inter-fibre failure until final failure. However, the ply-scaled specimens experience initial damage at approximately 280 MPa, recognisable by the decreasing stiffness, with severe delamination occurring above 500 MPa, which is in good agreement with the results of Nixon et al. [86]. These results demonstrate varying damage behaviour in OHT laminates, ranging from complex delamination (ply scaling) to brittle failure (sub-scaling) [8–12]. The young's modulus is the same for both laminates due to the same number of layers with the same fibre orientation. The ultimate tensile strength of 743 MPa for the sub-scaling specimen and 580 MPa for the ply-scaling specimen is higher compared to Nixon et al. [86], which results from the higher tensile strength of the T800s carbon fibres.

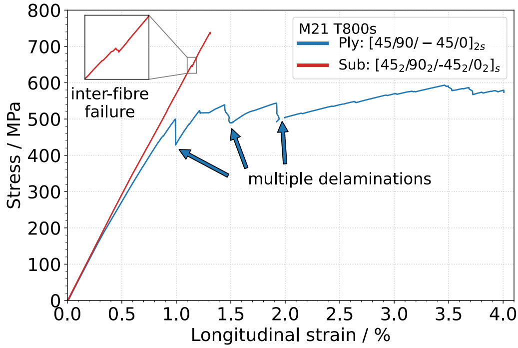

Figure 5.11: Stress-strain curves of ply- and sub-scaling quasi-isotropic OHT specimens for typical quasi-static tensile tests.

Fig. 5.12 shows the comparison of the results of stepwise tensile tests for representative sub- and ply-scaling specimens, including stress, amplitudes of the MI up to the fourth order and the average frequency of the AE signal resulting from damages. Colour-coded frequency ranges indicate where inter-fibre fractures, delamination, and fibre-matrix debonding occur. The first measurable minor damage in the form of matrix cracking and delamination can be seen in the sub-scaling specimens between 350 and 400 MPa. In this stress range, no equivalent stress reduction was observed in the quasi-static tensile tests, indicating discontinuous matrix cracking that did not extend over the full width of the specimen. However, the damage is closely correlated with a slight increase in the third and fourth order modulation indices. As the load increases, the number of AE hits and the frequencies at which they are detected also increase. This leads to fibre-matrix detachments between 400 and 500 MPa, which continuously increase the modulation indices. Additionally, crack saturation is visible due to the flattening of the modulation indices and the decreasing intensity of the AE hits.

Initially, the MI's of the ply-scaling specimen remain constant until 250 MPa stress, which can be interpreted as low damage, analogous to the linear-elastic range (see Fig. 5.11). This can be confirmed by the AE signal, with only a few hits below 150 kHz that can be attributed to small matrix cracks and local delaminations of CFRP [198, 298]. After this initial phase, the MI slopes increase continuously, which correlates very well with the increased number of AE hits. Fibre-matrix debondings begin at 360 MPa and are detectable and assignable in the 200-300 kHz frequency range [198, 298, 299]. Above 420 MPa, both the detected hits and modulation indices increase, while the stress curve shows no significant change. Crack saturation occurs at the final stress level.

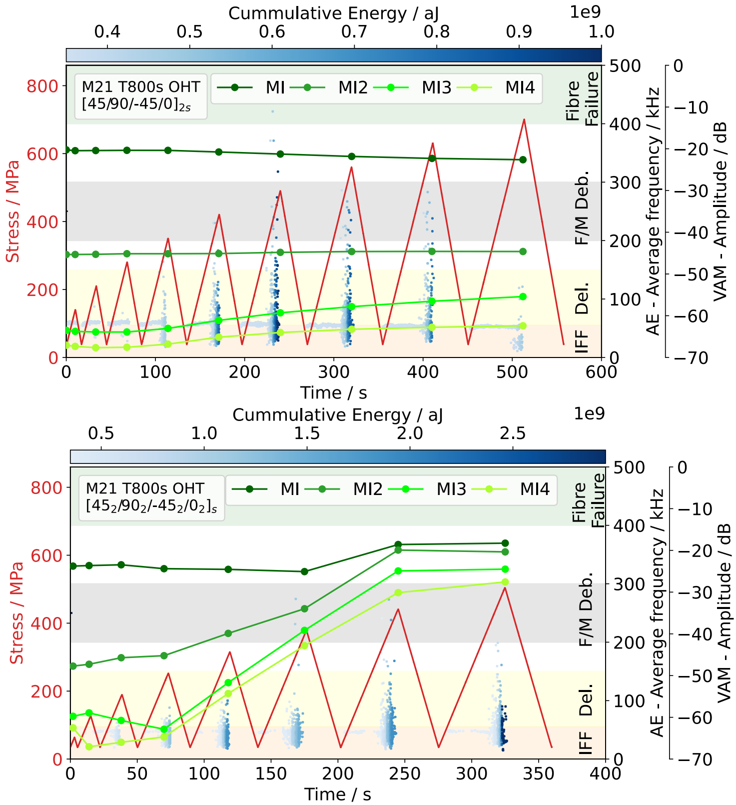

Figure 5.12: Representative results of step-wise tensile tests on OHT laminates with Sub-Scaling $[45/90/-45/0]_{2s}$ (top) and Ply-Scaling $[45_2/90_2/-45_2/0_2]_s$ (bottom) layup including stress, average frequency of AE signal and amplitudes of MI up to fourth order; IFF refers to inter-fibre failure.

Moreover, the comparison illustrates the smaller inter-fibre failures observed in the sub-scaling specimens at higher stresses (above 500 MPa) and higher frequencies, which produce a lower cumulative energy compared to the ply-scaling specimens. The AE cumulative energy remains below 1 aJ (sub) and up to $2.85 \cdot 10^{\mathbf{9}}$ aJ (ply) respectively and correlates with the increase of the MI amplitudes. These results of the AE measurements follow the in-situ effect due to the different ply thickness. The lower ply thickness shifts the initiation of inter-fibre failures towards higher strains and prevents the propagation and subsequent delaminations trough the increased number of differently orientated layers, which is confirmed by Yokezi et al. [124], analogous an elongated guitar string rupturing.

The chirp and FFT signals of the OHT laminates during the stepped tensile tests in Fig. 5.13 and Fig. 5.14 confirm the increased damage initiation in the ply-scaling specimens. The frequency curve of the chirp signal for the sub-scaling specimens remains almost constant over the tested stress range with a slight reduction in signal strength. However, the signal strength of the ply-scaling specimens is significantly reduced from 400 MPa applied stress. Additionally, the frequency shift is much more pronounced in the ply scaling specimens. The occurrence of more sidebands with a higher degree indicates higher damage initiation in the ply scaling specimens.

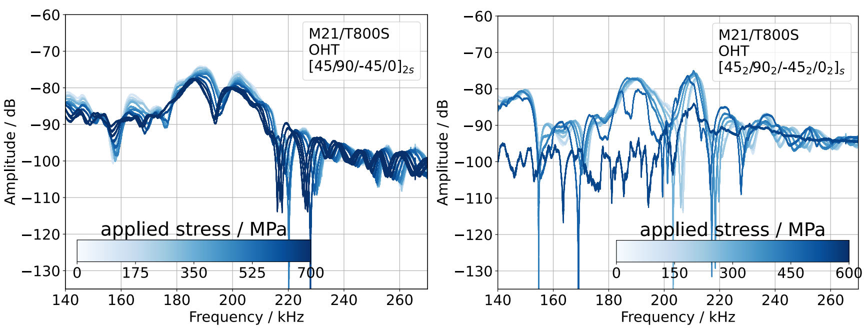

Figure 5.13: Chirp signal of CFRP OHT laminates at 3 Hz pump frequency after initial and continuous stepped loading with $[45/90/-45/0]_{2s}$ (left) and $[45_2/90_2/-45_2/0_2]_s$(right) configuration.

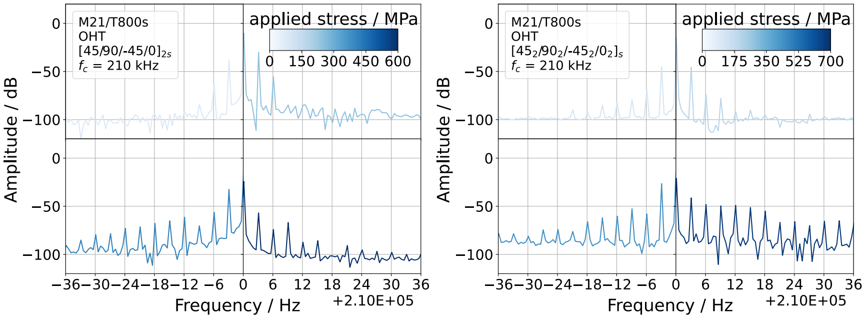

Figure 5.14: FFT signal of CFRP OHT laminates at 3 Hz pump frequency after initial and continuous stepped loading with $[45/90/\text{-}45/0]_{2s}$ (left) and $[45_2/90_2/\text{-}45_2/0_2]_s$(right) configuration. The areas of the negative and positive sidebands are shown in the respective quadrants according to the associated load.

5.3 Fatigue tests

5.3.1 Unnotched Laminates

Fatigue tests of thickply laminates

Cross-ply laminates

In the following, the mean amplitudes (left and right sideband) for the first three sidebands, the MI, and the relative stiffness are presented for three exemplary CP specimens in Figure 5.15. The sidebands and the MI are averaged over the entire frequency range (185-230 kHz). The relative specimen stiffness describes the ratio between the stiffness after cycle n and the initial stiffness. Generally, the stiffness is calculated according to the tangential modulus of each hysteresis curve. Due to the differences in the layups, the maximal load was adjusted to 65 % of the maximum tensile strength, resulting in fatigue stress amplitudes of $\sigma_{\mathrm{A,F}} = 187\,\mathrm{MPa}$ for $[0/90_7]_s$, $\sigma_{\mathrm{A,F}} = 234\,\mathrm{MPa}$ for $[0/90_6/0]_s$ and $\sigma_{\mathrm{A,F}} = 500\,\mathrm{MPa}$ for $[0/90]_{4s}$. These presented specimens were stopped after $3.4 \cdot 10^{4}$ cycles ($[0/90_7]_s$), $3.3 \cdot 10^{4}$ cycles ($[0/90_6/0]_s$) and $1.7 \cdot 10^{5}$ cycles ($[0/90]_{4s}$) due to crack saturation before final failure.

After the initial loads, the sideband amplitudes of the $[0/90_7]_s$ and $[0/90_6/0]_s$ laminates increase only marginally, while the sideband amplitudes of the $[0/90]_{4s}$

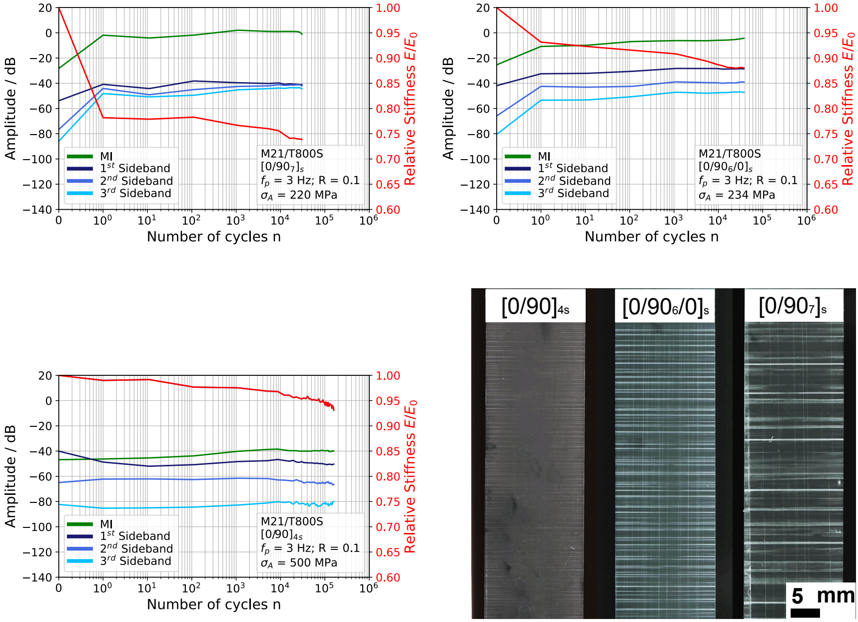

Figure 5.15: Representative results of fatigue tests on CP laminates with $[0/90_7]_s$ (upper left), $[0/90_6/0]_s$ (upper right) and $[0/90]_{4s}$ (lower left) layup including relative reduction of the specimen stiffness E/E_0, MI and amplitudes of first three sideband over number of cycles tested with stress ratio R=0.1. Corresponding negative x-ray scans after the respective cyclic loading are shown in the lower right section. White horizontal lines indicate the inter fiber-cracks in the 90° layers due to fatigue loading.

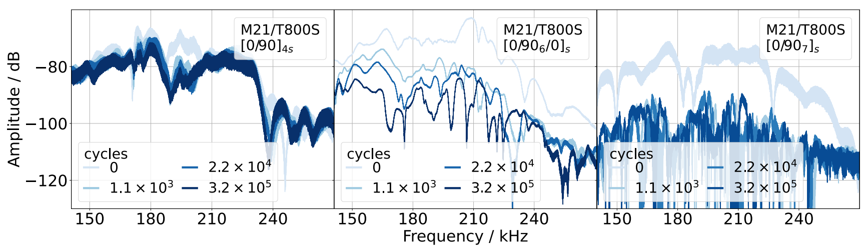

Figure 5.16: Chirp signal of CFRP cross-ply laminates at 3 Hz after initial and continuous fatigue measurement with $[0/90]_{4s}$ (left), $[0/90_6/0]_s$ (center) and $[0/90_7]_s$ (right) configuration.

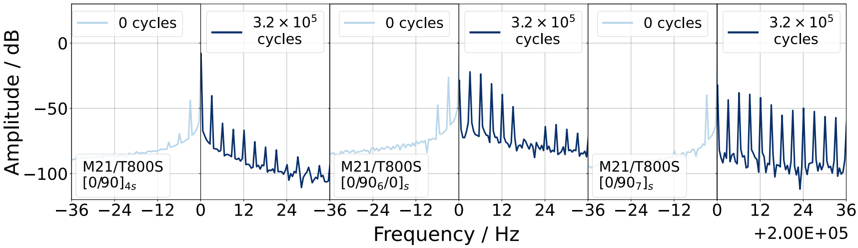

Figure 5.17: FFT signal of CFRP cross-ply laminates at 200 kHz and 3 Hz after initial and continuous fatigue measurement with $[0/90]_{4s}$ (left), $[0/90_6/0]_s$ (center) and $[0/90_7]_s$ (right) layup configuration. The FFT signal displays negative (left half-image) and positive sidebands (right half-image), which illustrate the damage propagation from the initial to continous number of fatigue cycles.

laminate remain almost constant. The highest increase in sideband amplitude is measured for the $[0/90_7]_s$ laminate followed by $[0/90_6/0]_s$. From the initial measurement to the beginning of the first fatigue cycle, the second sideband increase is more than twice as high as compared to the first sideband for the $[0/90_7]_s$. The remaining sidebands show a similar strong increase and a graded, identical curve as the second sideband. This strong increase is in very good agreement with the relative stiffness decrease by more than 20 %. The measured increase of the higher order sidebands after the first load has a magnitude of 35.4 ± 2.3 dB. A lower increase in the sideband amplitudes after the first load is observed for the $[0/90_6/0]_s$ specimens. The first two sidebands increase by 6.2 ± 1.1 dB and 18.4 ± 1.7 dB respectively, while the increase of the higher sidebands is 22.1 ± 0.8 dB. The measured amplitude change and MI show an excellent agreement with relative stiffness reduction to 10 %. In contrast, there is no significant increase in the sideband amplitudes and MI for the $[0/90]_{4s}$ laminate as they remain in the same order of magnitude. This correlates well with the small relative stiffness reduction of 2 % after first load cycle. Regarding CP-laminates in general, the cracks in the first cycles have the strongest influence on the sideband amplitudes and the MI. Furthermore, these VAM characteristics remain in the same order of magnitude since crack saturation occurred, which is consistent with a weakly decreasing stiffness.

Similar to the stepped tensile tests of the CP specimens, the chirp and FFT signals of the corresponding ply structures exhibit distinct characteristics (see Fig 5.16 and Fig 5.17) . In the case of the $[0/90]_{4s}$ specimens, the signal strength gradually decreases across the entire frequency range until crack saturation is achieved. This trend is also evident in the $[0/90_6/0]_s$ specimens, albeit with a more significant decline in signal strength. The $[0/90_7]_s$ specimens exhibit a sharp drop in signal strength after the first load cycle, resulting in a diffuse frequency response. This is caused by the large inter-fibre breaks, which are not impeded by a 0° layer. As a result, the Lamb waves can propagate with reduced efficiency within the CFRP. After the applied load cycles, the number of sidebands occurring in the FFT signal is identical for all CP laminates, while the height of the sideband amplitudes increases significantly with a higher number of 90° layers.

The correlation between MI and specimen stiffness is shown in Figure 5.18. In this context, the relative stiffness was reconstructed based on MI. The functions approximate the MI curves of the CP specimens particularly well. In the case of $[0/90_7]_s$ and $[0/90_6/0]_s$ specimens, R^2 is 0.93 and 0.96, respectively. However, the function also follows the stiffness curve for the $[0/90]_{4s}$ specimen. With an R^2 of 0.66, the fit curve is not so well approximated, which might result from the stiffness decrease due to the fatigue cracks being relatively small and the MI not increasing much either.

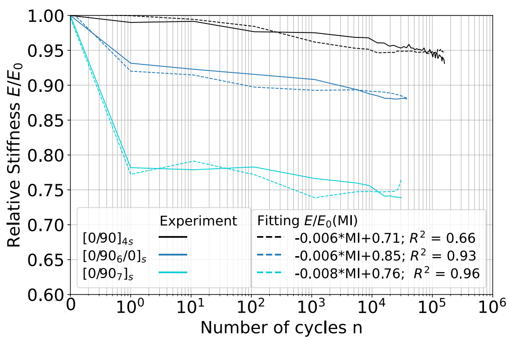

Figure 5.18: Correlation of the specimen stiffness E/E_0 on CP laminates with $[0/90_7]_s$, $[0/90_6/0]_s$ and $[0/90]_{4s}$ layup by using the MI. The solid lines indicates the relative stiffness, calculated from the tangential modulus of each hysteresis curve (stress-strain). The dashed lines shows the relative stiffness reconstructed from a linear correlation to the MI.

In the $[0/90_7]_s$ laminate with the highest 90° layer thickness, the inter-fibre cracks can spread over 14 adjacent layers, resulting in cracks with a high cross sectional area. The X-ray scans show that the total amount of cracks decreases with increasing adjacent 90° layers, conversely the amount of cracks running through the layer thickness and through the entire specimen width increases (see Figure 5.15). The measured width of the cracks in the $[0/90_7]_s$ and $[0/90_6/0]_s$ laminates varies between 0.6 and 1.1 mm, while in the $[0/90]_{4s}$ Laminates the crack diameter is between 0.1 and 0.3 mm. As a result a larger crack opening with high local strains by pump vibration generates a higher envelope amplitude and consequently the highest modulation. As expected, reducing the number of adjacent 90° layers prevents the crack propagation and results in defects with a smaller cross-section. Therefore, these cracks have less stiffness-reducing effect, resulting in minimal modulation change but an increase in the number of cracks. As a consequence, it can be determined that VAM provides more sensitive results with regard to the crack size (in relation to the cross-sectional area of the pump wave propagation) compared to the crack density.

Quasi-isotropic laminates

As depicted in Figure 5.19, QI specimens with a high layer thickness ($268\,\mathrm{g/m^2}$) show a completely different vibro-acoustic behavior during tensile fatigue load compared to CP laminates. To analyse the damage state using a vibro-acoustic signal, different criteria were applied. Firstly, the signal was analysed in the time and frequency domain. In this case, the response signal is shown representatively at 200 kHz in the time domain. Secondly, X-ray scans of the specimens were made at characteristic points of the stiffness condition. The linear sideband amplitude and MI increase is in very good agreement with the linear relative stiffness reduction until 4681 load cycles. The X-ray scan after 1111 cycles indicates that multiple inter-fibre fractures have developed in the ±45° and 90° layers. Pronounced cracks are visible on the outside of the specimen. With progressive fatigue loading, an exponential stiffness reduction accompanies it. In this phase, high interlaminar shear stresses occur at these inter-fibre fractures and lead to shear cracks, which develop into increasingly larger delaminations under fatigue load. Based on the X-ray image, it is evident that the delaminations spread from the edge of the specimen, extending into the centre. These delaminations are located at the strongest stiffness gradient, between the 0° layers in the middle and the adjacent 45° layers.

Furthermore, the progressive separation of the individual layers leads to friction at the individual layers with the initiation of longitudinal oscillation. As a result, the vibro-acoustic response signal in the time domain is influenced by additional vibrations. It deviates from a pure sinusoidal envelope as seen with inter-fibre fractures to more complex oscillations in a sine-like shape.

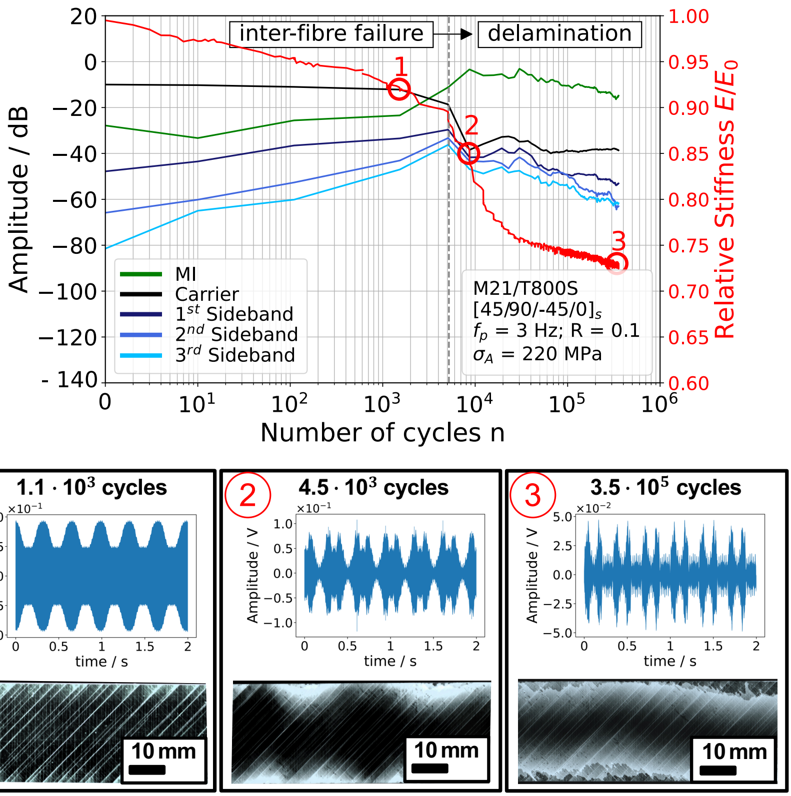

Figure 5.19: Representative results of fatigue tests on a quasi-isotropic [45/90/-45/0]$_s$ CFRP laminate with 268 g/m^2 - showing relative stiffness E/E$_0$, amplitudes of carrier, MI and first three sidebands over number of cycles tested with stress ratio R=0.1 and corresponding x-ray images for three specific damage states. White lines indicate inter-fibre cracks along the respective fibre orientation, while large white areas show edge delamination growth in single or multiple layers due to fatigue loading.

The increase of the interfaces due to the delaminations is an explanation for the decrease of carrier and sideband, which can also be seen in Figure 5.20 left. The number of sidebands increases with the number of fatigue cycles. However, the signal strength decreases from the time of global delamination, as shown in Figure 5.20 right, due to a clear drop in the signal over the entire frequency response. Prior to this, inter-fibre failures and local delamination successively reduce the signal strength, but no frequency shift is discernible. The decrease of the carrier amplitude is stronger than the decrease of the first sideband, hence the MI increases. In addition, once the single layers are delaminated, the Lamb waves will not propagate within the entire specimen thickness, but only in the last contiguous layers at the surface of the piezoceramic. After the specimen has passed through the exponentially decreasing stiffness range in which the first delaminations occurred, a relatively constant plateau follows in which the damage continues growing and a slight but continuous stiffness reduction becomes detectable until the final failure occurs. The increasing amount and propagation of delaminations is visibly confirmed in the X-ray scan and in the more pronounced deviation of the sinusoidal signal of the envelope in the time domain.

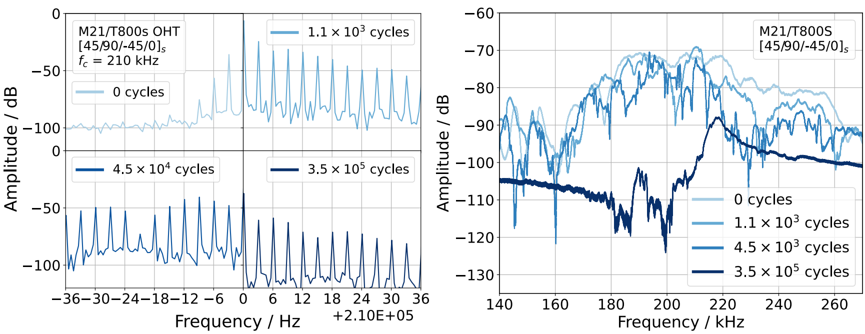

Figure 5.20: FFT signal (left) and chirp signal (right) of a quasi-isotropic CFRP laminate $[45/90/\text{-}45/0]_s$ with at 3Hz after initial and continuous fatigue measurement with fibre areal weight of 268 g/m^2. The FFT areas of the negative and positive sidebands are shown in the respective quadrants according to the associated fatigue cycles.

5.3.2 Fatigue tests of thinply laminates

The results of the tension-tension fatigue tests of thinply laminates are shown in Figure 5.21. The diagramm on the left-hand side represents the relative reduction of the specimen stiffness with a fatigue stress amplitude of 220 MPa. The typical stiffness curve of QI fibre composite is observable in all laminates. The initial area where the number of inter-fibre breaks increases and propagates, resulting in a constant linear decrease in stiffness, sustains longer in the thinply laminates with 30 and 60 g/m^2. Among the thinply specimen with 120 g/m^2 as well as the thickply specimen with 268 g/m^2, the inter-fibre fractures result in delaminations, which can be identified by the pronounced decrease in the stiffness curve. Koetter et al. [300] obtained similar mechanical curves after tension-tension fatigue tests with this configuration. With an increase of the fatigue amplitude to 275 MPa, even in the 60 g/m^2 specimen some local delaminations occur but the general damage behaviour is characterised by a brittle nature with dominating inter-fibre fractures. This mechanical behaviour agrees very well with the vibro-acoustic measurement results. With regard to the specimen with delamination-dominant behaviour (120 g/m^2 and 268 g/m^2), the sideband amplitudes increase until 44.2 ± 2.3 dB for 268 g/m^2 respectively 35.1 ± 1.4 dB for 120 g/m^2 with inter-fibre fractures occurrence. This shows a stronger increase in sideband amplitude with higher layer thickness and indicates an earlier onset of the increase. These findings are in good agreement with the results from the CP laminates, where the increase of sideband amplitudes is more pronounced with increasing crack size and length. However, the fatigue amplitude maximum, the threshold for delamination, is also reached earlier with higher layer thickness. This is well reflected in the relative stiffness curve. The reason for these mechanical results is analogous to the QI laminates with high layer thickness and characteristic for QI laminates with the occurrence of large-area delaminations. In contrast, for the specimens with inter-fibre failure-dominant damage behaviour, only an increase in sideband amplitudes is evident, which is less pronounced. The sideband amplitudes of the 30 g/m^2 specimen with smaller crack size increases by 6.2 ± 1.1 dB, while the 60 g/m^2 specimen increases by 25.4 ± 1.9 dB.

The mechanical and vibro-acoustic behaviour of the thinply laminates with 30 and 60 g/m^2 fibre areal weight is confirmed by the chirp and FFT signals (refer to Fig G.2 and G.3 in Appendix). The signal strength of the chirp signal decreases with increasing number of fatigue cycles, but a frequency shift is not

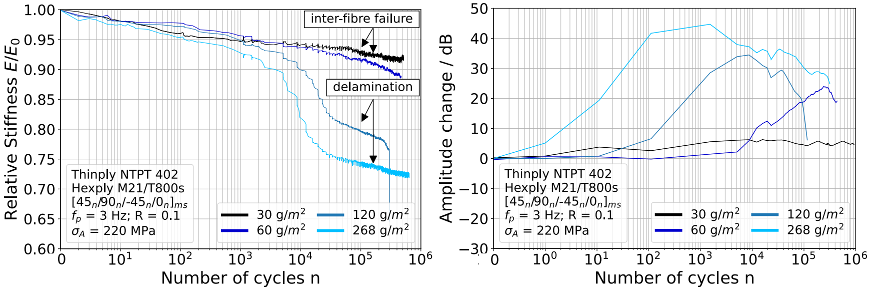

Figure 5.21: Fatigue results with relative reduction of the specimen stiffness E/E$_0$ (left) and change of (representative) 3rd sideband amplitude (right) on quasi-isotropic laminates with different fibre areal weight (30, 60, 120 and 268 g/m^2)

visible. However, thinply laminates with delaminations show a decrease in signal strength of up to 40 dB, which is observed in the thickply structures with 268 g/m^2. The most significant drop is noticeable after the sideband maximum occurs. The FFT signal also indicates an increased level of damage due to the number and height of the sidebands present in the 120 g/m^2 specimens. Similarly, the 30 and 60 g/m^2 specimens, which have a comparable level of damage, exhibit a similar FFT signal.

Figure 5.22 illustrates the resulting fatigue life of the thinply structures (30,60 and 120 g/m^2), plotted as S-N curves for the tested stress amplitudes. Solid lines indicate the calculated failure probability, at which the specimens will fail at a specific stress amplitude. This fitting curve is based on the Palmgren-Miner equation (eq. 2.1). This S-N diagram was extended by adding the moment when the VAM maximum occurs as a dashed line, also fitted by the Palmgren-Miner equation. The 268 g/m^2 specimens were not shown here, as the T800s fibres offer significantly better fatigue performance compared to the T700s fibres of the thinply specimens. The failure probability of the 120 g/m^2 specimens is shifted to reduced fatigue life compared to the 30 and 60 g/m^2 specimens, which confirms the suppressed formation of delaminations, a brittle failure and better fatigue performance at lower layer thickness. Both 30 and 60 g/m^2 specimens have a similar slope of its S-N curve and are equally sensitive to failure behaviour. In general, the higher the applied stress amplitude of the fatigue load, the earlier the specimens fail and the maximum of the sideband amplitude is also reached earlier. The difference between the occurrence of the sideband maxima and the failure of the specimens thus determines the remaining service life. As the stress amplitude increases, the remaining service life decreases, irrespective of the layer thickness. Consequently, specimens subjected to a stress amplitude of 275 MPa still exhibit cycles in the range of 10^4 after reaching the sideband maxima, whereas specimens subjected to a stress amplitude of 220 MPa have a remaining service life in the range of 10^5 cycles. Thus, the observation of the S-N curve extended by the sideband maxima serves not only to identify the occurrence of delamination, but also to determine the remaining service life, which is a unique feature in VAM analysis. The slope resulting from the maximum amplitude of VAM measurements is shifted to lower cycles at higher layer thickness similar to the S-N curves. The calculated Wöhler exponents k from (eq. 2.1) are averaged from the S-N curve and the VAM measurements and are comparable to literature values of composites [301–303] at 8.20 for 120 g/m^2, 14.43 for 60 g/m^2, and 16.24 for 30 g/m^2 specimens. Exponents of thinply laminates have not been presented in literature. The small standard deviation shows that both predictions are in very good agreement and even for fatigue prediction the vibro-acoustic signal correlates with the mechanical behavior. The Wöhler exponent increases with decreasing layer thickness and the resulting useful lifetime is extended, allowing extended maintenance intervals.

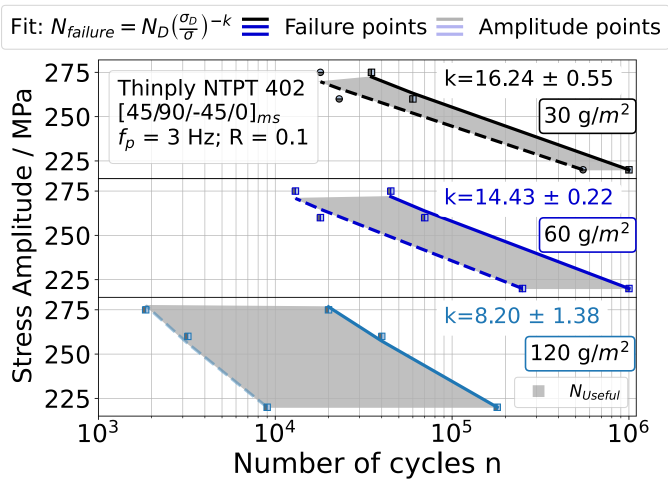

Figure 5.22: S-N curves of CFRP thinply laminates with fibre areal weight of 30, 60, 120 g/m^2 (from top to bottom) showing the maximum sideband amplitude clearly before failure with a resulting useful life filled in grey (right) at load ratio of R=0.1

5.3.3 Notched laminates

Statistically distributed damage within standard thick- and thinply CFRP structures could be detected over the service life. The delamination extended over the entire specimen geometry. In OHT laminates, further investigation is required to determine the impact of local stress concentrations, where delamination nucleates, on the course of the VAM signals.

A detailed analysis of VAM in sub- and ply-scaling specimens during fatigue testing is given in Fig. 5.23 and Fig. 5.24, which show the MI amplitudes and the relative stiffness change for a representative specimen with stress amplitudes of 180 MPa (sub-scaling) and 115 MPa (ply-scaling). The relative stiffness of the specimens decrease continuously by -10 %. This decrease in stiffness can be related to the initiation and growth of matrix cracks in ±45° and 90° layers around the hole, which is clearly demonstrated by both X-ray images up to this point. In these ranges, both configurations' chirp signals exhibit a slight, continuous decrease in signal strength across the entire frequency response (refer to Fig. G.4 in Appendix). Simultaneously, there is a noticeable increase in the sidebands (refer to Fig. G.5 in Appendix). In this linear decreasing stiffness regime, the MI amplitudes have the inverse behaviour of the stiffness with a similar shape. Stiffness reduction leads to an increase in the MI amplitudes, with the first-order MI appearing to be more sensitive. For sub-scaling specimens a 5 % decrease in stiffness results in a doubling of the MI amplitude, while the maximal MI is reached at approx. 10 % decrease. The sub-scaling specimens have a final MI of 0.31, the MI measured for the ply-scaling specimens is 0.22.

Inter-fibre failures under continuous loading result in high inter-laminar shear stresses, which cause shear cracks that eventually develop into multiple delaminations. Both the pronounced cracks and delaminations of the ply-scaling specimens are also evident. The measured VAM values of the ply-scaling specimens are basically similar, but the MI amplitudes maxima occurs when an exponential drop of stiffness due to delaminations is recognized. This can be probably explained by the stiff 0° core, consisting of 8 layers, is separated from the other 45° and 90° layers and is probably no more detected by the piezoceramic actuator applied on the outside. Considering the different modulations, it is noticeable that the amount of AM is very low compared to PM. The curve of the first-order MI also shows that it is strongly PM-driven, which is an indicator for the occurrence of higher-order sidebands (see Fig. G.5).

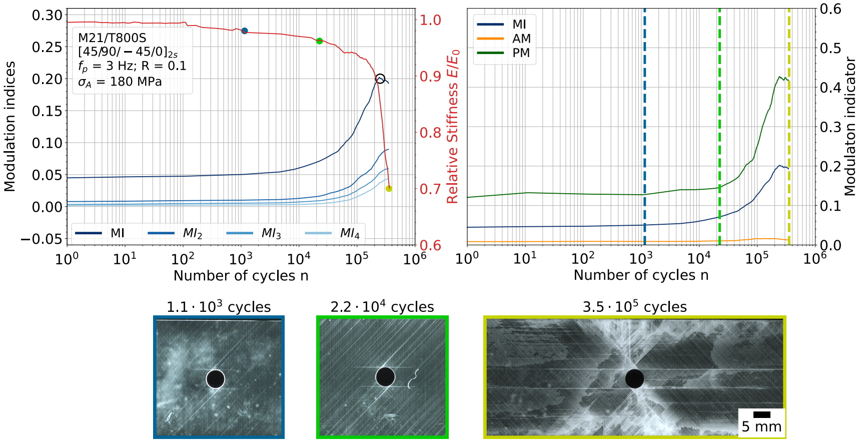

Figure 5.23: Representative results of fatigue tests on a quasi-isotropic sub-scaling OHT laminate $[45/90/\text{-}45/0]_{2s}$ - showing relative stiffness E/E_0, amplitudes of first four MIs with MI maximum marked in black (upper left) and AM, PM as well as MI as a comparative value (upper right) over number of cycles tested with stress ratio R=0.1. The maximum of MI amplitude is marked in black. Corresponding x-ray images of other specimens at this fatigue level focused on the drill hole for three specific damage states (lower middle).

Similarly to the unnotched tensile specimens, the maxima of the VAM amplitudes correlate well with the occurrence of delaminations in OHT specimens. Here, the threshold from the increase to the decrease of the amplitudes can be attributed to delaminations along the hole. The higher the degree of large-area delaminations, the stronger the amplitude reduction, which is evident by comparing the sub- and ply-scaling specimens. Delaminations are typically an exclusion criterion for further operation of a fibre-reinforced polymer component, regardless of the application. The VAM signal changes during fatigue indicate an increase in modulation with pure inter-fibre failures, and this range can be analysed clearly. Additionally, the delamination is visible from the sharp drop in signal strength of up to 25 dB in the chirp measurement (see Fig. G.4). This effect is more pronounced with higher individual layer thickness. The number of sidebands remains constant in the delaminated state, although the amplitude has decreased. Although there is no clear literature on this significant change from inter-fibre failures to delaminations, which can be quantitatively determined based on stiffness, it represents a characteristic point in the VAM.

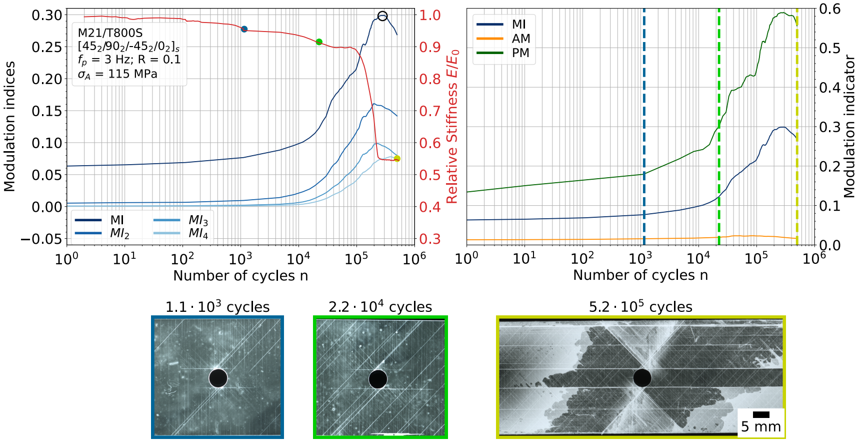

Figure 5.24: Representative results of fatigue tests on a quasi-isotropic ply-scaling OHT laminate $[45_2/90_2/\text{-}45_2/0_2]_s$ - showing relative stiffness E/E_0, amplitudes of first four MIs with MI maximum marked in black (upper left) and AM, PM as well as MI as a comparative value (upper right) over number of cycles tested with stress ratio R=0.1. Corresponding x-ray images of other specimens at this fatigue level focused on the drill hole for three specific damage states (lower middle).

A similar correlation can be observed between the maximum values of the VAM amplitudes and the occurrence of delamination in OHT specimens in Fig. 5.25, as is the case with the unnotched CFRP laminates. Specimens with 536 g/m^2 areal weight reach the VAM maximum at the same fatigue load earlier and a higher level compared to the 268 g/m^2 specimens, which is indicated with the colored circles. Generating the S-N curve extended by the MI maximum, significant differences in the k exponents are obtained according to the Palmgren-Miner fitting with k=16.24± 2.41 for 268 g/m^2 and k=9.80± 1.77 db for 536 g/m^2 OHT laminates. With this approach, the safety factor of VAM is very high, making in possible to interrupt the operation of structural components with high localised stress concentration, long before the failure occurs.

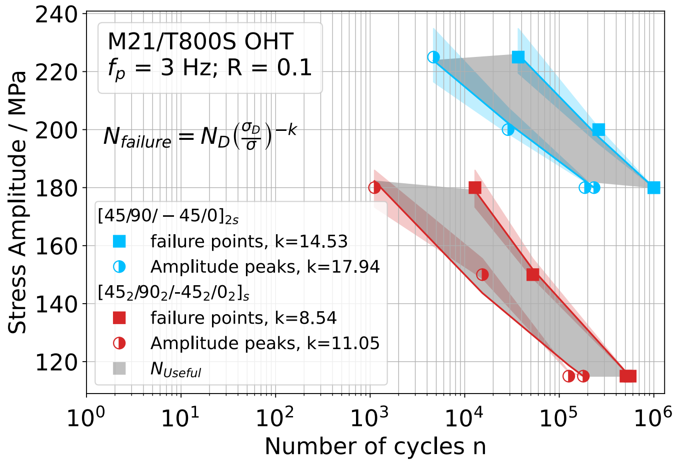

Figure 5.25: S-N curves of the OHT fatigue results showing the maximum MI amplitude clearly before failure with a load ratio of R=0.1

5.3.4 Fatigue after impact

Thinply Impacts

The previous sections demonstrated the detectability of matrix cracks, inter-fibre fractures, and delamination occurring in CFRP during stepwise-tensile and fatigue tests using VAM measurements. This section examines the applicability of VAM for the initial detection of impact damage as localised damage with concentration and its evaluation of influence on structural integrity is investigated as a consequent further development.

Using a representative force-time diagram of a 120 g/m^2 specimen with varying impact energies from 5 to 6.5 to 8 J (Fig. 5.26 left), the typical damage progression of thinply structures when an impact is applied is illustrated. The force progression is similar for all tested fibre areal weights and is characterised by a jagged progression. The pronounced drop in force at the beginning at around 0.2 ms indicates a strongly emphasised delamination as a result of the impact. As a result of the limited amount of deformation and the prevention of inter-fibre breaks in Thinply specimens, the elastic dissipation of energy is reduced and high shear stresses occur, resulting in delaminations. Kötter et al. [300] identified the formation of sublaminates due to the introduction of impact in thinply specimens. The number and extent of sublaminates depended on the

layer thickness. A sharp drop in force is consequently caused by the formation of these delaminations leading to sublaminates. The subsequent force drops are attributable to sudden material damage caused by small inter-fibre breaks and delamination, after the sub-laminates have developed.
The resulting extent of damage due to varying impact energy is shown for the specimens manufactured with different areal weights in Fig. 5.26 (right). Fundamentally, the damage pattern depends on the layer thickness. Typical failure behaviour of fibre-reinforced composites under impact loading is described in various studies [78, 79, 300]. The delamination pattern of the specimens changes significantly as the layer thickness decreases, which is reflected in a larger projected area of delamination on the C-scans. The typical damage behaviour observed in thinply structures with suppression of delaminations and inter-fibre fractures, where layer thickness decreases, can also be observed under impact insertion. Arteiro et al. [10] and Saito et al. [304] even showed a complete suppression of the inter-fibre fractures. The shape of the delaminations in the presented layer configuration remains in a circular shape. These images agrees well with the results of Kötter et al. [300], whose micrographs provide explanations regarding separable delamination areas that can be assigned to the layers in the $120\,\mathrm{g/m^2}$ specimens and why the damage patterns are similar in the 30 and $60\,\mathrm{g/m^2}$ specimens. According to Saito et al. [304], laminates with lower layer thickness show more fibre breaks and higher surface damage after impact. Due to the properties of thinner laminates, the impact damage on the specimen surface continues to grow and the impact energy is dissipated. This results in less indent deformation with less delamination surfaces. Accordingly, the $120\,\mathrm{g/m^2}$ specimens exhibit the highest proportion of delamination layers. These layers are not circular, but rather have the shape of a peanut. The high number of delamination layers leads to a dissipation of the impact energy through interlaminar inter-fibre failures and fibre fractures. According to Kötter et al. [300], the delaminations are located between the 0° and 45° layers and therefore spread preferentially in the direction of this fibre orientation. The ultrasound images confirm these observations through the presence of clear and concise delamination areas, which occur between defect depths of 0.5 and 1.5 mm.

Section 5.1 analysed the influencing parameters of the pump excitation on the VAM signal in undamaged UD tensile test specimens. As a result, the MI, AM and PM amplitude also increased based on the stress amplitude. The stress ratio R had no influence on the damage indicators in damage-free laminates. However,

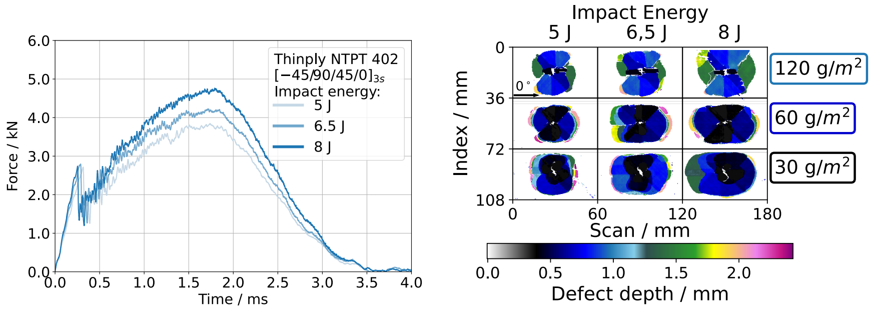

Figure 5.26: Representative force over time curves for impacts with 5 J, 6.5 J and 8 J impact energy on a 120 g/m^2 specimen (left). Ultrasonic C-Scan images of the impact damage for a potential impact energy of 5, 6.5 and 8J, from top to bottom: 120 g/m^2, 60 g/m^2 and 30 g/m^2 (right).

the stress ratio of the pump excitation significantly influences the MI when detecting impact damage in CFRP-Thinply structures using VAM measurement. For this purpose, different stress ratios were specified for the initial comparison of impact damages to thinply laminates (Fig. 5.27 left). Two stress ratios were selected in the tension-tension range: R=0.1 and R=0.3. Additionally, a stress ratio of R=-0.5, which is commonly used in the design of fibre composites, was chosen. In this case, the compression component represents half of the tensile component. Finally, a stress ratio of R=10 was selected, in which test specimens are only subjected to compression. The results of the initial measurement before and after the impact with varying impact energies show, on the one hand, that the MI increases with increasing impact energy. On the other hand, the two measurements in the tensile-tensile range confirm that the stress amplitude rather than the stress ratio influences the MI. Whereas in the tension-compression range, the MI before impact is about 50 % lower than measured under tension-tension conditions. However, as described in Fig. 4.2, the anti-buckling support is used for this purpose. However, this distance is reduced when the specimens are compared after the impact has been applied. Accordingly, the excitation is more sensitive in the tension-compression range. An explanation is given by the local spreading of the different damages. Whereas the cracks in the 45° and 90° layers are opened by strain, and thus, the modulation increases. The delaminations are closed by strain and opened by compression. The sensitivity of the VAM measurement increases as the proportion of com-

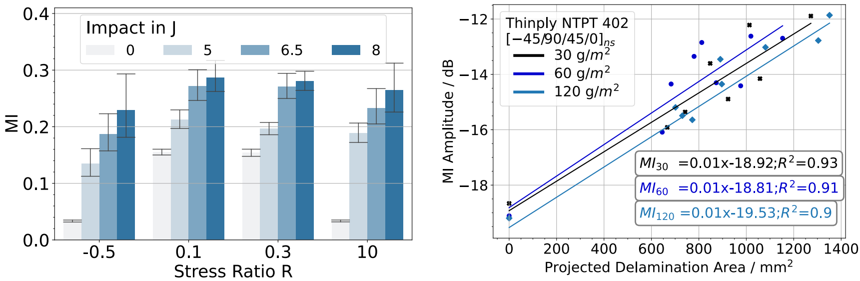

Figure 5.27: Barplot with resulting initial MI amplitude after different impact energies with varying stress ratio (left). Linear correlation between projected delamination area and MI amplitude for three different fibre areal weights under stress ratio R=0.1 (right).

pressive stress increases, up to the elimination of tensile stress caused by the expansion of delaminations.

The FFT signals in Fig. 5.28 confirm the observed behaviour. Sidebands up to the fourth order are strongly present in the tension-tension range, even in undamaged specimens. However, they are suppressed by the applied buckling support in the tension-compression range. The increase in sidebands after the impact is significant with both measurement methods, with a higher increase in the tension-compression range. However, the use of the buckling support also generates frictional effects on the specimen itself, which can lead to non-linearities. This circumstance also explains the occurrence of higher order sidebands in the undamaged state in comparison to the undamaged specimens that were tested under R=0.1. A differentiation of the non-linearities, which are due to friction effects or damage, was not carried out. However, the resulting delamination area is not sufficiently large to influence the friction surfaces of the buckling support, which rules out an increase in the frictional effects. Consequently, the increase in modulation is comparable in both stress conditions.

Compared to the UD measurements in the unloaded state Figure 5.4, it is evident that the ply structure strongly influences the VAM signal in both stress states. With 0° laminates, a maximum of 2 sidebands are formed, while QI laminates form sidebands up to the seventh order. This is caused by reflections of the individual layers with different fibre orientations, which are only slightly present in 0° laminates due to the uniform fibre orientation. The stress ratio R=10 used in the measurements is not necessarily application-related, as fibre-reinforced plas-

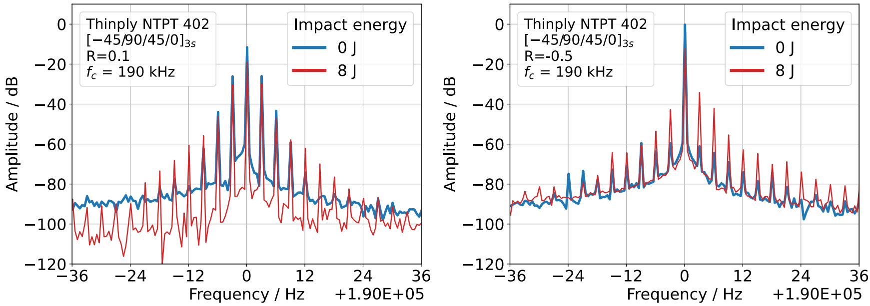

Figure 5.28: Comparison of the FFT signal different stress ratios in tension-tension (R=0.1) and tension-compression mode (R=-0.5) at initial and after an impact event with 8J impact energy. A representative CFRP thinply laminate with 120 g/m^2 fibre areal weight at 190 kHz carrier frequency and 3 Hz pump frequency is illustrated.

tic composites are not typically designed for compression. However, it provides a good example of the influence of the type of damage. The impact damage can be detected using the buckling support. The sensitivity increases with higher compressive stress due to the delamination. The linear correlation between MI amplitude and projected delamination area of thinply structures at stress ratio of R=0.1 is shown in Figure 5.27 (right). The functions approximate the MI curves of the of the 30, 60, and 120 g/m^2 Thinply specimens particularly well with R^2 from 0.9 until 0.93. The small deviation of the measured MI before impact–marked with 0 mm^2 delamination area–is a feature indicating a good reproducibility. Both the MI and the complete FFT and chirp signal (see Figure 5.29), including the occurring sidebands, characterise the damage state after the impact. As impact energy increases, the number and height of the sidebands increase. Meanwhile, a slight continuous decrease in signal strength is visible in the chirp signal. The comparison between undamaged and damaged specimens shows the highest decrease in signal strength at the beginning.

Figure 5.30 left illustrates representative Force-time curves of impacted thickply specimens in CAI configuration for the three impact energies 8 J, 15 J and 21 J. The energy resulting from the impact event is determined by integrating the force versus time curve and multiplying by the measured velocity of the impactor during the test. There is no noticeable loss of contact, and the contact time remains constant regardless of the impact energy. Compared to thinply structures, the force curve of this structure is less jagged due to the use of high-modulus T800s

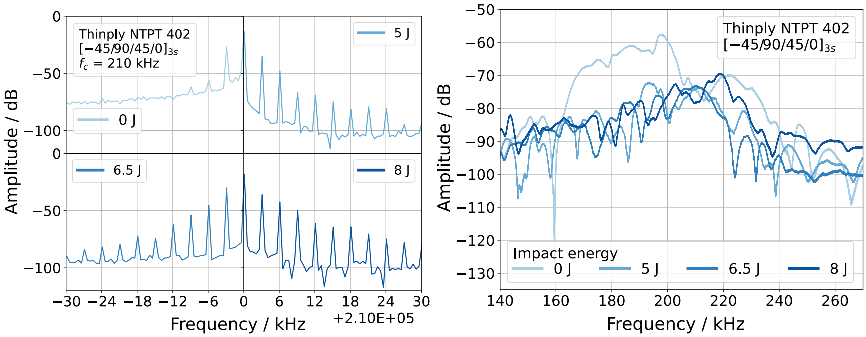

Figure 5.29: FFT signal (left) and chirp signal (right) of a CFRP thinply laminate with 120 g/m^2 fibre areal weight at 210 kHz carrier frequency and 3 Hz pump frequency after initial and after several impact events with 5, 6.5 and 8 J impact energy. The areas of the negative and positive sidebands are shown in the respective quadrants according to the associated impact energy.

fibres. These fibres increase the bending stiffness of the laminate and additionally with the thermoplastic particles toughened matrix, suppressing damage in the form of inter-fibre breaks or delamination. As a result, the force drop along the force curve is less pronounced. The ultrasonic c-scan images in the right part of Fig. 5.30 show the back wall echo of the damage as the reflection amplitude in dB, visualised by different colours. The impact results in delaminations and matrix cracks in the 45, 90 and 0 directions in the delaminated areas. At 8 J impact energy, the delamination has a circular shape, while the overall extent of damage increases significantly at 15 and 21 J. Matrix cracks form extensively in both 45° and 0° directions due to the high stiffness difference and and the double-layered 0° area.

In the frequency domain shown in Fig. 5.31, the sidebands with higher impact energy appear in increasing numbers and with increasing intensity. The strongest modulation is observed at 21 J, with successive sidebands appearing at 8 and 15 J. The chirp signal confirms the increasing damage with a continuous drop in signal strength. Unlike global delamination, which occurs in quasi-isotropic laminates above 60 g/m^2 under fatigue loading, an abrupt drop in signal strength or frequency shift is not observed in this case. A frequency shift is also not recognisable, which would occur with global damage due to the strain shift.

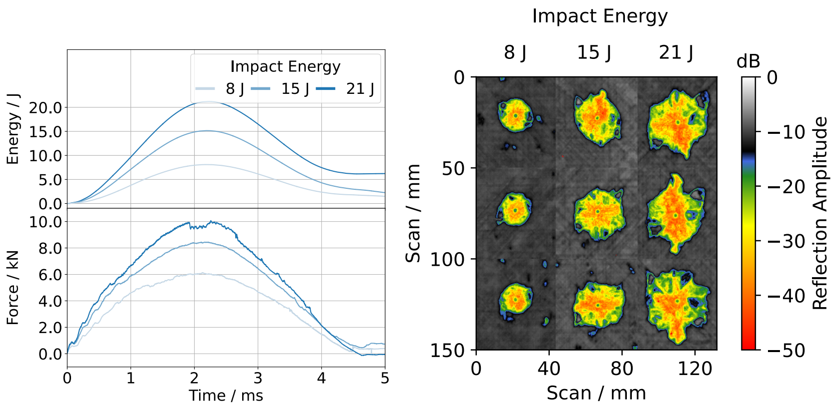

Figure 5.30: Representative force over time curves for impacts with 8 J, 15 J and 21 J impact energy on a 268 g/m^2 Hexply M21 CFRP laminate (left), including Ultrasonic C-Scan images of the impact damage for a potential impact energy of 8, 15 and 21 J, from left to right, each with three different specimens (right).

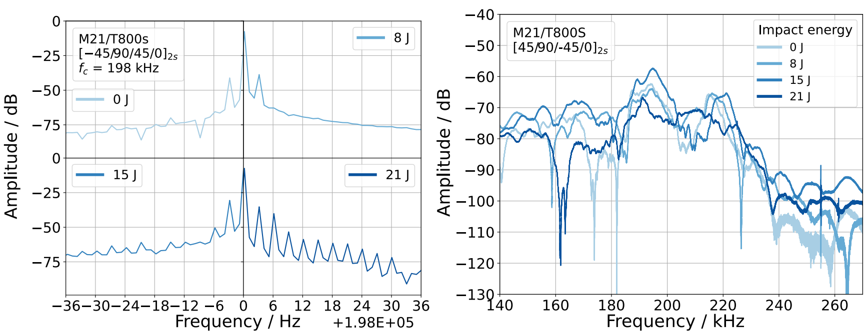

Figure 5.31: FFT signal (left) and chirp signal (right) of a CAI CFRP thickply laminate with 268 g/m^2 fibre areal weight at 210 kHz carrier frequency and 3 Hz pump frequency after initial and after several impact events with 8, 15 and 21 J impact energy. The areas of the negative and positive sidebands are shown in the respective quadrants according to the associated impact energy.

The measured MI for these different impact energies categorised by the signal path between the piezoceramic actuator combinations at a stress ratio of R=0.1 at CAI specimens is shown in Fig. 5.32, including the standard deviations. In this case, the signal paths for P1-P4 and P2-P3 pass directly through the impact damage, whereas P3-P4 propagates only though the pristine material. All measurements within this sensor network were carried out bidirectionally in the sense that receiver and transmitter were alternated for each measurement configuration. Here, an effect on the MI could not be determined. The assignment of the signal paths can also be seen in Fig. 4.1. The bar plot show a clear increase of MI with rising impact energies, but only for signal paths directly passing through the impact. The MI of the piezoceramic combination P3-P4 remains constant at different impact energies, which indicates that the impact damage detection is not possible in this measurement configuration. Compared to the 2.88 mm of the thinply specimens with FAI geometry, the specimen thickness of 4.08 mm and the larger measuring distances lead to a measured MI for the CAI specimens that is about a decade below its FAI equivalent.

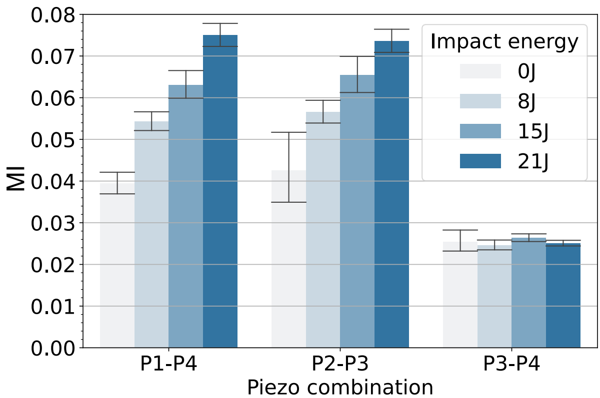

Figure 5.32: Comparison of MI amplitude of these impacted laminates for different signal pathways between the piezoceramic actuators at R=0.1.

A comparison of the MI over the entire frequency range in Fig. 5.33 confirms the high sensitivity of the VAM measurement when the damage is between the piezoceramic actuators. No deviation is recognizable in any frequency range in the case of the piezo combination P3-P4, which measures outside the impact damage. The mean values of the specimens with varying impact and undamaged specimens overlap with the standard deviation. Even though the chosen sensor

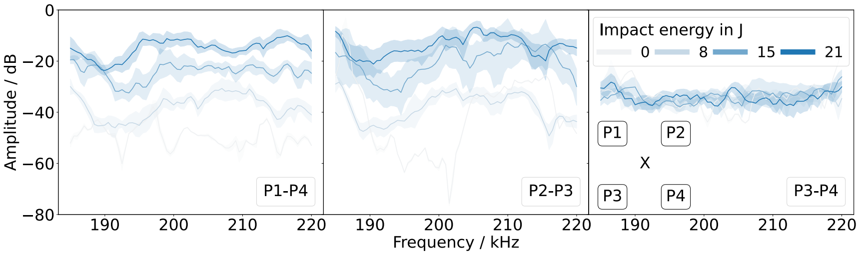

Figure 5.33: Average measured MI of all specimens with varying impact energy of 8, 15 and 21 J with the standard deviation as a shadow depending on the piezo measurement direction. The pictogram on the right indicates the localisation of the piezoceramic actuators on the specimens (analogous to Fig. 4.1). P1-P4 and P2-P3 corresponds to measuring direction crosses the impact (indicated by X), whereas P3-P4 is outside the impact measuring path.

network is subject to a laboratory-scale limited specimen geometry, a damage localisation based on the piezoceramic positions can be determined quite effectively. The sensitivity depends on the signal path, which allows a size estimation of the impact damage based on the magnitude of the MI increase.

Fatigue after impact

The mean amplitudes (left and right sidebands) for the first three sidebands, the MI and the relative stiffness are shown in Figure 5.34 for an exemplary 120 g/m^2 thinply laminate. The relative specimen stiffness describes the ratio between the stiffness at cycle n and the initial stiffness. Additionally, ultrasonic C-scans were performed on the impact area after 1111, $2 \cdot 10^{\mathbf{4}}$, and $1.5 \cdot 10^{\mathbf{5}}$ cycles to characterise the damage state during fatigue. As the mechanical behaviour of the 30, 60 and 120 g/m^2 specimens looks very similar, which is characterised in terms of stiffness decrease, the 30 and 60 g/m^2 specimens were not shown. The curves generally exhibit a first section with a constant decrease in stiffness, rather than the typical horizontal plateau observed in the tensile-tensile regime. The linear sideband amplitude increase agrees with this linear relative stiffness reduction until a maximum is reached at approximately $2 \cdot 10^{\mathbf{4}}$ load cycles. The MI also increases during this fatigue time, but its growth weakens once the sideband maximum is reached. A reversal point in the MI curve occurs at this moment. As the fatigue load continues, the sideband amplitudes decreases until a further clear drop at the end of the service life. Regarding the MI, which is the ratio between the carrier and sideband amplitudes, the decrease in carrier amplitude is considerably higher than the sideband amplitude. At the end of its service life, the MI reaches 0, ensuring that the carrier and sideband amplitudes are at the same level. From a methodological point of view, the MI as a damage indicator therefore offers the advantage that no reference measurement is necessary, in contrast to the sideband amplitudes. In fatigue tests conducted under tensile-tensile loading without any pre-damages, this increase in VAM amplitudes can be attributed to the inter-fibre failures. Accordingly, it is reasonable to assume that the propagation of the impact damage also leads to this vibro-acoustic behaviour under fatigue-after-impact tests with R=-0.5. A significant damage progression cannot be detected in the ultrasound images due to the similarity of the delamination patterns shown in the C-scans. On the other hand, ultrasound images have a limitation in identifying only the top layer of damage when there are multiple layers of damage. However, according to tomography images of thinply laminates captured by Kötter et al. [300] after approximately every decade of fatigue cycles, the damage growth increases with an increasing number of cycles, and a static damage state is reached.

The FFT signals and chirp signals after the stopped fatigue cycles indicate that no significant damage growth has occurred (see Figure G.6 in Appendix). The number of sidebands has remained constant, while only the height of the sidebands and the signal strength of the chirp signal are continuously decreasing. There are no recognisable signal strength drops resulting from delamination. The laminate exhibits none of matrix cracks propagation and the formation of delamination is prevented. Interlaminar shear stresses are insufficient for delamination growth. However, it is not possible to obtain reliable results regarding the absence of inter-fibre failures due to their small size, particularly in thinply structures, and hence would only be visible at very high resolutions.

Both the sideband amplitudes and the MI can be useful for predicting the service life of FAI tests on thinply structures. The MI increases to the value of 0 at the end of the service life, which can be considered a critical value in terms of structural integrity. In this context, the advantage of damage assessment based on the MI is that no reference measurement is required. Conversely, the determination of the maximum amplitude of sidebands always necessitates a historical view of the damage. On the other hand, since the VAM sidebands reach a maximum well before the final failure coinciding with the MI inflection point, this point represents a rather conservative approach to lifetime monitoring.

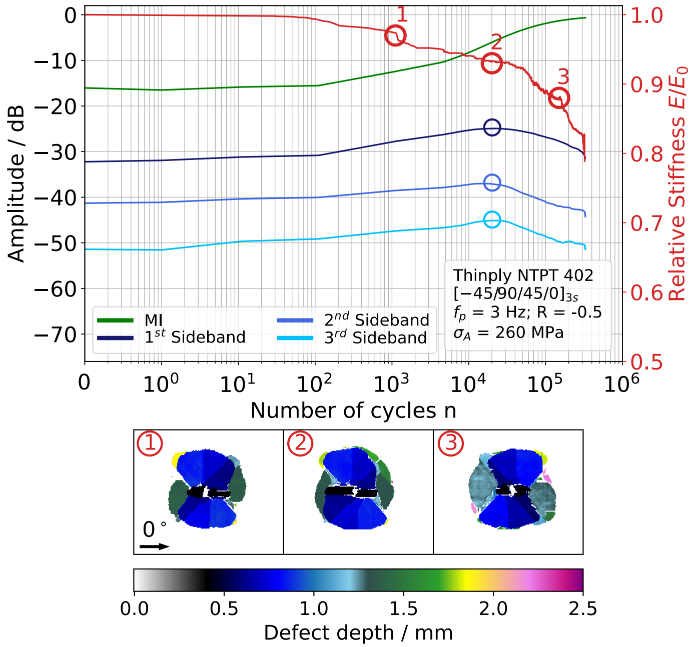

Figure 5.34: Representative results of fatigue after impact tests on a 120 g/m^2 quasi-isotropic thinply laminate $[45/90/\text{-}45/0]_{3s}$ with 5 J impact energy - showing relative stiffness E/E_0, amplitudes of MI and first three sidebands with sideband maximum marked in the respective colour over number of cycles tested with stress ratio R=-0.5. The damage pattern is demonstrated by corresponding ultrasonic C-scans following three specific fatigue steps.

In Fig 5.35, S-N-Curves of the 30, 60 and 120 g/m^2 specimens of the fatigue after impact tests are compared with those of the sideband maxima. The failure probability and VAM sideband maxima are fitted by the Palmgren-Miner-equation (eq. 2.1). These VAM maxima are highlighted with higher transparency and further shifted to a lower number of cycles with dashed or dotted lines due to higher impact energies. Lines with full opacity (S-N curves) show the calculated failure probability that 50 % of the specimens will fail after this number of cycles at a certain stress amplitude. Upon closer examination of the 30, 60 and 120 g/m^2 specimens, it is evident that the Wöhler curves exhibit a consistent negative slope. Consequently, the maximum of the sidebands occurs just before specimen failure occurs. As layer thickness increases, the cycle difference between the occurrence of the sideband maxima and the final failure also

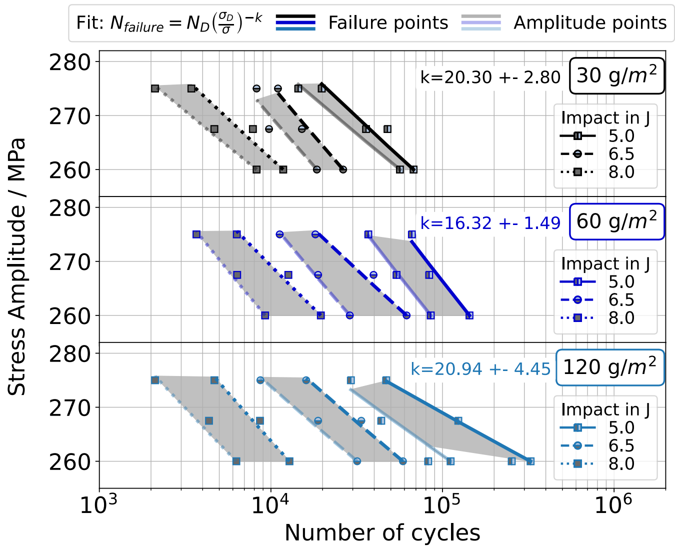

Figure 5.35: S-N curves of the fatigue after impact results of thinply laminates with 30, 60 and 120 g/m^2 showing the maximum MI amplitude clearly before failure with a load ratio of R=-0.5

increases. Additionally, the horizontal distance between the respective failure points is approximately equal. It is worth noting that the cycles are represented logarithmically. Thus, considering the fitting line at 5 J and 260 MPa, the specimens still have about $1 \cdot 10^{\mathbf{4}}$ cycles, whereas at 5 J and 275 MPa the distance is about $5 \cdot 10^{\mathbf{3}}$ cycles. The sideband maxima at 5 J and 260 MPa were observed in the 60 g/m^2 specimens at $2.5 \cdot 10^{\mathbf{4}}$ before the final failure and in the 120 g/m^2 specimens at $2 \cdot 10^{\mathbf{5}}$ cycles. Consequently, 30 g/m^2 specimens with a lower stress amplitude have a higher bound to failure. A change in the negative slope is evident in the 60 g/m^2 specimens. The calculated Wöhler exponents k from (eq. 2.1) are averaged from the S-N curve and the VAM prediction. With 20.3 for 30 g/m^2 specimens, 16.32 for 60 g/m^2 and 20.94 for 120 g/m^2, these values are higher than under tension-compression load. Whereas the scatter is significantly higher, which is cumulative with the scatter of damage initiation by the impact, as well as the scatter typically existing under fatigue load. The similar failure as well as VAM predictions of 30 and 60 g/m^2 specimen are consistent with the damage behaviour of the initial impact. Damage estimation, as well as monitoring using VAM, is applicable.

The VAM measurements on CFRP laminates indicate that the detection of damage in the form of inter-fibre failure and delamination is due to the vibroacoustic modulation caused by a systematic change in the laminate structure of CFRP. Service life monitoring can also include assessing the type and extent of damage, as well as providing a service life estimate based on maxima occurring in VAM sidebands. Consequently, a residual lifetime can be determined for all CFRP laminates where delamination occurs that generates amplitude maxima. This allows inspection and maintenance intervals to be adapted and, if necessary, limits for components to be extended and increases both sustainability as well as competitiveness. In the following section, VAM is evaluated as a non-destructive testing (NDT) and structural health monitoring (SHM) process for bonded joints in carbon fibre reinforced polymer (CFRP) materials, where the damage mechanism is related to the adhesive film.

5.4 Adhesive bonded CFRP structures

5.4.1 Initial measurement/Tensile test

The results of the tensile shear tests of the Sc and SLS specimens, including the configurations with introduced defects, are shown in Figure 5.36 as a box-plot diagram. In addition, the origin of the test specimens from differently produced laminates was colour-coded. The tensile shear strength of the Sc Pristine and PTFE specimens are comparable, with values of 23.33 ± 1.22 MPa and 24.64 ± 1.09 MPa, respectively, which aligns with the results of Harder et al. [185]. In contrast, the tensile shear strength of the release agent specimens is only 17.04 ± 1.63 MPa, which corresponds to a drop of 30.2 %. According to Harder et al. [185], the failure of scarfed joints with a QI laminate structure is significantly dominated by the stress concentration and the failure of the 90° layers is dominated by inter-fibre failures. As a result, a significant reduction in bond strength due to defects of 21.1 % of the bonded area is not observed as the influence of the stress concentration in the 90° layers is too high. Accordingly, the location of defects along the 0° layers with a proportion of about 5 % of the adhesive surface is of minor importance for the failure and the adhesive strength. However, the specimens with release agent on the adhesive surface show significantly lower strengths than those of the other specimen configurations. Due to the stress concentration of the finite thickness of the PTFE film compared to the release agent, a reduction in the shear strength of the PTFE specimen

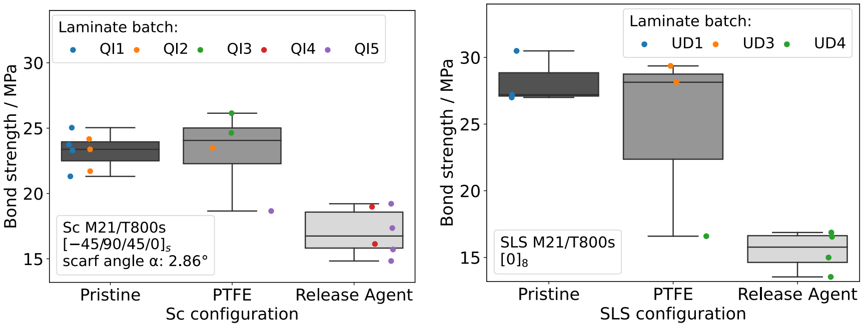

Figure 5.36: Box-plot including results of shear tensile tests on Sc and SLS CFRP specimens with specific induced defects. Colored Scatter points indicate the root of manufactured laminate.

would be expected. It is worth noting that every specimen made from panels QI4 and QI5 has a reduced strength, which can be attributed to the origin of the panels. The specimens from these panels were produced simultaneously in the same batch, indicating a manufacturing error. The same behaviour is observed in the SLS specimens. In terms of shear strength, no differences are found between the untreated specimens (28.23 ± 1.59 MPa) and those with PTFE film (24.69 ± 5.73 MPa). However, the specimens with release agent, which are produced in the same manufacturing process as the Sc specimens with release agent, have a shear strength of 15.49 ± 1.33 MPa, which is 42.04 % lower. In comparison to Boll et al. [187], where the introduction of PTFE and release agent with a defect area of 18 % resulted in a reduction in strength, no significant reduction in strength can be determined in this work with a smaller defect area of only 5 %. Importantly, the specimens with reduced shear strength from the manufacturing process were not used for fatigue testing and sorted out.

The failure behaviour of the bonded laminates can be seen in the fracture patterns shown in Figure 5.37. The representative images displays a pristine specimen, the specimen modified with PTFE and the specimen modified with a release agent (from left to right). The fracture patterns exhibit similar behaviour, characterised by mixed fractures with fibre fractures, inter-fibre fractures, delamination as well as cohesive and adhesive failure of the adhesive. The manufacturing defects in the test specimens modified with the release agent, therefore, affect the shear strength (see Figure 5.36), but not the general damage behaviour. Additionally, the defects can only be visually identified based on the missing adhesive.

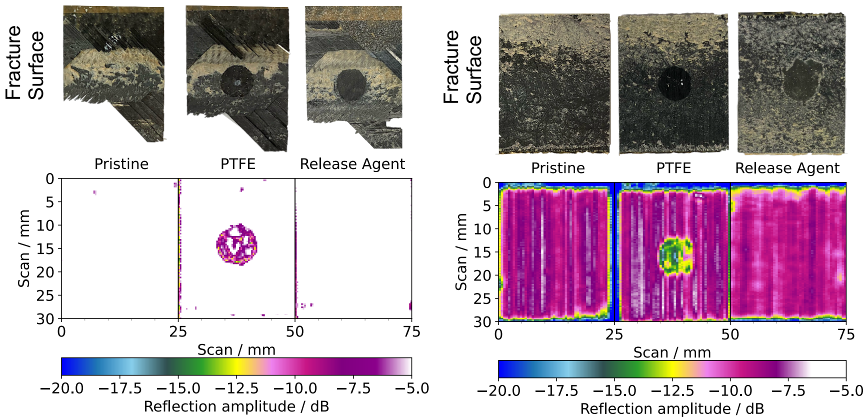

Figure 5.37: Comparison of fracture patterns and ultrasonic C-scans of the bonded CFRP specimens with Sc (left) and SLS (right) configurations after final failure at quasi-static tensile test. From left to right, the figure displays pristine specimens, as well as specimens with PTFE and release agent defects of the respective CFRP adhesive bonds.

Ultrasound images of the fracture patterns from both adhesive configurations reveal that only PTFE films are identifiable in the adhesive area. Release agents are not detectable using ultrasound imaging. The mechanical characterisation of the CFRP bonded joints indicates that in the centre located defects are realistic and do not lead to a reduction in strength, with a defect size of 5 %.

Figure 5.38 shows a detailed illustration of the failure zones within the fracture pattern of a representative Sc specimen. The failure zones are arranged symmetrically. Adhesive failure due to adhesive residues is mainly visible in the area of the 45° layers. Inter-fibre failures due to the stress concentration at the 90° layers and delamination from the 45° layer are recognisable. Minor fibre crack failures are also observed. Above the defect, there is an area with adhesive failure, followed by a mixed fracture of adhesive and cohesive origin. The failure zones of the SLS specimens are also characterised by cohesive and adhesive areas, marked in colour. Adhesive residues indicate cohesive failure in both the specimens with defect insertion and the untreated specimens. It is clearly recognisable that the overlap ends, where stress concentrations are present, are characterised by adhesive failure. This confirms a good manufacturing process with high adhesive strength.

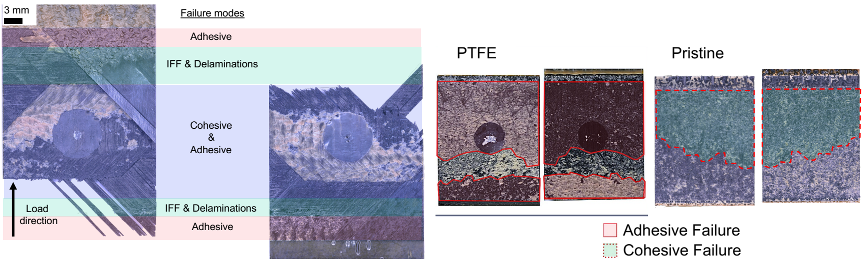

Figure 5.38: Detailed view of the fracture patterns of representative Sc and SLS specimens. Colour-coded areas show the respective dominant failure modes.

The violin plots in Figure 5.39 illustrate the distribution of the modulation index in comparison to AM and PM of the measurements on the CFRP bonded joints. The origin of the bonded part was assigned to the plate numbers by colour. The median MI of the Sc specimens without artificially introduced defects is $4.6 \cdot 10^{-2}$, of the specimens with release agent $6.5 \cdot 10^{-2}$ and of the specimens with PTFE film $4.7 \cdot 10^{-2}$. The median MI of the SLS specimens without artificially introduced defects is $4.3 \cdot 10^{-2}$, of the specimens with release agent $4.2 \cdot 10^{-2}$ and of the specimens with PTFE film $4.5 \cdot 10^{-2}$. The mean values of PM and AM for the respective specimen configurations are observed to demonstrate analogous behaviour. Based on the mean values of the VAM parameters shown and the distributions, it is not possible to differentiate between the defect configuration and a pristine specimen. The interquartile range of all specimen configurations overlaps. This applies to both the Sc and SLS specimens. These observations are consistent with initial VAM measurements by Boll et al. on SLS-GFRP adhesive bonds with adhesive film defects [187], according to which a pure evaluation of the mean value with standard deviation did not result in any significant detection of the defects. According to Chen et al. [305], a classification of defects in conventional tensile specimens made of CFRP could only be made using higher harmonic frequencies and a relative sideband ratio. An increase in amplitude and frequency modulation was observed with a change in stiffness by Dorendorf et al. [249]. As the stiffness is proportional to the shear modulus, it is unlikely that there is a variation in the modulation for different specimens, particularly with different plate origins. The shear modulus of all configurations are in the same size range for both CFRP bonded joints. In addition, the initial VAM measurements show that the manufacturing-related reduction in shear strength cannot be detected using MI, AM or PM.

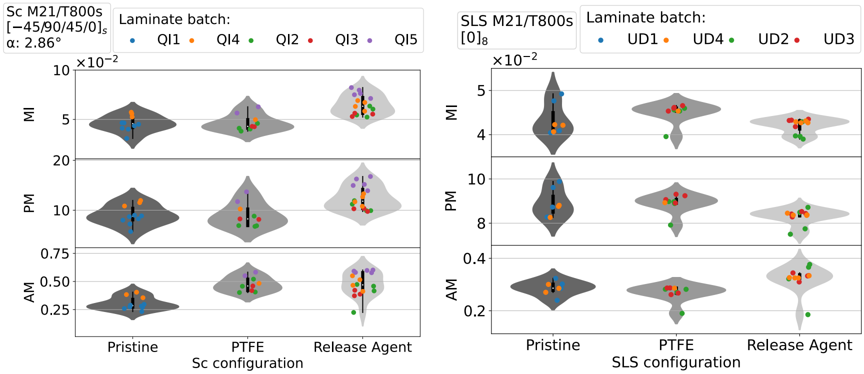

Figure 5.39: Modulation index, amplitude modulation and phase modulation of the Sc (left) and SLS specimens (right) for different defect configurations (PTFE, Release Agent) compared with reference (Pristine) specimens

The initial test results indicate that the mechanical properties, specifically the adhesive shear strength and shear modulus, were not significantly affected by the introduction of defects in the shafted and single overlapping specimens. Although there were deviations in the adhesive shear strength due to the manufacturing process, it is not possible to differentiate between the defect-free specimens and the specimens with defects, particularly due to the high scattering of the results. Compared to adhesive bonds with larger defects [187], a reduction in the adhesive shear strength of the PTFE-contaminated specimens would have been expected. Therefore, it is assumed that the selected defect size of 5% reduces its influence on the static strength. Additionally, the defect cannot be initially detected, as confirmed by the damage indicators MI, AM, and PM in the same size range. The next chapter will examine whether defects affect the mechanical properties under fatigue load and if adhesive film monitoring is feasible.

5.4.2 Fatigue tests

Permittivity Determination

Using Eq. 5.2 to determine a crack length, the relative permittivity of the specimens is required. For this purpose, capacitance measurements were carried out on three Sc specimens with PTFE and release agent as defects and a pristine configuration in which the capacitor area A was varied several times. This results in several data points, which are plotted as shown in Fig. 5.40 is shown. Here, the measured capacitance is shown over the plate area A. A linear regression can now be used to determine the slope of the linear equation and the relative permittivity of the corresponding specimen can then be determined using the following equation:

$$slope = \frac{C}{A} = \frac{\epsilon_0 \cdot \epsilon_r}{d} \tag{5.1}$$

The median relative permittivity of the Sc and SLS specimens are 23.54 and 57.43, respectively, with a factor of 2.4 difference. This is attributed to larger capacitor spacing resulting from the duplication of the joining parts. Neither the capacitance nor the relative permittivity can be distinguished between the two defect configurations.

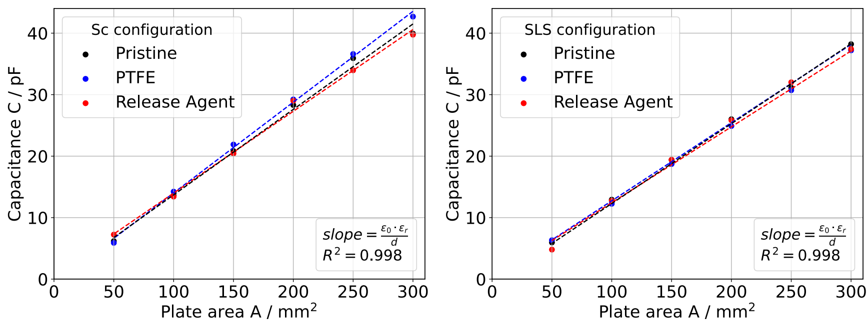

Figure 5.40: Representative plot for the determination of relative permittivity in scarfed joint specimens (left) and single-lap shear specimens (right) including artificial defects

Scarfed joints results

As illustrated in fig. 5.41, the results of VAM measurements during fatigue tests conducted on a Pristine Sc specimen are presented. The modulation indices up to the fourth order and the capacitance change with the recorded longitudinal strain at measuring point 5 are plotted over the load cycles. On the right-hand side, four specific measurement sections of the DIC recordings are shown with the corresponding scale. The geometric symbols are assigned to the corresponding recordings. The damage progression can be divided into three areas. The measured strain is inversely proportional to the change in capacitance. In the initial range of up to approximately $1.1 \cdot 10^{\mathbf{3}}$ cycles, a capacitance change of $-1.1\,\%$ occurs due to localized strain in thickness direction of less than $1\,\%$. The DIC images do not show any macroscopic cracks, only localized strains. The MIs up to the fourth order increase with continuous fatigue, which indicates crack formation. Therefore, the decrease in capacitance can be attributed to the local strain maxima resulting from the stress maxima along the 90° layers or continuously the 45° layers.

Until macroscopic cracks occur at around $4.6 \cdot 10^{\mathbf{3}}$ cycles, which can be seen from the significant increase in DIC strain, the MI increase until 0.36. An exponential increase in local elongation, the drop in capacitance to $-12\,\%$ and the MI to 0.87 is the result until the final failure at around $2.6 \cdot 10^{\mathbf{5}}$ cycles. The cracks propagating at the adhesive film area as can be seen in the DIC image. Characteristic points in the VAM parameters, as previously observed in CFRP laminates under fatigue, are not identifiable in the Sc specimens. The sidebands, modulation indices and amplitude and phase modulation were taken into account. Thus, it is not possible to estimate the life expectancy based on the VAM parameters. However, the exponential increase in the DIC, capacitance and VAM signal proves to be a reliable indicator of imminent structural failure.

The FFT and chirp signals in Fig. 5.42 show that both the number and height of the sidebands increase with continuous fatigue loading and that the frequency range does not shift. This suggests continuous crack growth without the occurrence of large scale delamination.

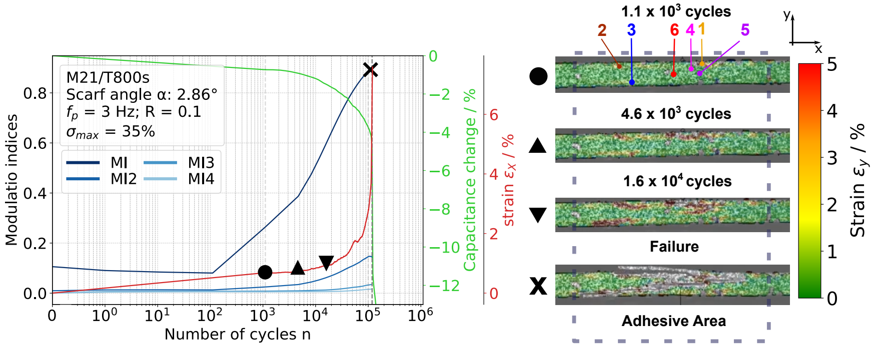

Figure 5.41: Representative results of fatigue tests on Sc CFRP specimens with quasi-isotropic layup. VAM parameter, capacitance change and peel strain of the adhesive bond at the 90° layers based on DIC images are shown. Corresponding DIC images for four specific fatigue steps showing strain in thickness direction.

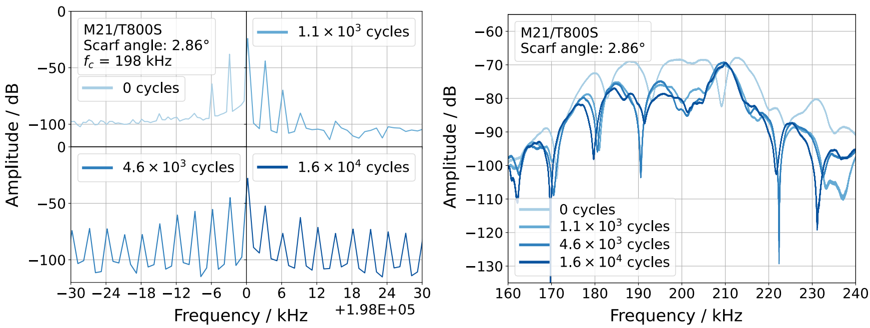

Figure 5.42: FFT signal (left) and chirp signal (right) of CFRP Sc specimens at 3 Hz after initial and continuous fatigue measurements. The areas of the negative and positive sidebands in the FFT signal are shown in the respective quadrants according to the associated fatigue cycles.

Fig. 5.43 displays the fracture pattern of the Sc specimens, including the schematic fracture progression in side view, with the respective joining parts at the top and bottom. The red lines indicate the crack path, while the red areas indicate the corresponding fracture surfaces at the top and bottom. This fracture pattern is representative of all Sc specimens, including those with artificially introduced defects due to the position of damage initiation and is illustrated in the Appendix in G.7. The static tests reveal that inter-fibre fractures in the 90° layers significantly dominate the failure. In the fatigue tests, damage initiation also occurs in this area, followed by crack growth in the adhesive joint. The results are consistent with the studies conducted by Augustin et al. [201] and Harder et al. [185]. Fibre fractures were observed in the 45° layers of the upper joining part, with inter-fibre fractures occurring in the 90° layer. Furthermore, delamination from the neighbouring 90° layer resulted in an exposed area of -45° layers. In addition to the red areas, there are yellow adhesive residues visible on the lower joining part, which are less pronounced in the upper joining part. These observations suggest that the failure was dominated by the adhesive. To the right of this area, the adhesive residue is distributed on the opposite joining parts, indicating a change in the crack front. The upper adherend part displays residues from the lower adherend part, revealing a distinct delamination between the 90° and -45° layers. In the upper right-hand corner of the image, an area of adhesive failure between the upper and lower adherend parts is visible.

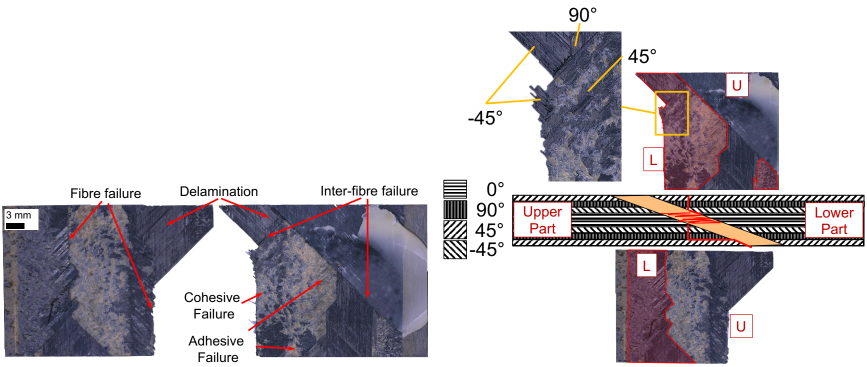

Figure 5.43: Detailed view of the fracture patterns of representative Sc specimens after final failure at fatigue tests with respective dominant failure modes (left). Resulting schematic fracture progression in side view with segmentation of the adherend parts (right).

The results of the tensile-tensile fatigue tests on scarfed joint specimens are shown in Fig.5.44. The diagram on the left represents the S-N curve, where the percentage static strength of the non-defective specimens is plotted versus the number of cycles to failure on a logarithmic scale. The solid lines indicate the calculated failure probability that 50 % of the specimens will fail after this number of cycles at a certain stress level. The scarfed specimens were tested at a total of five different load horizons, which are in 5 % ranges between 65 and 45 % of the static strength of the pristine specimens. Generally, specimens with defects incorporated have lower fatigue strength compared to defect-free specimens. Therefore, the S-N curve for specimens with release agent is shifted towards a lower number of cycles and lower strengths compared to the S-N curve of pristine specimens in the diagram. The trend is particularly noticeable in the specimens with PTFE film. As a result, the corresponding Wöhler curve in the diagram is shifted towards a lower number of cycles and lower strengths compared to the Wöhler curve of the specimens with release agent. PTFE specimens from the 45 % load horizon have similar life expectancies to the pristine specimens of the 55 % load horizon. However, the introduction of defects reduces the fatigue strength, as it increases stress concentration in the defective area. The defects serve as an area for crack initiation, leading to earlier development and propagation of a fatigue crack compared to the defect-free specimens. However, fatigue damage may originate in a different area, and the presence of a defect may lead to premature failure due to a reduction in the effective bonding area. This behaviour occurs because the stress required for fracture is lower than in defect-free specimens, resulting in a shorter service life. The specimens with PTFE film have a shorter service life due to the measurable thickness of the film, which results in a higher stress concentration compared to the specimens with release agent. The first-order MI curve of the three specimen configurations, tested at different load horizons on the right side, indicates that the percentage change in MI is higher at a lower load level tested. For all applied stresses the curves exhibit a coincidence in their respective colour intensities. This trend is consistent for all specimens, regardless of the configuration and confirms a low variance of the VAM results. This accuracy is particularly remarkable given the typically high variance of mechanical results in fatigue tests. The MI change converges towards 100 %, which is not reached by the specimens with a higher load level. The VAM measurement could not record the time of failure due to early failure. As the Sc specimens only fail in the adhesive area without substrate fracture, the area of forced fracture at higher stress levels theoretically should be wider than at lower stress levels, the curves suggest a correlation between fatigue crack growth and the increase in MI.

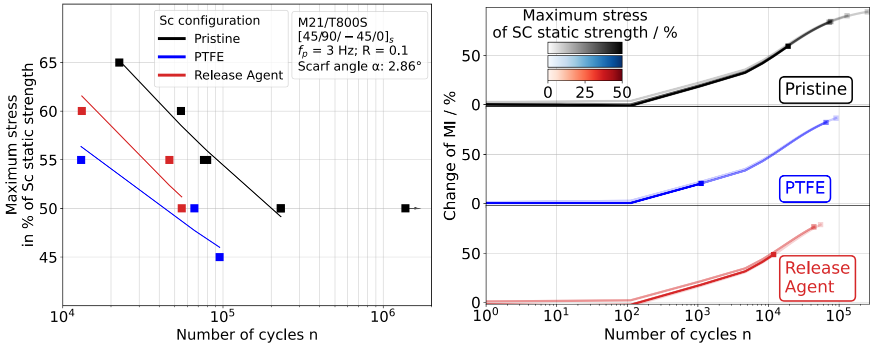

Figure 5.44: S-N curves of the Sc specimens under fatigue results with a load ratio of R=0.1 showing the number of cycles at relative maximum stress of static strength (left) and dependency of relative MI change with varied maximum stress over number of cycles of Sc specimens (right).

Single-lap shear results

Figure 5.45 displays the results of the VAM measurements performed during the fatigue tests on a pristine SLS specimen. The modulation indices up to the fourth order and the capacitance change with the recorded longitudinal strain at measuring point R1 from the DIC recordings are plotted over the load cycles. On the right-hand side, the measurement volumes of the DIC recordings are shown with the corresponding scale for five specific measurement points. The respective recordings are assigned to the geometric symbols. The damage curve for the SLS specimens can be divided into three areas. The change in capacitance is inversely proportional to the measured strain. In the initial range of up to approximately $1.1{\cdot}10^{\mathbf{3}}$ cycles, a capacitance change of $-0.16\,\%$ occurs due to localized elongation of less than $5\,\%$. The peel stresses in this case are five times lower than those in the Sc specimens due to the stress concentration at the joining ends. There is no visible sign of a macroscopic crack in the corresponding DIC image. The MI shows a clear increase to 0 at this number of load cycles, indicating crack initiation. Therefore, the capacity drop can be attributed to the local strain maxima resulting from the stress maxima along the overlap ends. As fatigue progresses, there is a noticeable increase in the measured strain, which correlates with the change in capacitance. Until macroscopic cracks occur at around 4500 cycles, which can be seen from the significant increase in DIC strain, there is a capacitance drop of $0.48\,\%$ and an MI of 0.36. An exponential increase in local elongation to over $35\,\%$, the drop in capacitance to $-12\,\%$ and the MI to 0.77 is the result until the final failure at around 45700 cycles. The cracks propagating from the bond ends have spread over a large part of the bond as can be seen in the DIC image. Characteristic points in the VAM parameters, as previously observed in fatigued CFRP laminates, are also not identifiable in the SLS specimens as in the Sc specimens. The sidebands, modulation indices, as well as amplitude and phase modulation, were considered. This makes it difficult to estimate the service life based on the VAM signal. However, the exponential increases in the DIC, capacitance, and VAM signal prove to be a reliable indicator of approaching structural failure.

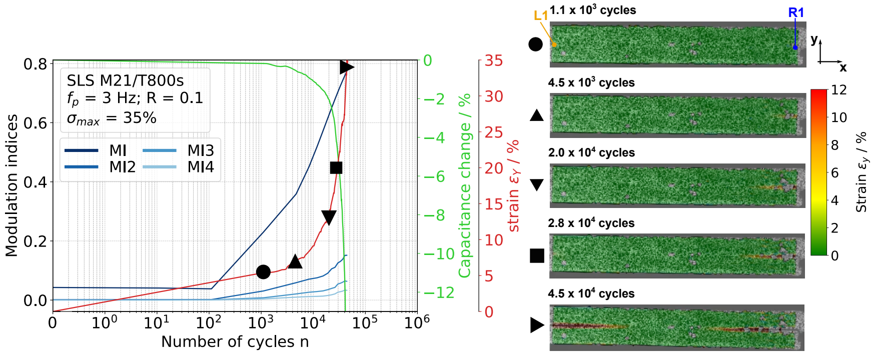

Figure 5.45: Representative results of fatigue tests on SLS CFRP specimens with quasi-isotropic layup. VAM parameter, capacitance change and peel strain of the adhesive bond at the 90° layers based on DIC images are shown. Corresponding DIC images for four specific fatigue steps showing strain in thickness direction.

The fracture behaviour of SLS specimens with defects is similar to the fracture behaviour of specimens without defects, as shown in Figure 5.46. The DIC images of the specimens shortly before final failure and the resulting fracture surface are presented. The stress and strain concentrations are localised at the overlap ends, while small strains are observed between the ends. Stress concentrations are not visible from this camera position if the defect is located in the centre of the overlap bond. However, a symmetrical distribution of stress concentrations is only present in the pristine specimen. This behaviour can be explained by a fracture surface of a specimen provided with release agent in Fig. 5.46 on the right. The presence of defects causes stress concentration, resulting in an asymmetrical stress distribution that also affects the asymmetrical crack. The DIC can only capture the crack growth from the left side, as the entire adhesive length is not visible. The right side is not captured in the DIC images due to the short length of the crack in that area. Furthermore, it should be noted that the crack length does not propagate uniformly across the width of the specimen. Therefore, the crack length depicted in the DIC images only represents a portion of the complete crack.

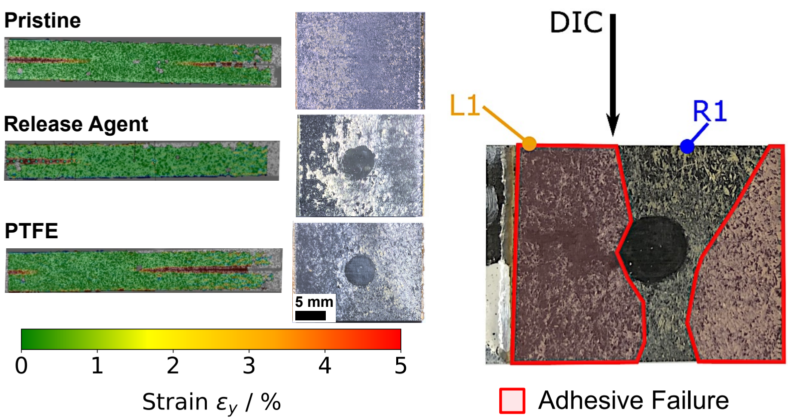

Figure 5.46: Comparison of fracture patterns and DIC images of the SLS bonded CFRP specimen after final failure at fatigue test (left). From top to bottom, the figure displays a pristine specimen and specimens with PTFE and release agent defects. The fracture pattern of the adherend part shown in the DIC images with labels on the sides and points L1 and R1 marked (right).

The FFT and chirp signals of the SLS specimen in Figure 5.47 confirm a continuous crack propagation, which in the case of the SLS specimens originates from the overlap ends. Symmetrical sidebands are formed and the frequency range does not shift. In fact, for both bonded joints, it is evident that life monitoring is possible for the selected frequency range and that the macroscopic cracks with continuous fatigue can be detected. Global delamination, as occurs in QI CFRP laminates, leads to ultimate failure and cannot be compensated by stress redistribution. As a result, no maxima of VAM parameters occur, as the test specimens fail beforehand.

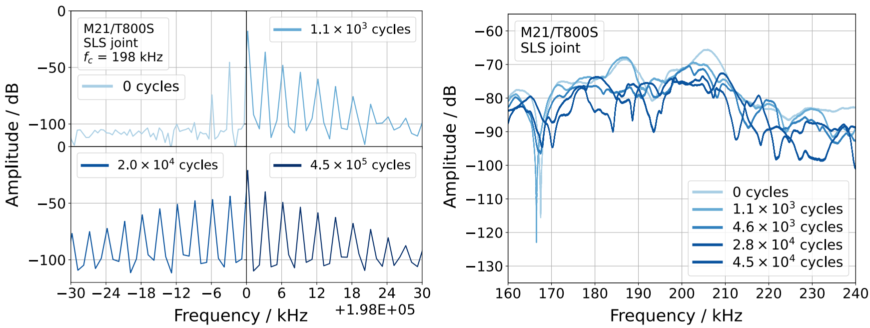

Figure 5.47: FFT signal (left) and chirp signal (right) of CFRP SLS specimens at 3 Hz after initial and continuous fatigue measurements. The areas of the negative and positive sidebands in the FFT signal are shown in the respective quadrants according to the associated fatigue cycles.

The S-N curves of the SLS specimens loaded in tension-tension in Fig. 5.48 confirm the previously observed failure behaviour and stress distribution within the bonded joint. The specimens were tested at different load horizons between 55 % and 30 % of the static strength of the SLS Pristine specimens. No clear trend is recognisable between the different specimen configurations and therefore the service life. The expected service life at a load horizon of 30 % for Pristine specimens is in the range of the PTFE specimen and the specimen with release agent achieved the highest number of load cycles. For the load horizon of 40 %, the life expectancy of the SLS Pristine specimen lies between the life expectancies of the specimens with introduced defects, with the specimen with release agent having the lowest life expectancy. The stress increase due to the artificially introduced defects does not appear to be large enough to change anything at the location of crack initiation and propagation, nor to have a noticeable effect on the residual strength at the time of the forced fracture.

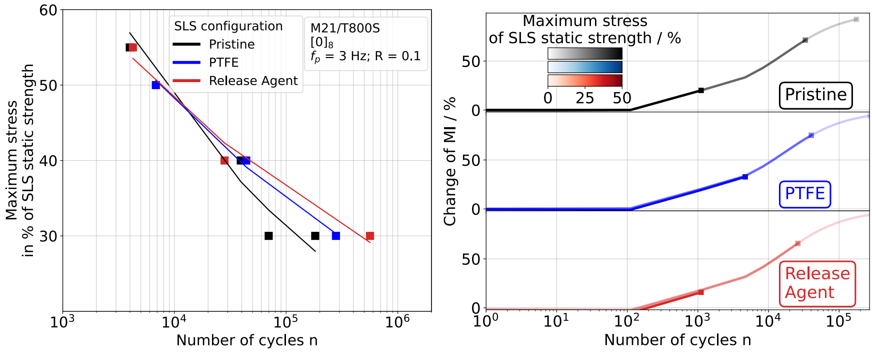

Figure 5.48: S-N curves of the SLS specimens under fatigue results with a load ratio of R=0.1 showing the number of cycles at relative maximum stress of static strength (left) and dependency of relative MI change with varied maximum stress over number of cycles of SLS specimens (right).

Figure 5.48 on the right shows the first-order MI curve for SLS specimens. The results are presented for specimens of three different configurations, which were tested at various load horizons. As can be observed at the Sc specimens, the MI curves exhibit a consistent trend with a minimal variance. A specific MI change can be attributed to a particular load cycle. The number of load cycles achieved and the percentage change in MI increased as the load level at which the specimens were tested decreased. The maximum MI is not measured with higher loads due to the discontinuous VAM measurement, as the specimen fails beforehand.

5.4.3 Analytical modeling of capacitance change in adhesive bonds

The service life of CFRP bonded joints cannot be estimated using characteristic points such as VAM maxima, as is the case with standard CFRP structures. Consequently, capacitance measurements are employed to ascertain the crack length with the objective of establishing a correlation between VAM and crack length. The previous sections investigated the fracture behaviour, elongation of the adhesive film, change in capacitance in the bond section, and modulation under fatigue load. An analytical model was used to develop the relationship between the capacitance change and the VAM damage indicators in Sc and SLS bonds. The model considers the adhesive film region in the thickness direction as an ideal plate capacitor with uniform electric field. The permittivity of the respective specimen configuration was used to characterise the dielectric medium. The distance between the insulated copper tapes on the surface of the specimens remains almost constant for Sc specimens. However, when the SLS specimens are loaded, peeling stresses occur at the end of the overlap length, resulting in an increase in distance. This change in distance is tracked using six measuring points during the DIC measurement. The area of conductor A is determined by the width and length of the copper adhesive tapes (6 x 30 mm). As previously explained in chapter 3.4, elongating the adhesive film in the thickness direction causes a linear decrease in capacitance due to the resulting change in distance of the capacitor. The presence of microscopic and macroscopic cracks can introduce air as an additional dielectric medium. The capacitance can be calculated using Equation 3.1.

$$C = \epsilon_0 \cdot (\epsilon_{air} \cdot a + \epsilon_{CFK}(a_{max} - a))\frac{b}{d} \tag{5.2}$$

$$a = \frac{1}{\epsilon_{air} - \epsilon_r} \cdot \left(\frac{C \cdot d}{b \cdot \epsilon_0} - a_{max} \cdot (\epsilon_r - \epsilon_{PTFE})\right) \tag{5.3}$$

The crack length a is limited by the maximum possible crack length a_{max} which is equal to the overlap length of the adhesive joint. The width of the copper adhesive tape is b. The distance d of the ideal capacitor is affected by the elongation of the adhesive film in the thick seal under fatigue load and is measured using the DIC system. Figure 5.49 illustrates the model development of these considerations for SLS and Sc specimens. The graph demonstrates that the relative capacity decreases linear as the crack length increases for all configurations. As a result of the elongation and crack expansion, the proportion of the relative dielectric constant of air $\epsilon_{air} = 1.0006$ increases and the proportion of the apparent longitudinal relative dielectric constants $\epsilon_{r,CFK} = 57.43$ for SLS specimens and $\epsilon_{r,CFK} = 23.54$ for Sc specimens, previously determined in Section 5.2.1, decreases. The relative dielectric constant is assumed to be $\epsilon_{PTFE} = 2$ [306].

Figure 5.50 shows the crack length and VAM parameters of representative SLS specimens under fatigue, plotted against the number of fatigue cycles. The crack length for the Sc specimens was determined using 9 homogeneously distributed points of strain averaged along the adhesive film in the thickness direction, which significantly influenced the spacing of the resulting plate capacitor. The spacing

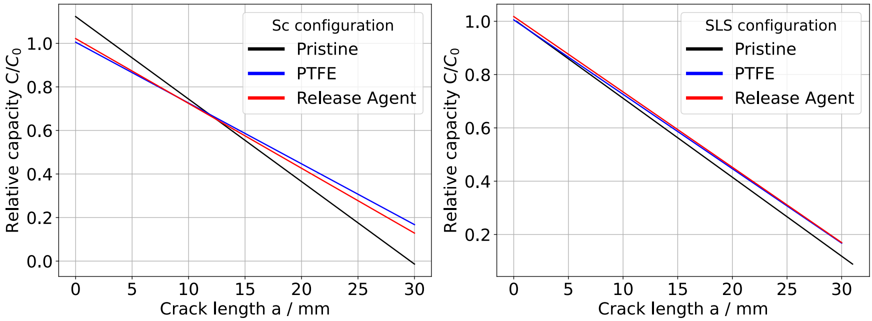

Figure 5.49: Dependency of relative capacity and calculated crack length of Sc (left) and SLS (right) specimens under fatigue load

of the plate capacitor in the SLS specimens was determined by the peel stresses at the overlap ends. The measured crack length due to the decrease in capacitance agreed well with the analytical modelling for all test specimens, both with and without defects. The crack length was measurable throughout the entire test. The crack development caused a measurable increase in the sidebands for all test specimens throughout the test. The analytical model corresponds approximately to the experimental increase over the entire test and can be attributed to the vibro-acoustic behaviour. The crack length analysis demonstrates the potential of localised damage monitoring in CFRP bonded joints and monitoring the development of damage.

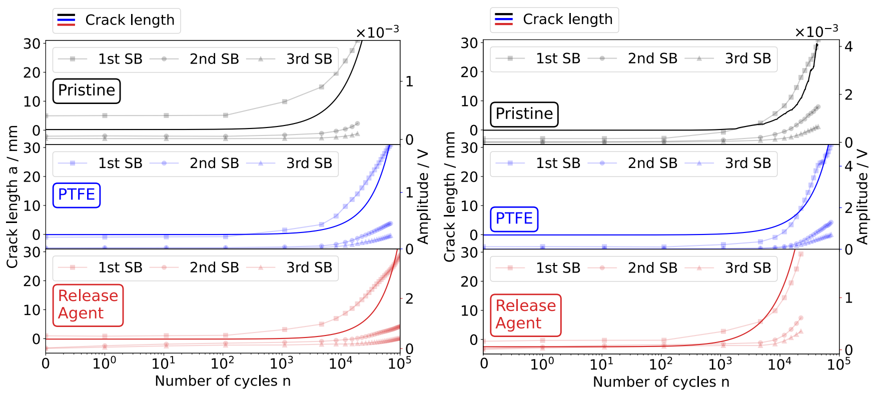

Figure 5.50: Dependency of calculated crack length and first three sidebands of Sc (left) and SLS (right) specimens under fatigue load

Capacitance measurements and measured adhesive film elongation can be used to determine the crack length and damage condition of CFRP adhesive joints. The calculation for the adhesive bonds produced assumes an ideal plate capacitor with a uniform electric field, uniform conductor spacing in the initial state, and rectangular conductor surfaces. These tests are suitable for determining the relative permittivity of bonded joints, confirming agreement between calculated and experimental results. During fatigue loading, the conductor spacing of the capacitor increases in both bonded joints, as confirmed by the elongation of the adhesive film in the thickness direction, resulting in a decrease in measured capacitance. The length of the crack correlates with the measured VAM signal, which justifies the assumptions made regarding the capacitor in the dynamic case. The results also demonstrate that the damage state of the bonded joints can be characterised using several measurement methods. However, the VAM measurement is the most sensitive compared to DIC and capacitance measurement, due to the numerous influencing parameters. Finally, the reliability of adhesive film monitoring using VAM was confirmed through the integration of DIC and capacitance measurement.

6 Summary and Conclusion

New valuable insights into vibro-acoustic modulation measurements as an NDT method in CFRP composites are provided by the results achieved within this thesis, with a special emphasis on sensitivity. The following research hypothesis is confirmed based on the results obtained:

Damage detection and determination of CFRP structures can be ensured through vibro-acoustic in-situ measurements, even retrospectively.

In General, VAM is a dependable technique for detecting damage in CFRP structures with varying geometry and ply thickness, which correlates with different damage behaviours. The investigation of step-wise and fatigue tensile tests revealed that inter-fibre fractures result in an increase in crack size proportional to the sideband amplitudes and a decrease in stiffness. The size and density of cracks have an impact on the VAM signal, with larger cracks causing a higher sideband increase. This observation is consistent with AE measurements. On the other hand, large delaminations result in an exponential decrease in the sidebands, which correlates with the decrease in stiffness. To fully characterise the extent of damage, it is important to consider the time domain of the VAM signal in addition to the factors mentioned above. The presence of inter-fibre fractures causes an increase in the enveloping sinusoidal curve of the low-frequency vibration due to the local increase in strain under constant stress. Conversely, large-scale delamination leads to a gradual separation of the individual layers, resulting in friction and multiple oscillations. This causes a progressive deviation of the sinusoidal envelope curve. Similarly, the propagation of Lamb waves throughout the entire sample thickness is no longer present, resulting in a significant decrease in signal strength.

In the initial undamaged measurements, the stress parameters of the low frequency excitation were varied and the results showed that only the stress amplitude correlated with the change in the damage indicators modulation index (MI), amplitude modulation (AM) and phase modulation (PM). The stress state with varying tensile and compressive components and the mean stress were found to be irrelevant. However, the proportion of AM and PM was found to depend strongly on the stress state and the test setup. For instance, specimens excited solely under tension with a stress ratio (R) of 0.1 to 0.3 exhibit composite-typically a dominant PM component. Conversely, the utilisation of a buckling support under alternating load with a stress ratio of R=-0.1 to -0.5 serves to suppress PM, thus predominates a strong AM component. The versatility of VAM in multiaxial loading is considerable, regardless of the stress state.

When determining the service life of fibre composites, the onset of delamination is an exclusion criterion and provides a useful feature for VAM as an SHM method. By correlating the sideband amplitudes with the relative stiffness and determining the effects of specific damage on the sideband amplitude, critical cycles at certain stress amplitudes can also be identified, and a sideband threshold can be defined shortly before delamination occurs. The occurrence of sideband maxima is directly proportional to the applied stress amplitude. The Palmgren-Miner rule, with an extension of this occurrence to the VAM maxima, can be reliably used for lifetime prediction, regardless of stress, specimen geometry, and configuration. These observations apply to all tested CFRP structures, whether unnotched, notched, or impacted specimens under fatigue loading. The number of cycles between the VAM maxima and final failure increases as the ply thickness increases. It can be observed that thicker layers are more susceptible to delamination. Thinner layers have a longer service life with regard to SHM, but their sensitivity decreases due to smaller crack size and higher crack density.

In CFRP bonded joints, sideband maxima are not present. The increase in VAM damage indicators is proportional to the development of fatigue damage. To record the propagation of fatigue damage, DIC and capacitance measurements were used to determine a specific crack length, which correlates well with the increase in sideband amplitudes. Overall, PM clearly dominates over AM. A service life estimate can be made by modelling the crack length. Additionally, it is important to investigate the suitability of the VAM method for damage monitoring on large-area structures, such as repair bonds. This may require the use of a sensor network in the application. The presented approach for analysing the VAM signal in relation to characteristic points for damage monitoring has partially confirmed the following sub-research hypothesis:

> *The service life of CFRP structures can be estimated based on different damage indicators.*

The amplitudes of sidebands also increase in cases of locally induced delamination and inter-fibre failures, as well as with impact damage. For FAI and CAI structures, the amplitudes are correlated with the extent of damage, which is determined by the impact energy or projected delamination area. Damage caused by impacts can be detected in both the tensile-tensile and the tensile-compression and compression-compression ranges. However, the increase in MI, which measures the sensitivity of VAM, is higher with increasing compressive component of the low-frequency excitation applied. This phenomenon can be attributed to delaminations opening under compression, which was prevented by the presence of a buckling support.

The sensor network of 4 piezoceramic actuators was applied to the larger sample geometry of the CAI samples to generate direct measurement paths outside and along the impact damage. Even this limited measuring size allows localisation of the damage due to the higher sideband amplitude difference.

However, the current measurement setup cannot detect artificially introduced small sized defects on or along adhesive joints. It is not possible to differentiate between defect-free samples and samples contaminated with PTFE and release agent at 5 % defect area, based on all the damage indicators used. Further investigations could explore the systematic variation of the defect area to determine a minimum detectable defect size. The presence, extent and location of the damage can, however, be checked in CFRP structures by including the basic influencing parameters of VAM at different stress states and loading conditions. The delamination area in affected specimens was assessed using VAM, and the fatigue life prediction was modelled. Therefore, the following research hypothesis can be proven for CFRP structures:

> *Vibro-acoustic modulation allows early detection of defects in CFRP structures, providing a wide range of quality control applications for CFRP.*

The comparison between VAM and conventional NDT methods indicates that VAM is generally highly sensitive. VAM and AE measurements correlate well in crack initiation and are equally influenced by crack size. Damage monitoring of FAI samples also demonstrates that VAM is more sensitive than ultrasonic C-scans for thin-ply structures. The increase in sideband amplitudes by VAM allowed for the detection of progressive damage growth at the micrometer level, which could not be detected even with CT scans under the same load and sample condition [300].

Capacitance measurements on CFRP bonded joints were also found to be helpful for modelling the crack length, in addition to the DIC measurements. However, crack initiation caused a significant increase in the MI and sideband amplitudes. This increase was observed in the capacitance measurement as a slight drop, but was not detected in the DIC measurement.

For all tested CFRP configurations, VAM provides the basis for an in-situ SHM method in real-time at low measurement technology costs. The knowledge gained from this work provides the basis for safe and efficient use of CFRP by establishing a direct correlation between varying damage behaviour and different VAM damage indicators. However, the current limitation is the introduction of low-frequency vibration. One approach is available for the simple integration of defined force states [297]. These states are generated statically and then combined as a sinusoidal curve. The results generated in this work can be used to evaluate this approach in fundamentals.

Bibliography

[1] O'brien, TK. "Characterization of Delamination Onset and Growth in a Composite Laminate". In: *Damage in composite materials* (1982), p. 140.

[2] Ogin, S.L., Smith, P.A., and Beaumont, P.W.R. "Matrix cracking and stiffness reduction during the fatigue of a (0/90)s GFRP laminate". In: *Composites Science and Technology* (1985), pp. 23–31. doi: 10.1016/0266-3538(85)90088-0..

[3] Kosmann, N., Karsten, J.M., Schuett, M., Schulte, K., and Fiedler, B. "Determining the effect of voids in GFRP on the damage behaviour under compression loading using acoustic emission". In: *Composites Part B: Engineering* 70 (2015), pp. 184–188. issn: 1359-8368. doi: 10.1016/j.compositesb.2014.11.010..

[4] Tai, NH, Yip, MC, and Lin, JL. "Effects of low-energy impact on the fatigue behavior of carbon/epoxy composites". In: *Composites Science and Technology* 58.1 (1998), pp. 1–8.

[5] Ramkumar, Ramaswamy L. *Effect of low-velocity impact damage on the fatigue behavior of graphite/epoxy laminates.* ASTM International, 1983.

[6] Prichard, J C and Hogg, PJ. "The role of impact damage in post-impact compression testing". In: *Composites* 21.6 (1990), pp. 503–511.

[7] Richardson, M.O.W. and Wisheart, M. J. "Review of low-velocity impact properties of composite materials". In: *Composites Part A: Applied Science and Manufacturing* 27.12 (1996), pp. 1123–1131. issn: 1359835X. doi: 10.1016/1359-835X(96)00074-7.

[8] Sihn, Sangwook, Kim, Ran Y., Kawabe, Kazumasa, and Tsaic, Stephen W. "Experimental studies of thin-ply laminated composites". In: *Composites Science and Technology* 67.6 (2007), pp. 996–1008. doi: 10.1016/j.compscitech.2006.06.008..

[9] Amacher, R., Cugnoni, J., Botsis, J., Sorensen, L., Smith, W., and Dransfeld, C. "Thin ply composites: Experimental characterization and modeling of size-effects". In: *Composites Science and Technology* 101 (2014), pp. 121–132. doi: 10.1016/j.compscitech.2014.06.027.

[10] Arteiro, A., Furtado, C., Catalanotti, G., Linde, P., and Camanho, P. P. "Thin-ply polymer composite materials: A review". In: *Composites Part A: Applied Science and Manufacturing* 132 (2020). doi: 10.1016/j.compscitech.2014.06.027.

[11] Cugnoni, J., Amacher, R., Kohler, S., Brunner, J., Kramer, E., Dransfeld, C., Smith, W., Scobbie, K., Sorensen, L., and Botsis, J. "Towards aerospace grade thin-ply composites: Effect of ply thickness, fibre, matrix and interlayer toughening on strength and damage tolerance". In: *Composites Science and Technology* 168 (2018), pp. 467–477. doi: 10.1016/j.compscitech.2018.08.037.

[12] Wisnom, M. R., Khan, B., and Hallett, S. R. "Size effects in unnotched tensile strength of unidirectional and quasi-isotropic carbon/epoxy composites". In: *Composite Structures* 84 (2008), pp. 21–28. doi: 10.1016/j.compstruct.2007.06.002.

[13] Alves, L. M., Afonso, R. M., and Martins, P. A.F. "Double-sided self-pierce riveting of polymer sheets". In: *Journal of Advanced Joining Processes* 3 (June 2021). issn: 2666-3309. doi: 10.1016/J.JAJP.2021.100051.

[14] Oz, Fatih E., Mehdikhani, Mahoor, Ersoy, Nuri, and Lomov, Stepan V. "In-situ imaging of inter- and intra-laminar damage in open-hole tension tests of carbon fibre-reinforced composites". In: *Composite Structures* 244 (July 2020). issn: 0263-8223. doi: 10.1016/J.COMPSTRUCT.2020.112302.

[15] Ciardiello, R., Greco, L., Miranda, M., Sciullo, F. Di, and Goglio, L. "Experimental investigation on adhesively bonded U-shaped metallic joints using the Arcan test". In: *Journal of Advanced Joining Processes* 1 (Mar. 2020). issn: 2666-3309. doi: 10.1016/J.JAJP.2020.100010.

[16] Goyal, Rakesh and El-zein, Mohamad. "Influence of laser weld shape on mechanical and fatigue behaviour of single lap laser welded joints". In: *Journal of Advanced Joining Processes* 1 (Mar. 2020), p. 100018. issn: 2666-3309. doi: 10.1016/J.JAJP.2020.100018.

[17] Dross, M., Heyser, P., Meschut, G., Hürkamp, A., and Dröder, K. "Fiber response to pin penetration in dry woven fabric using numerical analysis". In: *Journal of Advanced Joining Processes* 5 (June 2022). issn: 2666-3309. doi: 10.1016/J.JAJP.2021.100083.

[18] Haddad, E., Chung, W. S., Katz, O., Helm, J., Olowinsky, A., and Gillner, A. "Laser micro welding with fiber lasers for battery and fuel cell based electromobility". In: *Journal of Advanced Joining Processes* 5 (June 2022). issn: 2666-3309. doi: 10.1016/J.JAJP.2021.100085.

[19] Sinthusiri, Chaiwat and Nassar, Sayed A. "Load distributions in bolted single lap joints under non-central tensile shear loading". In: *Journal of Advanced Joining Processes* 3 (June 2021), p. 100055. issn: 2666-3309. doi: 10.1016/J.JAJP.2021.100055.

[20] de Goeij, W.C., van Tooren, M.J.L., and Beukers, A. "Composite adhesive joints under cyclic loading". In: *Materials & Design* 20.5 (1999), pp. 213–221. issn: 0261-3069. doi: https://doi.org/10.1016/S0261-3069(99)00032-1. url: https://www.sciencedirect.com/science/article/pii/S0261306999000321.

[21] Markatos, DN, Tserpes, KI, Rau, E, Markus, S, Ehrhart, B, and Pantelakis, Sp. "The effects of manufacturing-induced and in-service related bonding quality reduction on the mode-I fracture toughness of composite bonded joints for aeronautical use". In: *Composites Part B: Engineering* 45.1 (2013), pp. 556–564.

[22] Lockard, Colin D. "Anomaly detection in radiographic images of composite materials via crosshatch regression". PhD thesis. Mills College, Jan. 2015.

[23] Kundu, Tribikram. *Nonlinear ultrasonic and Vibro-acoustical techniques for Nondestructive evaluation.* Springer, 2018, pp. 1–759. isbn: 9783319944760. doi: 10.1007/978-3-319-94476-0.

[24] Zagrai, Andrei, Donskoy, Dimitri M., Chudnovsky, Alexander, and Wu, Hudson. "Assessment of material fatigue damage using nonlinear vibro-modulation technique". In: *The Journal of the Acoustical Society of America* 115.5 (2004), p. 2576. doi: 10.1121/1.4784208.

[25] Donskoy, Dimitri M. and Sutin, Alexander M. “Vibro-Acoustic Modulation Nondestructive Evaluation Technique”. In: *Journal of Intelligent Material Systems and Structures* 9.9 (1998), pp. 765–771. doi: 10.1177/1045389X9800900909.

[26] Klepka, Andrzej, Pieczonka, Lukasz, Staszewski, Wieslaw J., and Aymerich, Francesco. “Impact damage detection in laminated composites by non-linear vibro-acoustic wave modulations”. In: *Composites Part B: Engineering* 65 (2014), pp. 99–108. issn: 13598368. doi: 10.1016/j.compositesb.2013.11.003.

[27] Pieczonka, Lukasz, Ukowski, P., Klepka, Andrzej, Staszewski, Wieslaw J., Uhl, Tadeusz, and Aymerich, Francesco. “Impact damage detection in light composite sandwich panels using piezo-based nonlinear vibro-acoustic modulations”. In: *Smart Materials and Structures* 23.10 (2014). issn: 1361665X. doi: 10.1088/0964-1726/23/10/105021.

[28] Aymerich, F. and Staszewski, W. J. “Experimental study of impact-damage detection in composite laminates using a cross-modulation vibro-acoustic technique”. In: *Structural Health Monitoring* 9.6 (2010), pp. 541–553. issn: 14759217. doi: 10.1177/1475921710365433.

[29] Lim, Hyung Jin and Sohn, Hoon. “Online fatigue crack prognosis using nonlinear ultrasonic modulation”. In: *Structural Health Monitoring* 18.5-6 (2017), pp. 1889–1902. doi: 10.1177/1475921719828271.

[30] Donskoy, Dimitri M., Sutin, Alexander M., and Ekimov, Alexander E. “Nonlinear acoustic interaction on contact interfaces and its use for nondestructive testing”. In: *NDT & E International* 34.4 (2001), pp. 231–238. doi: 10.1016/S0963-8695(00)00063-3.

[31] Pieczonka, Lukasz, Klepka, Andrzej, Martowicz, Adam, and Staszewski, Wieslaw J. “Nonlinear vibroacoustic wave modulations for structural damage detection: an overview”. In: *Optical Engineering* 55.1 (2015), p. 011005. issn: 0091-3286. doi: 10.1117/1.oe.55.1.011005.

[32] Willmann, Erik, Boll, Benjamin, Scheel, Moritz, Meissner, Robert Horst, and Fiedler, Bodo. “Health monitoring of CFRP laminates under cyclic loading via vibro-acoustic modulation based measurements”. In: *Composite Structures* 308 (Mar. 2023), p. 116696. issn: 0263-8223. doi: 10.1016/J.COMPSTRUCT.2023.116696.

[33] Willmann, Erik, Boll, Benjamin, Moritz, Scheel, Dräger, Torben, Meissner, Robert Horst, and Fiedler, Bodo. "Vibro-acoustic modulation measurements for a lifetime evaluation of composite materials". In: *Proceedings of the 23rd International Conference on Composite Materials*. 2023.

[34] Willmann, Erik, Boll, Benjamin, Mikaelyan, Gor, Wittich, Hans, Meissner, Robert Horst, and Fiedler, Bodo. "Vibro-acoustic modulation based measurements in CFRP laminates for damage detection in Open-Hole structures". In: *Composites Communications* 42 (2023), p. 101659.

[35] Schürmann, Helmut et al. *Konstruieren mit faser-kunststoff-verbunden*. Vol. 2. Springer, 2005.

[36] Daniel, Isaac M, Ishai, Ori, Daniel, Issac M, and Daniel, Ishai. *Engineering mechanics of composite materials*. Vol. 1994. Oxford university press New York, 2006.

[37] Fiedler, Bodo and Karl, Schulte. *Structure and Properties of Composite Materials*. Jan. 2005. isbn: ISBN 3-9300400-53-7.

[38] Drummer, Jonas, Gibhardt, Dennis, Körbelin, Johann, and Fiedler, Bodo. "General influence of the environmental temperature on the matrix strength under tensile and compressive loading-A comprehensive study on high performance matrices". In: *Composites Science and Technology* 230 (2022).

[39] Gibhardt, Dennis, Buggisch, Christina, Meyer, Devin, and Fiedler, Bodo. "Hygrothermal aging history of amine-epoxy resins: Effects on thermo-mechanical properties". In: *Frontiers in Materials* 9 (2022).

[40] Flaggs, D. L. and Kural, M. H. "Experimental Determination of the In Situ Transverse Lamina Strength in Graphite/Epoxy Laminates". In: *Journal of Composite Materials* 16.2 (1982), pp. 103–116. issn: 0021-9983. doi: 10.1177/002199838201600203.

[41] Dvorak, G. J. and Laws, N. "Analysis of Progressive Matrix Cracking In Composite Laminates II. First Ply Failure". In: *Journal of Composite Materials* 21.4 (1987), pp. 309–329. issn: 0021-9983. doi: 10.1177/002199838702100402.

[42] Camanho, P. P., Bessa, M. A., Catalanotti, G., Vogler, M., and Rolfes, R. "Modeling the inelastic deformation and fracture of polymer composites – Part II: Smeared crack model". In: *Mechanics of Materials* 59 (2013), pp. 36–49. issn: 01676636. doi: 10.1016/j.mechmat.2012.12.001.

[43] Adolfsson, E. and Gudmundson, P. "Matrix crack initiation and progression in compositelaminatessubjected to bending and extension". In: *International Journal of Solids and Structures* 36.21 (1999), pp. 3131–3169. issn: 00207683. doi: 10.1016/S0020-7683(98)00142-5.

[44] Arteiro, A., Catalanotti, G., Melro, A. R., Linde, P., and Camanho, P. P. "Micro-mechanical analysis of the in situ effect in polymer composite laminates". In: *Composite Structures* 116 (2014), pp. 827–840. issn: 02638223. doi: 10.1016/j.compstruct.2014.06.014.

[45] Puck, A. "Festigkeitsanalyse von Faser-Matrix-Laminaten, Modelle fuÈr die Praxis". In: *Munchen, Wien: Hanser* (1996).

[46] Knops, Martin. *Analysis of failure in fiber polymer laminates: the theory of Alfred Puck*. Springer Science & Business Media, 2008.

[47] Fiedler, Bodo. *Hochleistungs-Faserverbundwerkstoffe mit Duroplastmatrix*. TuTech Innovation GmbH, 2009.

[48] Fiedler, Bodo, Hojo, Mea, Ochiai, Shojiro, Schulte, Karl, and Ochi, M. "Finite-element modeling of initial matrix failure in CFRP under static transverse tensile load". In: *Composites science and technology* 61.1 (2001), pp. 95–105.

[49] Trappe, Volker and Harbich, K-W. "Intralaminar fatigue behaviour of carbon fibre reinforced plastics". In: *International journal of fatigue* 28.10 (2006), pp. 1187–1196.

[50] Fiedler, Bodo and Karl, Schulte. *Structure and Properties of Composite Materials*. Jan. 2005. isbn: ISBN 3-9300400-53-7.

[51] Gagel, Andreas, Lange, Dirk, and Schulte, Karl. "On the relation between crack densities, stiffness degradation, and surface temperature distribution of tensile fatigue loaded glass-fibre non-crimp-fabric reinforced epoxy". In: *Composites Part A: Applied Science and Manufacturing* 37.2 (2006). CompTest 2004, pp. 222–228. issn: 1359-835X. doi: https://doi.org/10.1016/j.compositesa.2005.03.028. url: https://www.sciencedirect.com/science/article/pii/S1359835X05002502.

[52] Rheinfurth, Martin, Kosmann, Nils, Sauer, Dorothee, Busse, Gerd, and Schulte, Karl. “Lamb waves for non-contact fatigue state evaluation of composites under various mechanical loading conditions”. In: *Composites Part A: Applied Science and Manufacturing* 43.8 (2012), pp. 1203–1211. doi: `10.1016/j.compositesa.2012.03.021`.

[53] Ehrenstein, Gottfried Wilhelm. *Faserverbund-Kunststoffe: Werkstoffe-Verarbeitung-Eigenschaften*. Carl Hanser Verlag GmbH Co KG, 2018.

[54] Chan, WS and Wang, ASD. “Effects of a 90° ply on matrix cracks and edge delamination in composite laminates”. In: *Composites science and technology* 38.2 (1990), pp. 143–157.

[55] Krieger, Raymond B. “An Adhesive Interleaf to Reduce Stress Concentrations Between Plys of Structural Composites”. In: *Adhesion 12* (1988), pp. 159–165.

[56] Pagano, NJ and Lackman, LM. “Prevention of delamination of composite laminates”. In: *AIAA Journal* 13.3 (1975), pp. 399–401.

[57] CHAN, W and OCHOA, O. “Suppression of edge delamination in composite laminates by terminating a critical ply near the edges”. In: *29th Structures, Structural Dynamics and Materials Conference*. 1988, p. 2257.

[58] LEE, EDWARD and CHAN, WEN. “Delamination arrestment by discretizing the critical ply in a laminate”. In: *30th Structures, Structural Dynamics and Materials Conference*. 1989, p. 1403.

[59] Mignery, LA, Sun, CT, and Tan, TM. *The use of stitching to suppress delamination in laminated composites*. ASTM International, 1985.

[60] Howard, WE, Gossard, T, and Jones, RM. “Composite laminate free-edge reinforcement with U-shaped caps”. In: *Part I: stress analysis’ A1AA J* 27 (1989), pp. 611–623.

[61] Chuaqui, TRC, Sebastian, E, Sahadevan, V, Rhead, AT, and Butler, R. “Edge treatment of short beam shear tests for improved assessment of structural strength”. In: *Composites Part A: Applied Science and Manufacturing* 137 (2020), p. 105991.

[62] Schultheisz, Carl R and Waas, Anthony M. “Compressive failure of composites, part I: testing and micromechanical theories”. In: *Progress in Aerospace Sciences* 32.1 (1996), pp. 1–42.

[63] Budiansky, B, Fleck, NA, and Amazigo, JC. "On kink-band propagation in fiber composites". In: *Journal of the Mechanics and Physics of Solids* 46.9 (1998), pp. 1637–1653.

[64] Nunna, Srinivas, Ravindran, Anil R, Mroszczok, Jens, Creighton, Claudia, and Varley, Russell J. "A review of the structural factors which control compression in carbon fibres and their composites". In: *Composite Structures* 303 (2023).

[65] Oya, Naoyuki and Johnson, David J. "Longitudinal compressive behaviour and microstructure of PAN-based carbon fibres". In: *Carbon* 39.5 (2001), pp. 635–645. issn: 0008-6223. doi: https://doi.org/10.1016/S0008-6223(00)00147-0. url: https://www.sciencedirect.com/science/article/pii/S0008622300001470.

[66] Chen, Ke, Jia, Mingyin, Sun, Hua, and Xue, Ping. "Thermoplastic reaction injection pultrusion for continuous glass fiber-reinforced polyamide-6 composites". In: *Materials* 12.3 (2019), p. 463.

[67] Dransfield, Kimberley, Baillie, Caroline, and Mai, Yiu-Wing. "Improving the delamination resistance of CFRP by stitching—a review". In: *Composites Science and Technology* 50.3 (1994), pp. 305–317.

[68] Creighton, C.J, Sutcliffe, M.P.F, and Clyne, T.W. "A multiple field image analysis procedure for characterisation of fibre alignment in composites". In: *Composites Part A: Applied Science and Manufacturing* 32.2 (2001), pp. 221–229. issn: 1359-835X. doi: https://doi.org/10.1016/S1359-835X(00)00115-9. url: https://www.sciencedirect.com/science/article/pii/S1359835X00001159.

[69] Verghese, K. N., Broyles, N. S., Lesko, J. J., Davis, R. M., and Riffle, J. S. "Pultruded Carbon Fiber/Vinyl Ester Composites Processed with Different Fiber Sizing Agents. Part II: Enviro-Mechanical Durability". In: *Journal of Materials in Civil Engineering* 17.3 (2005), pp. 334–342. doi: 10.1061/(ASCE)0899-1561(2005)17:3(334). eprint: https://ascelibrary.org/doi/pdf/10.1061/%28ASCE%290899-1561%282005%2917%3A3%28334%29. url: https://ascelibrary.org/doi/abs/10.1061/%28ASCE%290899-1561%282005%2917%3A3%28334%29.

[70] Thomsen, Ole Thybo and Kratmann, K.K. "Experimental Characterisation of Parameters Controlling the Compressive Failure of Pultruded Unidirectional Carbon Fibre Composites". In: Applied Mechanics and

Materials 24 (Aug. 2010), pp. 15–22. DOI: 10.4028/www.scientific.net/AMM.24-25.15.

[71] ISA, M.D., FEIH, S., and MOURITZ, A.P. "Compression fatigue properties of z-pinned quasi-isotropic carbon/epoxy laminate with barely visible impact damage". In: *Composite Structures* 93.9 (2011), pp. 2269–2276. ISSN: 0263-8223. DOI: https://doi.org/10.1016/j.compstruct.2011.03.015. URL: https://www.sciencedirect.com/science/article/pii/S0263822311000997.

[72] LIEBIG, W.V., LEOPOLD, C., and SCHULTE, K. "Photoelastic study of stresses in the vicinity of a unique void in a fibre-reinforced model composite under compression". In: *Composites Science and Technology* 84 (2013), pp. 72–77. ISSN: 0266-3538. DOI: https://doi.org/10.1016/j.compscitech.2013.04.011. URL: https://www.sciencedirect.com/science/article/pii/S026635381300167X.

[73] LIEBIG, Wilfried V., SCHULTE, Karl, and FIEDLER, Bodo. "Hierarchical analysis of the degradation of fibre-reinforced polymers under the presence of void imperfections". In: *Philosophical transactions of the Royal Society of London / A* 374.2071 (2016), p. 20150279. ISSN: 1364-503X, 1471-2962. DOI: 10.1098/rsta.2015.0279.

[74] SHAMS, Seyedmohammad S and ELHAJJAR, Rani F. "Investigation into the effects of fiber waviness in standard notched composite specimens". In: *CEAS Aeronautical Journal* 6 (2015), pp. 541–555.

[75] DRUMMER, Jonas, TAFESH, Felwa, and FIEDLER, Bodo. "Effect of fiber misalignment and environmental temperature on the compressive behavior of fiber composites". In: *Polymers* 15.13 (2023), p. 2833.

[76] LIU, Dahsin and MALVERN, Lawrence E. "Matrix cracking in impacted glass/epoxy plates". In: *Journal of Composite Materials* 21.7 (1987), pp. 594–609.

[77] DAVIES, Glyn AO, ZHANG, Xiang, ZHOU, Gang, and WATSON, S. "Numerical modelling of impact damage". In: *Composites* 25.5 (1994), pp. 342–350.

[78] CANTWELL, Wesley J and MORTON, John. "The impact resistance of composite materials—a review". In: *composites* 22.5 (1991), pp. 347–362.

[79] ABRATE, Serge. *Impact engineering of composite structures*. Vol. 526. Springer Science & Business Media, 2011.

[80] KHAN, Sanan H and SHARMA, Ankush P. “Influence of metal/composite interface on the damage behavior and energy absorption mechanisms of FMLs against projectile impact”. In: *Defence Technology* 18.3 (2022), pp. 441–456.

[81] DONALDSON, Steven L and MIRACLE, DB. “ASM handbook composites”. In: *ASM International* (2001).

[82] FINN, ScottR. *Composite plates impact damage: an atlas.* Routledge, 2017.

[83] GREEN, B. G., WISNOM, M. R., and HALLETT, S. R. “An experimental investigation into the tensile strength scaling of notched composites”. In: *Composites Part A: Applied Science and Manufacturing* 38.3 (Mar. 2007), pp. 867–878. ISSN: 1359-835X. DOI: 10.1016/J.COMPOSITESA.2006.07.008.

[84] AWERBUCH, J and MADHUKAR, MS. “Notched Strength of Composite Laminates: Predictions and Experiments—A Review”. In: *Journal of Reinforced Plastics and Composites* 4 (1985), pp. 3–159. DOI: 10.1177/073168448500400102.

[85] CHANG, K-Y, LLU, S, and CHANG, F-K. “Damage Tolerance of Laminated Composites Containing an Open Hole and Subjected to Tensile Loadings”. In: *Journal of Composite Materials* 25.3 (1991), pp. 274–301. DOI: 10.1177/002199839102500303.

[86] NIXON-PEARSON, O. J., HALLETT, S. R., WITHERS, P. J., and ROUSE, J. “Damage development in open-hole composite specimens in fatigue. Part 1: Experimental investigation”. In: *Composite Structures* 106 (Dec. 2013), pp. 882–889. ISSN: 0263-8223. DOI: 10.1016/J.COMPSTRUCT.2013.05.033.

[87] GREEN, B. G., WISNOM, M. R., and HALLETT, S. R. “An experimental investigation into the tensile strength scaling of notched composites”. In: *Composites Part A: Applied Science and Manufacturing* 38.3 (2007), pp. 867–878. ISSN: 1359835X. DOI: 10.1016/j.compositesa.2006.07.008.

[88] WISNOM, M. R. and HALLETT, S. R. “The role of delamination in strength, failure mechanism and hole size effect in open hole tensile tests on quasi-isotropic laminates”. In: *Composites Part A: Applied Science and Manufacturing* 40.4 (2009), pp. 335–342. ISSN: 1359835X. DOI: 10.1016/j.compositesa.2008.12.013.

[89] Wisnom, MR, Hallett, SR, and Soutis, C. “Scaling effects in notched composites”. In: *Journal of composite materials* 44.2 (2010), pp. 195–210.

[90] Nixon-Pearson, O. J. and Hallett, S. R. “An investigation into the damage development and residual strengths of open-hole specimens in fatigue”. In: *Composites Part A: Applied Science and Manufacturing* 69 (Feb. 2015), pp. 266–278. issn: 1359-835X. doi: 10.1016/J.COMPOSITESA.2014.11.013.

[91] Arteiro, A., Catalanotti, G., Xavier, J., Linde, P., and Camanho, P. P. “Effect of tow thickness on the structural response of aerospace-grade spread-tow fabrics”. In: *Composite Structures* 179 (2017), pp. 208–223. issn: 02638223. doi: 10.1016/j.compstruct.2017.06.047.

[92] Kawabe, Kazumasa, Tomoda, Shegeru, and Matsuo, Tatsuki. “A pneumatic process for spreading reinforcing fiber tow”. In: *Evolving Technologies for the Competitive Edge.* 42 (1997), pp. 65–76.

[93] Kötter, B., Karsten, J., Körbelin, J., and Fiedler, B. “CFRP Thin-Ply Fibre Metal Laminates: Influences of Ply Thickness and Metal Layers on Open Hole Tension and Compression Properties”. In: *Materials (Basel, Switzerland)* 13.4 (2020). issn: 1996-1944. doi: 10.3390/ma13040910.

[94] Cugnoni, J., Amacher, R., Kohler, S., Brunner, J., Kramer, E., Dransfeld, C., Smith, W., Scobbie, K., Sorensen, L., and Botsis, J. “Towards aerospace grade thin-ply composites: Effect of ply thickness, fibre, matrix and interlayer toughening on strength and damage tolerance”. In: *Composites Science and Technology* 168 (2018), pp. 467–477. issn: 02663538. doi: 10.1016/j.compscitech.2018.08.037.

[95] Schmutzler, Henrik Björn Hans. *Damage Accumulation Monitoring of Impact Damage in Carbon Fibre Reinforced Polymers by Means of Active Thermography.* TuTech-Verlag, 2015.

[96] Brod, M, Dean, A, Scheffler, S, Gerendt, C, and Rolfes, R. “Numerical modeling and experimental validation of fatigue damage in Cross-Ply CFRP composites under inhomogeneous stress states”. In: *Composites Part B: Engineering* 200 (2020), p. 108050.

[97] Quaresimin, Marino and Ricotta, Mauro. “Fatigue behaviour and damage evolution of single lap bonded joints in composite material”. In: *Composites Science and Technology* 66.2 (2006), pp. 176–187.

[98] May, Michael and Hallett, Stephen R. “An advanced model for initiation and propagation of damage under fatigue loading–part I: Model formulation”. In: *Composite structures* 93.9 (2011), pp. 2340–2349.

[99] May, Michael and Hallett, Stephen R. “Damage initiation in polymer matrix composites under high-cycle fatigue loading–A question of definition or a material property?” In: *International Journal of Fatigue* 87 (2016), pp. 59–62.

[100] Stinchcomb, Wayne W and Bakis, Charles E. “Fatigue behavior of composite laminates”. In: *Composite materials series*. Vol. 4. Elsevier, 1991, pp. 105–180.

[101] Paris, Paul and Erdogan, Fazil. “A critical analysis of crack propagation laws”. In: (1963).

[102] Corten, Herbert Theodore. *Composite Materials: Testing and Design: a Conference*. Vol. 497. ASTM International, 1972.

[103] Kaminski, M, Maire, J, Laurin, F, Rakotoarisoa, C, and Hemon, H. *Méthodologies de prévision de durée de vie des composites.*

[104] Chawla, Krishan K. *Composite materials: science and engineering*. Springer Science & Business Media, 2012.

[105] Rotem, Assa and Nelson, HG. “Failure of a laminated composite under tension—Compression fatigue loading”. In: *Composites Science and technology* 36.1 (1989), pp. 45–62.

[106] Schulte, K. “Compressive static and fatigue loading of continuous fiber-reinforced composites”. In: *ASTM SPECIAL TECHNICAL PUBLICATION* 1185 (1994), pp. 278–278.

[107] Gamstedt, EK and Sjögren, BA. “Micromechanisms in tension-compression fatigue of composite laminates containing transverse plies”. In: *Composites Science and Technology* 59.2 (1999), pp. 167–178.

[108] Beheshty, MH, Harris, B, and Adam, T. “An empirical fatigue-life model for high-performance fibre composites with and without impact damage”. In: *Composites Part A: Applied Science and Manufacturing* 30.8 (1999), pp. 971–987.

[109] Melin, LG, Schön, Joakim, and Nyman, Tonny. “Fatigue testing and buckling characteristics of impacted composite specimens”. In: *International journal of fatigue* 24.2-4 (2002), pp. 263–272.

[110] UDA, Nobuhide, ONO, Kousei, and KUNOO, Kazuo. "Compression fatigue failure of CFRP laminates with impact damage". In: *Composites Science and Technology* 69.14 (2009), pp. 2308–2314.

[111] ATTIA, O, KINLOCH, AJ, and MATTHEWS, FL. "The prediction of fatigue damage growth in impact-damaged composite skin/stringer structures. Part I: theoretical modelling studies". In: *Composites science and technology* 63.10 (2003), pp. 1463–1472.

[112] GARNIER, Christian, PASTOR, Marie-Laetitia, LORRAIN, Bernard, and PANTALÉ, Olivier. "Fatigue behavior of impacted composite structures". In: *Composite Structures* 100 (2013), pp. 443–450.

[113] TAI, NH, MA, CCM, LIN, JM, and WU, GY. "Effects of thickness on the fatigue-behavior of quasi-isotropic carbon/epoxy composites before and after low energy impacts". In: *Composites Science and Technology* 59.11 (1999), pp. 1753–1762.

[114] SYMONS, Digby D and DAVIS, Graham. "Fatigue testing of impact-damaged T300/914 carbon-fibre-reinforced plastic". In: *Composites science and technology* 60.3 (2000), pp. 379–389.

[115] ROSENFELD, MS and GAUSE, LW. "Compression fatigue behaviour of graphite/epoxy in the presence of stress raisers". In: *Fatigue of fibrous composite materials* (1981), pp. 174–196.

[116] MITROVIC, Milan, HAHN, H Thomas, CARMAN, Greg P, and SHYPRYKEVICH, Peter. "Effect of loading parameters on the fatigue behavior of impact damaged composite laminates". In: *Composites Science and Technology* 59.14 (1999), pp. 2059–2078.

[117] PALMGREN, A., RULEY, B., PALMGREN, G., and SKF INDUSTRIES, inc. *Ball and Roller Bearing Engineering*. SKF Industries, 1945. URL: `https://books.google.de/books?id=sdtSAAAAMAAJ`.

[118] MINER, Milton A. *Cumulative Damage in Fatigue*. Vol. 12. J. Appl. Mech., 1945, A159–A164. DOI: `10.1115/1.4009458`. URL: `https://books.google.de/books?id=sdtSAAAAMAAJ`.

[119] WISNOM, M. R. "Size effects in the testing of fibre-composite materials". In: *Composites Science and Technology* 59.13 (1999), pp. 1937–1957. ISSN: 02663538. DOI: `10.1016/S0266-3538(99)00053-6`.

[120] Sutherland, LS, Shenoi, RA, and Lewis, SM. “Size and scale effects in composites: I. Literature review”. In: *Composites Science and Technology* 59.2 (1999), pp. 209–220.

[121] Arteiro, A, Furtado, C, Catalanotti, G, Linde, P, and Camanho, PP. “Thin-ply polymer composite materials: A review”. In: *Composites Part A: Applied Science and Manufacturing* 132 (2020), p. 105777.

[122] Kötter, Benedikt, Karsten, Julian, Körbelin, Johann, and Fiedler, Bodo. “CFRP thin-ply fibre metal laminates: Influences of ply thickness and metal layers on open hole tension and compression properties”. In: *Materials* 13.4 (2020), p. 910.

[123] Kötter, B., Yamada, K., Körbelin, J., Kawabe, K., Nishikawa, M., Hojo, M., and Fiedler, B. “Steel foil reinforcement for high performance bearing strength in Thin–Ply composites”. In: *Composites Part C: Open Access* 4 (2021), p. 100085. issn: 26666820. doi: 10.1016/j.jcomc.2020.100085.

[124] Yokozeki, Tomohiro, Aoki, Yuichiro, and Ogasawara, Toshio. “Experimental characterization of strength and damage resistance properties of thin-ply carbon fiber/toughened epoxy laminates”. In: *Composite Structures* 82.3 (Feb. 2008), pp. 382–389. issn: 0263-8223. doi: 10.1016/J.COMPSTRUCT.2007.01.015.

[125] Sebaey, TA, Costa, J, Maimí, P, Batista, Y, Blanco, N, and Mayugo, JA. “Measurement of the in situ transverse tensile strength of composite plies by means of the real time monitoring of microcracking”. In: *Composites Part B: Engineering* 65 (2014), pp. 40–46.

[126] Dvorak, George J and Laws, Norman. “Analysis of progressive matrix cracking in composite laminates II. First ply failure”. In: *Journal of composite materials* 21.4 (1987), pp. 309–329.

[127] Arteiro, A, Catalanotti, G, Xavier, J, and Camanho, PP. “Notched response of non-crimp fabric thin-ply laminates: Analysis methods”. In: *Composites Science and Technology* 88 (2013), pp. 165–171.

[128] Laffan, MJ, Pinho, ST, Robinson, P, and Iannucci, L. “Measurement of the in situ ply fracture toughness associated with mode I fibre tensile failure in FRP. Part II: Size and lay-up effects”. In: *Composites Science and Technology* 70.4 (2010), pp. 614–621.

[129] Parvizi, A. "Constrained cracking in glass fibre reinforced epoxy cross-ply laminates". In: *Composites* 9.4 (1978), p. 286. issn: 00104361. doi: 10.1016/0010-4361(78)90215-X.

[130] Catalanotti, G. "Prediction of in situ strengths in composites: Some considerations". In: *Composite Structures* 207 (2019), pp. 889–893.

[131] Yokozeki, T., Aoki, Y., and Ogasawara, T. "Experimental characterization of strength and damage resistance properties of thin-ply carbon fiber/toughened epoxy laminates". In: *Composite Structures* 82.3 (2008), pp. 382–389. issn: 02638223. doi: 10.1016/j.compstruct.2007.01.015.

[132] Wu, Souheng. *Polymer interface and adhesion*. Routledge, 2017.

[133] Habenicht, Gerd. *Kleben: Grundlagen, Technologien, Anwendungen*. 6., aktualisierte Aufl. VDI-Buch. Berlin and Heidelberg: Springer, 2009. isbn: 9783540852643.

[134] Kaliske, G. *Zu Problemen der Oberflächenbehandlung metallischer Fügeteile in der Klebtechnik unter besonderer Berücksichtigung der mechanischen Vorbehandlung*. Plaste und Kautsch. 1971, pp. 446–452.

[135] Schweizer, Markus, Meinhard, Dieter, Ruck, Simon, Riegel, Harald, and Knoblauch, Volker. "Adhesive bonding of CFRP: a comparison of different surface pre-treatment strategies and their effect on the bonding shear strength". In: *Journal of Adhesion Science and Technology* 31.23 (2017), pp. 2581–2591.

[136] Fischer, F, Kreling, S, Jäschke, P, Frauenhofer, M, Kracht, D, and Dilger, K. "Laser surface pre-treatment of CFRP for adhesive bonding in consideration of the absorption behaviour". In: *The Journal of Adhesion* 88.4-6 (2012), pp. 350–363.

[137] Holtmannspötter, Jens, Czarnecki, JV, Feucht, Florian, Wetzel, Michael, Gudladt, H-J, Hofmann, Timo, Meyer, JC, and Niedernhuber, Michal. "On the fabrication and automation of reliable bonded composite repairs". In: *The Journal of Adhesion* 91.1-2 (2015), pp. 39–70.

[138] Encinas, N, Oakley, BR, Belcher, MA, Blohowiak, KY, Dillingham, RG, Abenojar, J, and Martínez, MA. "Surface modification of aircraft used composites for adhesive bonding". In: *International Journal of Adhesion and Adhesives* 50 (2014), pp. 157–163.

[139] Botana-Galvín, Marta, Blanco, Ginesa, González-Rovira, Leandro, Rodríguez, Miguel A, and Botana, Francisco J. "Adhesive behaviour of carbon fibre reinforced plastic panels manufactured using woven and unidirectional tape after ultraviolet laser surface treatment". In: *Journal of Composite Materials* 52.7 (2018), pp. 853–865.

[140] Boerio, FJ, Roby, B, Dillingham, RG, Bossi, RH, and Crane, RL. "Effect of grit-blasting on the surface energy of graphite/epoxy composites". In: *The Journal of Adhesion* 82.1 (2006), pp. 19–37.

[141] Zaldivar, RJ, Nokes, J, Steckel, GL, Kim, HI, and Morgan, BA. "The effect of atmospheric plasma treatment on the chemistry, morphology and resultant bonding behavior of a pan-based carbon fiber-reinforced epoxy composite". In: *Journal of composite materials* 44.2 (2010), pp. 137–156.

[142] Chin, Joannie W and Wightman, James P. "Surface characterization and adhesive bonding of toughened bismaleimide composites". In: *Composites Part A: Applied Science and Manufacturing* 27.6 (1996), pp. 419–428.

[143] Committee., AMS CACRC Commercial Aircraft Composite Repair. "Masking and Cleaning of Epoxy and Polyester Matrix Thermosetting Composite Materials". In: *SAE International* (2020). doi: 10.4271/ARP4916.

[144] Gude, MR, Prolongo, SG, and Ureña, A. "Adhesive bonding of carbon fibre/epoxy laminates: Correlation between surface and mechanical properties". In: *Surface and Coatings Technology* 207 (2012), pp. 602–607.

[145] Zaldivar, Rafael J, Kim, HI, Steckel, GL, Nokes, JP, and Morgan, BA. "Effect of processing parameter changes on the adhesion of plasma-treated carbon fiber reinforced epoxy composites". In: *Journal of Composite Materials* 44.12 (2010), pp. 1435–1453.

[146] Dighton, Chris, Rezai, Amir, Ogin, Stephen L, and Watts, John F. "Atmospheric plasma treatment of CFRP composites to enhance structural bonding investigated using surface analytical techniques". In: *International Journal of Adhesion and Adhesives* 91 (2019), pp. 142–149.

[147] Zaldivar, RJ, Nokes, JP, Patel, DN, Morgan, BA, Steckel, G, and Kim, HI. “Effect of using oxygen, carbon dioxide, and carbon monoxide as active gases in the atmospheric plasma treatment of fiber-reinforced polycyanurate composites”. In: *Journal of applied polymer science* 125.4 (2012), pp. 2510–2520.

[148] Williams, Thomas S, Yu, Hang, Yeh, Po-Ching, Yang, Jenn-Ming, and Hicks, Robert F. “Atmospheric pressure plasma effects on the adhesive bonding properties of stainless steel and epoxy composites”. In: *Journal of Composite Materials* 48.2 (2014), pp. 219–233.

[149] Li, Hao, Liang, Hui, He, Fang, Huang, Yuan, and Wan, Yizao. “Air dielectric barrier discharges plasma surface treatment of three-dimensional braided carbon fiber reinforced epoxy composites”. In: *Surface and Coatings Technology* 203.10-11 (2009), pp. 1317–1321.

[150] Banea, Mariana D and Silva, Lucas FM da. “Adhesively bonded joints in composite materials: an overview”. In: *Proceedings of the Institution of Mechanical Engineers, Part L: Journal of Materials: Design and Applications* 223.1 (2009), pp. 1–18.

[151] Sanchez Serrano, Javier, Ureña, Alejandro, Lazcano Urena, Silvia, and Blanco Varela, Tamara. “New approach to surface preparation for adhesive bonding of aeronautical composites: atmospheric pressure plasma. Studies on the pretreatment lifetime and durability of the bondline”. In: *Composite Interfaces* 22.8 (2015), pp. 731–742.

[152] Adkins, David W and Pipes, R Byron. “End effects in scarf joints”. In: *Composites Science and Technology* 22.3 (1985), pp. 209–221.

[153] Campilho, RDSG, De Moura, MFSF, and Domingues, JJMS. “Stress and failure analyses of scarf repaired CFRP laminates using a cohesive damage model”. In: *Journal of Adhesion science and technology* 21.9 (2007), pp. 855–870.

[154] Bendemra, Hamza, Compston, Paul, and Crothers, Phillip J. “Optimisation study of tapered scarf and stepped-lap joints in composite repair patches”. In: *Composite Structures* 130 (2015), pp. 1–8.

[155] Hayes-Griss, JM, Gunnion, AJ, and Khatibi, A Afaghi. “Damage tolerance investigation of high-performance scarf joints with bondline flaws under various environmental, geometrical and support conditions”.

In: *Composites Part A: Applied Science and Manufacturing* 84 (2016), pp. 246–255.

[156] Hu, FZ and Soutis, C. “Strength prediction of patch-repaired CFRP laminates loaded in compression”. In: *Composites science and technology* 60.7 (2000), pp. 1103–1114.

[157] Yoo, Jae-Seung, Truong, Viet-Hoai, Park, Min-Young, Choi, Jin-Ho, and Kweon, Jin-Hwe. “Parametric study on static and fatigue strength recovery of scarf-patch-repaired composite laminates”. In: *Composite structures* 140 (2016), pp. 417–432.

[158] Darwish, Feras H and Shivakumar, Kunigal N. “Experimental and analytical modeling of scarf repaired composite panels”. In: *Mechanics of Advanced Materials and Structures* 21.3 (2014), pp. 207–212.

[159] Li, Jianfeng, Yan, Ying, Liang, Zudian, and Zhang, Taotao. “Experimental and numerical study of adhesively bonded CFRP scarf-lap joints subjected to tensile loads”. In: *The Journal of Adhesion* 92.1 (2016), pp. 1–17.

[160] Campilho, Raul Duarte Salgueiral Gomes, De Moura, MFSF, Pinto, AMG, Morais, JJL, and Domingues, JJMS. “Modelling the tensile fracture behaviour of CFRP scarf repairs”. In: *Composites Part B: Engineering* 40.2 (2009), pp. 149–157.

[161] Whittingham, B, Baker, AA, Harman, A, and Bitton, D. “Micrographic studies on adhesively bonded scarf repairs to thick composite aircraft structure”. In: *Composites Part A: Applied Science and Manufacturing* 40.9 (2009), pp. 1419–1432.

[162] Wang, CH, Venugopal, Veena, and Peng, L. “Stepped flush repairs for primary composite structures”. In: *The Journal of Adhesion* 91.1-2 (2015), pp. 95–112.

[163] Wang, Chun Hui and Duong, Cong N. *Bonded joints and repairs to composite airframe structures*. Academic Press, 2015.

[164] Gunnion, Andrew J and Herszberg, Israel. “Parametric study of scarf joints in composite structures”. In: *Composite structures* 75.1-4 (2006), pp. 364–376.

[165] ZHANG, Qian, CHENG, Xiaoquan, CHENG, Yujia, LI, Weidong, and HU, Renwei. "Investigation of tensile behavior and influence factors of composite-to-metal 2D-scarf bonded joint". In: *Engineering Structures* 180 (2019), pp. 284–294.

[166] MATTA, Seshadri and RAMJI, M. "Prediction of mechanical behaviour of adhesively bonded CFRP scarf jointed specimen under tensile loading using localised DIC and CZM". In: *International Journal of Adhesion and Adhesives* 89 (2019), pp. 88–108.

[167] HAYES-GRISS, JM, ORIFICI, AC, and KHATIBI, Akbar Afaghi. "An improved progressive failure modelling and damage tolerant design methodology for composite scarf joints with bondline flaws". In: *Composites Part A: Applied Science and Manufacturing* 131 (2020), p. 105776.

[168] LIU, Bin, XU, Fei, FENG, Wei, YAN, Rui, and XIE, Wei. "Experiment and design methods of composite scarf repair for primary-load bearing structures". In: *Composites Part A: Applied Science and Manufacturing* 88 (2016), pp. 27–38.

[169] GOH, JY, GEORGIADIS, Steve, ORIFICI, AC, and WANG, CH. "Effects of bondline flaws on the damage tolerance of composite scarf joints". In: *Composites Part A: Applied Science and Manufacturing* 55 (2013), pp. 110–119.

[170] WANG, Chun H and GUNNION, Andrew J. "On the design methodology of scarf repairs to composite laminates". In: *Composites Science and Technology* 68.1 (2008), pp. 35–46.

[171] KUMAR, SB, SRIDHAR, I, SIVASHANKER, S, OSIYEMI, SO, and BAG, A. "Tensile failure of adhesively bonded CFRP composite scarf joints". In: *Materials Science and Engineering: B* 132.1-2 (2006), pp. 113–120.

[172] VOLKERSEN, Olaf. "Die schubkraftverteilung in leim-, niet-und bolzenverbindungen". In: *Energie und Technik* 5.68 (1953), p. 103.

[173] VOLKERSEN, Olaf. "Die Nietkraftverteilung in zugbeanspruchten Nietverbindungen mit konstanten Laschenquerschnitten". In: *Luftfahrtfor schung* 15 (1938), pp. 41–47.

[174] GOLAND, Ma and REISSNER, Eric. "The stresses in cemented joints". In: (1944).

[175] Apalak, M Kemal and Engin, Aysel. “An investigation on the initiation and propagation of damaged zones in adhesively bonded lap joints”. In: *Journal of adhesion science and technology* 17.14 (2003), pp. 1889–1921.

[176] Apalak, M Kemal and Engin, Aysel. “Effect of adhesive free-end geometry on the initiation and propagation of damaged zones in adhesively bonded lap joints”. In: *Journal of adhesion science and technology* 18.5 (2004), pp. 529–559.

[177] Heslehurst, RB. “Observations in the structural response of adhesive bondline defects”. In: *International journal of adhesion and adhesives* 19.2-3 (1999), pp. 133–154.

[178] Pires, I, Quintino, L, Durodola, JF, and Beevers, A. “Performance of bi-adhesive bonded aluminium lap joints”. In: *International Journal of Adhesion and Adhesives* 23.3 (2003), pp. 215–223.

[179] Chaves, FJ P, Silva, LF M da, and Castro, PMS T de. “Adhesively bonded T-joints in polyvinyl chloride windows”. In: *Proceedings of the Institution of Mechanical Engineers, Part L: Journal of Materials: Design and Applications* 222.3 (2008), pp. 159–174.

[180] Adams, RD, Atkins, RW, Harris, JA, and Kinloch, AJ. “Stress analysis and failure properties of carbon-fibre-reinforced-plastic/steel double-lap joints”. In: *The Journal of Adhesion* 20.1 (1986), pp. 29–53.

[181] Sancaktar, Erol and Nirantar, Prasad. “Increasing strength of single lap joints of metal adherends by taper minimization”. In: *Journal of adhesion science and technology* 17.5 (2003), pp. 655–675.

[182] Ramalho, Gabriel M. F., Lopes, António M., and Silva, Lucas F. M. da. “Structural health monitoring of adhesive joints using Lamb waves: A review”. In: *Structural Control and Health Monitoring* 29.1 (2022), e2849. doi: `https://doi.org/10.1002/stc.2849`. eprint: `https://onlinelibrary.wiley.com/doi/pdf/10.1002/stc.2849`. url: `https://onlinelibrary.wiley.com/doi/abs/10.1002/stc.2849`.

[183] Omairey, Sadik, Jayasree, Nithin, and Kazilas, Mihalis. “Defects and uncertainties of adhesively bonded composite joints”. In: *SN Applied Sciences* 3.9 (2021), p. 769. doi: `https://doi.org/10.1007/s42452-021-04753-8`.

[184] NAGY, Peter B. “Ultrasonic detection of kissing bonds at adhesive interfaces”. In: *Journal of Adhesion Science and Technology* 5.8 (1991), pp. 619–630. DOI: `10.1163/156856191X00521`. URL: `https://doi.org/10.1163/156856191X00521`.

[185] HARDER, Sergej, RÖPER, Florian, GIBHARDT, Dennis, KOERT, Benedikt, and FIEDLER, Bodo. “Strength of scarf-bonded CFRP repairs containing disc-shaped zones of weak bonding considering hot-wet conditioning”. In: *International Journal of Adhesion and Adhesives* 102 (2020), p. 102643. ISSN: 0143-7496. DOI: `https://doi.org/10.1016/j.ijadhadh.2020.102643`. URL: `https://www.sciencedirect.com/science/article/pii/S0143749620301068`.

[186] BROTHERHOOD, C.J., DRINKWATER, B.W., and DIXON, S. “The detectability of kissing bonds in adhesive joints using ultrasonic techniques”. In: *Ultrasonics* 41.7 (2003), pp. 521–529. ISSN: 0041-624X. DOI: `https://doi.org/10.1016/S0041-624X(03)00156-2`. URL: `https://www.sciencedirect.com/science/article/pii/S0041624X03001562`.

[187] BOLL, Benjamin, WILLMANN, Erik, FIEDLER, Bodo, and MEISSNER, Robert. “Weak adhesion detection – enhancing the analysis of vibroacoustic modulation by machine learning”. In: *Composite Structures* 273 (2021). ISSN: 0263-8223. DOI: `10.1016/j.compstruct.2021.114233`.

[188] TIGHE, Rachael C, DULIEU-BARTON, Janice M, and QUINN, Simon. “Identification of kissing defects in adhesive bonds using infrared thermography”. In: *International Journal of Adhesion and Adhesives* 64 (2016), pp. 168–178.

[189] EHRHART, Bastien, ECAULT, Romain, TOUCHARD, Fabienne, BOUSTIE, Michel, BERTHE, Laurent, BOCKENHEIMER, Clemens, and VALESKE, Bernd. “Development of a laser shock adhesion test for the assessment of weak adhesive bonded CFRP structures”. In: *International Journal of Adhesion and Adhesives* 52 (2014), pp. 57–65.

[190] HEIDE-JØRGENSEN, Simon, FREITAS, Sofia Teixeira de, and BUDZIK, Michal K. “On the fracture behaviour of CFRP bonded joints under mode I loading: Effect of supporting carrier and interface contamination”. In: *Composites Science and Technology* 160 (2018), pp. 97–110.

[191] Wetzel, M, Holtmannspötter, J, Gudladt, H-J, and Czarnecki, JV. "Sensitivity of double cantilever beam test to surface contamination and surface pretreatment". In: *International Journal of Adhesion and Adhesives* 46 (2013), pp. 114–121.

[192] David-West, O.s, Amafabia, Daerefa-a, Haritos, George, and Montalvão, Diogo. "A Review of Structural Health Monitoring Techniques as Applied to Composite Structures". In: *SDHM Structural Durability and Health Monitoring* 11 (Feb. 2017), pp. 91–147. doi: 10.3970/sdhm.2017.011.091.

[193] Balageas, Daniel, Fritzen, Claus-Peter, and Güemes, Alfredo. *Structural health monitoring*. Vol. 90. John Wiley & Sons, 2010.

[194] Vijaya Kumar, R.L., Bhat, M.R., and Murthy, C.R.L. "Evaluation of kissing bond in composite adhesive lap joints using digital image correlation: Preliminary studies". In: *International Journal of Adhesion and Adhesives* 42 (2013), pp. 60 –68. issn: 0143-7496. doi: 10.1016/j.ijadhadh.2013.01.004.

[195] Schmutzler, Henrik, Alder, Marko, Kosmann, Nils, Wittich, Hans, and Schulte, Karl. "Degradation monitoring of impact damaged carbon fibre reinforced polymers under fatigue loading with pulse phase thermography". In: *Composites Part B: Engineering* 59 (2014), pp. 221–229. doi: 10.1016/j.compositesb.2013.12.010.

[196] Gostautas, Richard S, Ramirez, Guillermo, Peterman, Robert J, and Meggers, Dave. "Acoustic emission monitoring and analysis of glass fiber-reinforced composites bridge decks". In: *Journal of bridge engineering* 10.6 (2005), pp. 713–721.

[197] De Groot, Peter J, Wijnen, Peter AM, and Janssen, Roger BF. "Real-time frequency determination of acoustic emission for different fracture mechanisms in carbon/epoxy composites". In: *Composites science and technology* 55.4 (1995), pp. 405–412.

[198] Gutkin, R., Green, C. J., Vangrattanachai, S., Pinho, S. T., Robinson, P., and Curtis, P. T. "On acoustic emission for failure investigation in CFRP: Pattern recognition and peak frequency analyses". In: *Mechanical Systems and Signal Processing* 25.4 (May 2011), pp. 1393–1407. issn: 0888-3270. doi: 10.1016/J.YMSSP.2010.11.014.

[199] Loutas, TH, Roulias, D, Pauly, E, and Kostopoulos, V. "The combined use of vibration, acoustic emission and oil debris on-line monitoring towards a more effective condition monitoring of rotating machinery". In: *Mechanical systems and signal processing* 25.4 (2011), pp. 1339–1352.

[200] Buggisch, Christina, Gibhardt, Dennis, Felmet, Nils, Tetzner, Yannick, and Fiedler, Bodo. "Strain sensing in GFRP via fully integrated carbon nanotube epoxy film sensors". In: *Composites Part C: Open Access* 6 (2021). doi: 10.1016/j.jcomc.2021.100191.

[201] Augustin, Till, Karsten, Julian, Kötter, Benedikt, and Fiedler, Bodo. "Health monitoring of scarfed CFRP joints under cyclic loading via electrical resistance measurements using carbon nanotube modified adhesive films". In: *Composites Part A: Applied Science and Manufacturing* 105 (2018), pp. 150–155. issn: 1359-835X. doi: 10.1016/j.compositesa.2017.11.015.

[202] Kupke, M., Schulte, K., and Schüler, R. "Non-destructive testing of FRP by d.c. and a.c. electrical methods". In: *Composites Science and Technology* 61.6 (2001), pp. 837–847. doi: 10.1016/S0266-3538(00)00180-9.

[203] Schulte, K. and Baron, Ch. "Load and failure analyses of CFRP laminates by means of electrical resistivity measurements". In: *Composites Science and Technology* 36.1 (1989), pp. 63–76. doi: 10.1016/S0266-3538(00)00180-9.

[204] Abry, J.C., Bochard, S., Chateauminois, A., Salvia, M., and Giraud, G. "In situ detection of damage in CFRP laminates by electrical resistance measurements". In: *Composites Science and Technology* 59.6 (1999), pp. 925–935. doi: 10.1016/S0266-3538(98)00132-8.

[205] Takahashi, K. and Hahn, H.T. "Towards practical application of electrical resistance change measurement for damage monitoring using an addressable conducting network"." In: *Structural Health Monitoring* 11.3 (2012), pp. 367–377. doi: 10.1177/1475921711424519.

[206] Augustin, Till, Grunert, Danny, Langner, Hauke H., Haverkamp, Vico, and Fiedler, Bodo. "Online monitoring of surface cracks and delaminations in carbon fiber/epoxy composites using silver nanoparticle based ink". In: *Advanced Manufacturing: Polymer & Composites Science* 3.3 (2017), pp. 110–119. doi: 10.1080/20550340.2017.1362508.

[207] Eddib, A.A. and Chung, D.D.L. “First report of capacitance-based self-sensing and in-plane electric permittivity of carbon fiber polymer-matrix composite”. In: *Carbon* 140 (2018), pp. 413–427. doi: 10.1016/j.carbon.2018.08.070.

[208] Buggisch, Christina, Gagani, Abedin, and Fiedler, Bodo. “Capacitance measurements on integrated conductors for detection of matrix cracks in GFRP”. In: *Functional Composite Materials* 2.2 (2021). doi: 10.1186/s42252-020-00013-x.

[209] Abry, J.C., Choi, Y.K., Chateauminois, A., Dalloz, B., Giraud, G., and Salvia, M. “In situ detection of damage in CFRP laminates by electrical resistance measurements”. In: *Composites Science and Technology* 61.6 (2001), pp. 855–864. doi: 10.1016/S0266-3538(00)00181-0.

[210] Karim, M.A., Bae, J.-H., Kam, D.-H., Kim, C., Choi, W.-H., and Park, Y.-D. “Assessment of rivet coating corrosion effect on strength degradation of CFRP/aluminum self-piercing riveted joints”. In: *Surface and Coatings Technology* 393 (2020). doi: 10.1016/j.surfcoat.2020.125726.

[211] He, X., Pearson, I., and Young, K. “Self-pierce riveting for sheet materials: State of the art”. In: *Journal of Materials Processing Technology* 199 (2008), pp. 27–36. doi: 10.1016/j.jmatprotec.2007.10.071.

[212] Mandel, M. and Krüger, L. “Determination of pitting sensitivity of the aluminium alloy EN AW-6060-T6 in a carbon-fibre reinforced plastic/aluminium rivet joint by finite element simulation of the galvanic corrosion process”. In: *Corrosion Science* 73 (2013), pp. 172–180. doi: 10.1016/j.corsci.2013.03.033.

[213] Ofoegbu, S., Ferreira, M., and Zheludkevich, M. “Galvanically Stimulated Degradation of Carbon-Fiber Reinforced Polymer Composites: A Critical Review”. In: *Materials* 12.4 (2019). doi: 10.3390/ma12040651.

[214] Fink, A., Camanho, P.P., and Andrés, J.M. “Hybrid CFRP/titanium bolted joints: Performance assessment and application to a spacecraft payload adaptor”. In: *Composites Science and Technology* 70.2 (2010), pp. 305–317. doi: 10.1016/j.compscitech.2009.11.002.

[215] Kradinov, V. and Madenci E.and Ambur, D.R. “Bolted lap joints of laminates with varying thickness and metallic inserts”. In: *Composite Structures* 68.1 (2005), pp. 75–85. doi: 10.1016/j.compstruct.2004.03.002.

[216] Kradinov, V. and Madenci E.and Ambur, D.R. "Combined in-plane and through-the-thickness analysis for failure prediction of bolted composite joints". In: *Composite Structures* 77.2 (2007), pp. 127–147. doi: 10.1016/j.compstruct.2005.06.008.

[217] Majumder, M., Gangopadhyay, T.K., Chakraborty, A.K., Dasgupta, K., and Bhattacharya, D.K. "Fibre Bragg gratings in structural health monitoring—Present status and applications". In: *Sensors and Actuators A: Physical* 147.1 (2008), pp. 150–164. doi: 10.1016/j.sna.2008.04.008.

[218] Takeda, N. "Characterization of microscopic damage in composite laminates and real-time monitoring by embedded optical fiber sensors". In: *International Journal of Fatigue* 24 (2002), pp. 281–289. doi: 10.1016/S0142-1123(01)00083-4.

[219] Mizutani, T., Okabe, Y., and Takeda, N. "Quantitative evaluation of transverse cracks in carbon fiber reinforced plastic quasi-isotropic laminates with embedded small-diameter fiber Bragg grating sensors". In: *Smart Materials and Structures* 12.6 (2002), 898–903. doi: 10.1088/0964-1726/12/6/006.

[220] Kreuzer, M. *Strain measurement with fiber Bragg grating sensors*. 2006. url: http://www-personal.umich.edu/~bkerkez/courses/cee575/handouts/7fbgs_strainmeasurement_mo.pdf.

[221] Giurgiutiu, V. *Structural health monitoring of aerospace composites*. Amsterdam, Boston, and Heidelberg: Academic Press an imprint of Elsevier, 2016. isbn: 9780124096059.

[222] Wu, T.-T. and Liu, Y.-H. "On the measurement of anisotropic elastic constants of fiber-reinforced composite plate using ultrasonic bulk wave and laser generated Lamb wave". In: *Ultrasonics* 37.6 (1999), pp. 405–412. doi: 10.1016/S0041-624X(99)00025-6.

[223] Kudela, P., Radzienski, M., Fiborek, P., and Wandowski, T. "Elastic constants identification of fibre-reinforced composites by using guided wave dispersion curves and genetic algorithm for improved simulations". In: *Composite Structures* 272 (2021). doi: 10.1016/j.compstruct.2021.114178.

[224] Grimberg, R., Savin, A., Steigmann, R., Stanciu, MD., and Grum, J. "Determination of elastic properties of cfrp using lamb waves resonant spectroscopy". In: *2nd International symposium on NDT in Aaerospace.* 2010, pp. 1–8. URL: `https://www.ndt.net/article/aero2010/papers/we5b1.pdf`.

[225] Ong, W., Rajic, N., Chiu, W., and Rosalie, C. "Determination of the elastic properties of woven composite panels for Lamb wave studies". In: *Composite Structures* 141 (2021), pp. 24–31. DOI: `10.1016/j.compstruct.2015.12.017`.

[226] Diamanti, K. and Soutis, C. "Structural health monitoring techniques for aircraft composite structures". In: *Progress in Aerospace Sciences* 46.8 (2010), pp. 342–352. DOI: `10.1016/j.paerosci.2010.05.001`.

[227] Prager, Jens, Hoever, Carsten, Brekow, Gerhard, and Kreutzbruck, Marc. "Flaw detection with guided waves using phased array technique". In: *Department of Non-destructive Testing, Acoustical and Electrical Methods Division, Federal Institute of Materials Research and Testing, Unter den Eichen* 87 (2010).

[228] Gaal, Mate, Döring, Joachim, Brekow, Gerhard, and Kreutzbruck, Marc. "Detection of flaws with lamb waves and air-coupled ultrasound". In: *NDT in progress* (2009).

[229] Cai, J., Qiu, L., Yuan, S., Shi, L., Liu, P., and Liang, D. *Structural Health Monitoring for Composite Materials.* Composites and Their Applications, 2012. ISBN: 978-953-51-0706-4.

[230] Mall, S. "Integrity of graphite/epoxy laminate embedded with piezoelectric sensor/actuator under monotonic and fatigue loads". In: *Smart Materials and Structures* 11.4 (2002). DOI: `10.1088/0964-1726/11/4/307`.

[231] Paget, C.A., Levin, K., and Delebarre, C. "Actuation performance of embedded piezoceramic transducer in mechanically loaded composites". In: *Smart Materials and Structures* 11.6 (2002). DOI: `10.1088/0964-1726/11/6/309`.

[232] Yocum, M., Abramovich, H., Grunwald, A., and Mall, S. "Fully reversed electromechanical fatigue behavior of composite laminate with embedded piezoelectric actuator/sensor". In: *Smart Materials and Structures* 5 (2003). DOI: `10.1088/0964-1726/12/4/307`.

[233] YOO, Sanghyun, KHATIBI, Akbar Afaghi, and KANDARE, Everson. “Durability of Embedded PZTs in Structural Health Monitoring Systems under Cyclic Loading”. In: *Advanced Materials Research* 891-892 (2014), pp. 1255–1260. ISSN: 1662-8985. DOI: `10.4028/www.scientific.net/AMR.891-892.1255`.

[234] WILLBERG, Christian, MOOK, Gerhard, GABBERT, Ulrich, and POHL, Jürgen. “The phenomenon of continuous mode conversion of Lamb waves in CFRP plates”. In: *Key Engineering Materials* 518 (2012), pp. 364–374.

[235] CIANG, Chia Chen, LEE, Jung-Ryul, and BANG, Hyung-Joon. “Structural health monitoring for a wind turbine system: a review of damage detection methods”. In: *Measurement science and technology* 19.12 (2008), p. 122001.

[236] WU, Datong and BUSSE, Gerd. “Evaluation non destructive de materiaux par thermographie a detection synchrone”. In: *Revue Generale de Thermique* 8.37 (1998), pp. 693–703.

[237] WITTEL, Falk, KRÖPLIN, Bernd, and BUSSE, Gerd. *Damage and its Evolution in Fiber Composite Materials: Simulation and Non-Destructive Evaluation.* Oct. 2006. ISBN: 978-3930683901.

[238] RIEGERT, G, ZWESCHPER, Th, DILLENZ, A, and BUSSE, G. “Wirbelstromangeregte Lockin-Thermografie–Prinzip und Anwendungen”. In: *DGZfP Dach-Jahrestagung* (2004).

[239] MENNER, Ph, SPIESSBERGER, Christian, GLEITER, Andreas, and BUSSE, Gerd. “Aerospace applications of lockin thermography with optical, ultrasonic and inductive excitation”. In: *AIP Conference Proceedings.* Vol. 1211. 1. American Institute of Physics. 2010, pp. 525–532.

[240] SPIESSBERGER, Christian, ZWESCHPER, Thomas, and DILLENZ, Alexander. “Rissprüfung mittels aktiver Thermografieverfahren: Induktions-und Ultraschallanregung im Vergleich”. In: *Thermographie-Kolloquium.* 2011.

[241] DONSKOY, Dimitri, EKIMOV, Alexander, and SUTIN, Alexander. “Characterization of bonding quality of composites with the nonlinear modulation method”. In: *The Journal of the Acoustical Society of America* 105.2 (1999), pp. 954–954.

[242] SUTIN, Alexander M and DONSKOY, Dimitri M. “Nonlinear vibro-acoustic nondestructive testing technique”. In: *Nondestructive Characterization of Materials VIII.* Springer, 1998, pp. 133–138.

[243] Donskoy, Dimitri M and Sutin, Alexander M. "Vibro-acoustic modulation nondestructive evaluation technique". In: *Journal of intelligent material systems and structures* 9.9 (1998), pp. 765–771.

[244] Zaitsev, V Yu, Sutin, AM, Belyaeva, I Yu, and Nazarov, VE. "Nonlinear interaction of acoustical waves due to cracks and its possible usage for cracks detection". In: *Journal of Vibration and Control* 1.3 (1995), pp. 335–344.

[245] Burgos, Diego Alexander Tibaduiza, Mujica, Luis Eduardo, and Rodellar, José. *Emerging Design Solutions in Structural Health Monitoring Systems*. IGI Global, 2015.

[246] Carcione, A, Blanloeuil, P, and Veidt, M. "Demodulation technique to identify nonlinear characteristics of vibro-acoustic NDT measurements". In: *Journal of Sound and Vibration* 466 (2020), p. 115014.

[247] Van Den Abeele, KE-A, Johnson, Paul A, and Sutin, Alexander. "Nonlinear elastic wave spectroscopy (NEWS) techniques to discern material damage, part I: nonlinear wave modulation spectroscopy (NWMS)". In: *Journal of Research in Nondestructive Evaluation* 12.1 (2000), pp. 17–30.

[248] Ballad, EM, Vezirov, S Yu, Pfleiderer, K, Solodov, I Yu, and Busse, G. "Nonlinear modulation technique for NDE with air-coupled ultrasound". In: *Ultrasonics* 42.1-9 (2004), pp. 1031–1036.

[249] Dorendorf, Lennart, Lalkovski, Nikolay, and Rutner, Markus. "Physical explanation for vibro-acoustic modulation due to local and global nonlinearities in a structure and its experimental and numerical validation". In: *Journal of Sound and Vibration* 528 (2022). issn: 0022-460X. doi: 10.1016/j.jsv.2022.116885.

[250] Dziedziech, Kajetan, Pieczonka, Lukasz, Kijanka, Piotr, and Staszewski, Wieslaw J. "Enhanced nonlinear crack-wave interactions for structural damage detection based on guided ultrasonic waves". In: *Structural Control and Health Monitoring* 23.8 (2016), pp. 1108–1120.

[251] Donskoy, Dimitri M. and Ramezani, Majid. "Separation of amplitude and frequency modulations in Vibro-Acoustic Modulation nondestructive testing method". In: *Proceedings of Meetings on Acoustics* 34.1 (2018). doi: 10.1121/2.0000831.

[252] Oppermann, Peter, Dorendorf, Lennart, Rutner, Marcus, and Renner, Christian. “Nonlinear modulation with low-power sensor networks using undersampling”. In: *Structural Health Monitoring* (2021). doi: 10.1177/1475921720982885.

[253] Ramezani, M., Civil, Environmental Stevens Institute of Technology. Department of, and Engineering, Ocean. *Enhancement of Joining Method and Damage Detection Methodology in Structural Materials.* Stevens Institute of Technology, 2018. isbn: 9780438837256.

[254] Hu, H.F., Staszewski, W.J., Hu, N.Q., Jenal, R.B., and Qin, G.J. “Crack detection using nonlinear acoustics and piezoceramic transducers—instantaneous amplitude and frequency analysis”. In: *Smart Materials and Structures* 19.6 (2010). doi: 10.1088/0964-1726/19/6/065017.

[255] Oppermann, Peter, Dorendorf, Lennart, Boll, Benjamin, Gagani, Abedin, Lalkovski, Nikolay, Renner, Christian, Rutner, Marcus, Meissner, Robert, and Fiedler, Bodo. “Towards Structural Health Monitoring using Vibro-Acoustic Modulation in the Real World”. In: *18. GI/ITG KuVS FachGespräch SensorNetze, FGSN 19-20.9. 2019, Magdeburg.* 2019, pp. 21–24. doi: 10.25673/28428.

[256] Duffour, Philippe, Morbidini, Marco, and Cawley, Peter. “A study of the vibro-acoustic modulation technique for the detection of cracks in metals”. In: *The Journal of the Acoustical Society of America* 119.3 (2006), pp. 1463–1475. issn: 0001-4966. doi: 10.1121/1.2161429.

[257] Zagrai, Andrei, Donskoy, Dimitri, Chudnovsky, Alexander, Golovin, Edward, and Agarwala, Vinod S. “Micro/meso scale fatigue damage accumulation monitoring using nonlinear acoustic vibro-modulation measurements”. In: *Testing, reliability, and application of micro-and nano-material systems IV.* Vol. 6175. SPIE. 2006, pp. 22–33.

[258] Dorendorf, Lennart, Lalkovski, Nikolay, Stolz, Ricarda, and Rutner, Marcus. “Zuverlässigkeit der Vibro-Akustischen Modulationsmethode zur Strukturüberwachung von Metallen unter Ermüdungsbeanspruchung und ihr Potenzial für das Bauwesen”. In: *22. DASt-Forschungskolloquium.* Karlsruhe, Deutschland, 2020, pp. 135–139.

[259] Alnutayfat, Abdullah, Sutin, Alexander, and Liu, Dong. “Vibroacoustic Modulation of Wideband Vibrations and Its Possible Application for

Windmill Blade Diagnostics". In: *Int. J. Civ. Environ. Eng.* 17.1 (2023), pp. 31–36.

[260] LIM, Hyung Jin and SOHN, Hoon. "Necessary conditions for nonlinear ultrasonic modulation generation given a localized fatigue crack in a plate-like structure". In: *Materials* 10.3 (2017), p. 248.

[261] POLIMENO, Umberto and MEO, Michele. "Understanding the effect of boundary conditions on damage identification process when using non-linear elastic wave spectroscopy methods". In: *International Journal of Non-Linear Mechanics* 43.3 (2008), pp. 187–193.

[262] ZAITSEV, Vladimir and SAS, Paul. "Nonlinear response of a weakly damaged metal sample: a dissipative modulation mechanism of vibro-acoustic interaction". In: *Journal of Vibration and Control* 6.6 (2000), pp. 803–822.

[263] ZAITSEV, V Yu, GUSEV, V, and CASTAGNEDE, B. "Observation of the "Luxemburg–Gorky effect" for elastic waves". In: *Ultrasonics* 40.1-8 (2002), pp. 627–631.

[264] ZAITSEV, Vladimir, NAZAROV, Veniamin, GUSEV, Vitaly, and CASTAGNEDE, Bernard. "Novel nonlinear-modulation acoustic technique for crack detection". In: *Ndt & e international* 39.3 (2006), pp. 184–194.

[265] SOHN, Hoon, LIM, Hyung Jin, DESIMIO, Martin P, BROWN, Kevin, and DERRISO, Mark. "Nonlinear ultrasonic wave modulation for online fatigue crack detection". In: *Journal of Sound and Vibration* 333.5 (2014), pp. 1473–1484.

[266] MIRÓ, Marina, EIRAS, Jesús N, POVEDA, P, CLIMENT, Miguel-Ángel, and RAMIS, J. "Detecting cracks due to steel corrosion in reinforced cement mortar using intermodulation generation of ultrasonic waves". In: *Construction and Building Materials* 286 (2021), p. 122915.

[267] PIECZONKA, L, ZIETEK, L, KLEPKA, A, STASZEWSKI, WJ, AYMERICH, F, and UHL, T. "Damage imaging in composites using nonlinear vibro-acoustic wave modulations". In: *Structural Control and Health Monitoring* 25.2 (2018), e2063.

[268] LIU, Peipei, SOHN, Hoon, and JEON, Ikgeun. "Nonlinear spectral correlation for fatigue crack detection under noisy environments". In: *Journal of Sound and Vibration* 400 (2017), pp. 305–316.

[269] Chen, X.J., Kim, J.-Y., Kurtis, K.E., Qu, J., Shen, C.W., and Jacobs, L.J. “Characterization of progressive microcracking in Portland cement mortar using nonlinear ultrasonics”. In: *NDT & E International* 41.2 (2008), pp. 112–118. issn: 0963-8695. doi: `https://doi.org/10.1016/j.ndteint.2007.08.009`. url: `https://www.sciencedirect.com/science/article/pii/S0963869507001041`.

[270] Duffour, P, Morbidini, M, and Cawley, P. “Comparison between a type of vibro-acoustic modulation and damping measurement as NDT techniques”. In: *NDT & E International* 39.2 (2006), pp. 123–131.

[271] Donskoy, Dmitri, Ekimov, Alexander, Luzzato, Emile, Lottiaux, Jean-Louis, Stoupin, Stanislav, and Zagrai, Andrei. “N-scan: New vibromodulation system for detection and monitoring of cracks and other contact-type defects”. In: *Smart Structures and Materials 2003: Smart Systems and Nondestructive Evaluation for Civil Infrastructures.* Vol. 5057. SPIE. 2003, pp. 400–409.

[272] Pandey, Shashikant and Amarnath, Muniyappa. “Applications of vibro-acoustic measurement and analysis in conjunction with tribological parameters to assess surface fatigue wear developed in the roller-bearing system”. In: *Proceedings of the Institution of Mechanical Engineers, Part J: Journal of Engineering Tribology* 235.10 (2021), pp. 2034–2055.

[273] Ramamurthy, Sundar, Krousgrill, Charles M, and Sadeghi, Farshid. “Vibration in Grease Lubricated Bearing Systems©”. In: *Tribology & lubrication technology* 67.8 (2011), p. 50.

[274] Lee, Sang-Kwon and Amarnath, M. “Experimental investigations to establish correlation between stribeck curve, specific film thickness and statistical parameters of vibration and sound signals in a spur gear system”. In: *Journal of Vibration and Control* 22.6 (2016), pp. 1667–1681.

[275] Amarnath, M and Lee, Sang-Kwon. “Assessment of surface contact fatigue failure in a spur geared system based on the tribological and vibration parameter analysis”. In: *Measurement* 76 (2015), pp. 32–44.

[276] Amarnath, M, Sujatha, C, and Swarnamani, S. “Experimental studies on the effects of reduction in gear tooth stiffness and lubricant film thickness in a spur geared system”. In: *Tribology international* 42.2 (2009), pp. 340–352.

[277] Solvay. “Technical data sheet - FM®300-2 film adhesive”. In: (2011).

[278] *ASTM D7136-M, Test method for measuring the damage resistance of a fiber-reinforced polymer matrix composite to a drop-weight impact event.* Norm. 2020.

[279] Bosbach, Björn, Ohle, Christoph, and Fiedler, Bodo. “Structural health monitoring of fibre metal laminates under mode I and II loading”. In: *Composites Part A: Applied Science and Manufacturing* 107 (2018), pp. 471–478.

[280] Tiedemann, Tobias, Chen, Florian, and Fiedler, Bodo. “New method for crack length determination in low-temperature DCB tests based on electrical capacitance”. In: *Proceedings of the 9th International Conference on Fracture of Polymers, Composites and Adhesives.* 2024.

[281] 527-4, DIN EN ISO. *Plastics - Determination of tensile properties - Part 4: Test conditions for isotropic and anisotropic fibre-reinforced plastic composites.* DIN EN ISO, 1997.

[282] ASTM D5766 / D5766M-11. *Standard Test Method for Open-Hole Tensile Strength of Polymer Matrix Composite Laminates.* ASTM, 2018. doi: 10.1520/D5766_D5766M-11.

[283] Richardson, MOW and Wisheart, MJ. “Review of low-velocity impact properties of composite materials”. In: *Composites Part A: Applied Science and Manufacturing* 27.12 (1996), pp. 1123–1131.

[284] Sjoblom, P. O., Hartness, J. T., and Cordel, T. M. “On Low-Velocity Impact Testing of Composite Materials”. In: *Journal of Composite Materials* 22.1 (1988). issn: 0021-9983. doi: 10.1177/002199838802200103.

[285] D6484, ASTM. *Open-Hole Compressive Strength of Polymer Matrix Composite Laminates.* ASTM, 1999. doi: 10.1520/D6484_D6484M-20.

[286] Donskoy, Dimitri M. “Nonlinear acoustic interaction on contact interfaces and its use for nondestructive testing”. In: *Encyclopedia of Structural Health Monitoring* (2009). doi: 10.1002/9780470061626.shm014.

[287] Alam, P., Mamalis, D., Robert, C., Floreani, C., and Ó Brádaigh, C.M. “The fatigue of carbon fibre reinforced plastics - A review”. In: *Composites Part B: Engineering* 166 (2019), pp. 555–579.

[288] Smarsly, K., Worm, M., Dragos, K., Peralta Abadía, J.J., Wenner, M., and Hahn, O. “Mobile structural health monitoring using quadruped robots”. In: *Health Monitoring of Structural and Biological Systems XVI,SPIE* 12048 (2022), pp. 404–417. doi: 10.1049/iet-rpg.2013.0229.

[289] Devriendt, C., Weijtjens, W., El-Kafafy, M., and De Sitter, G. “Monitoring resonant frequencies and damping values of an offshore wind turbine in parked conditions”. In: *Renewable Power Generation, IET* 8.4 (2014), pp. 433–441. doi: 10.1049/iet-rpg.2013.0229.

[290] Doolan, C. J., Moreau, D. J., and Brooks, L. A. “Wind turbine noise mechanisms and some concepts for its control”. In: *Acoustics Australia* 40.1 (2012).

[291] Knoll, J.B., Riecken, B.T., Kosmann, N., Chandrasekaran, S., Schulte, K., and Fiedler, B. “The effect of carbon nanoparticles on the fatigue performance of carbon fibre reinforced epoxy”. In: *Composites Part A: Applied Science and Manufacturing* 67 (2014). doi: 10.1016/j.compositesa.2014.08.022.

[292] Reifsnider, L.K., Schulte, K., and Duke, L.C. “Long-term fatigue behavior of composite materials”. In: *O’Brien TK* (1983), pp. 136–9.

[293] Jamison, R.D., Schulte, K., Reifsnider, L.K., and Stinchcomb, W.W. “Characterization and analysis of damage mechanisms in tension-tension fatigue of graphite/epoxy laminates”. In: *Effects of defects in composite materials* (1984), pp. 21–55.

[294] Quaresimin, M. and Carraro, P.A. “Damage initiation and evolution in glass/epoxy tubes subjected to combined tension–torsion fatigue loading”. In: *International Journal of Fatigue* 63 (2014), pp. 25–35. doi: 10.1016/j.ijfatigue.2014.01.002.

[295] Donskoy, Dimitri and Liu, Dong. “Vibro-acoustic modulation baseline-free non-destructive testing”. In: *Journal of Sound and Vibration* 492 (Feb. 2021), p. 115808. issn: 0022-460X. doi: 10.1016/J.JSV.2020.115808.

[296] Hexcel. *HeyPly M21: Epoxy Matrix (180 °C curing matrix.* Datasheet, 2016.

[297] Boll, Benjamin, Dorendorf, Lennart, Oppermann, Peter, Willmann, Erik, Fieder, Bodo, Renner, Bernd-christian, Rutner, Marcus, and Horst, Robert. "Synthetic generation of vibroacoustic modulation signals for structural health monitoring applications". In: *Mech. Syst. Signal Process.* (2023), pp. 1–18.

[298] Groot, Peter J. de, Wijnen, Peter A.M., and Janssen, Roger B.F. "Real-time frequency determination of acoustic emission for different fracture mechanisms in carbon/epoxy composites". In: *Composites Science and Technology* 55.4 (Jan. 1995), pp. 405–412. issn: 0266-3538. doi: 10.1016/0266-3538(95)00121-2.

[299] Ramirez-Jimenez, C. R., Papadakis, N., Reynolds, N., Gan, T. H., Purnell, P., and Pharaoh, M. "Identification of failure modes in glass/polypropylene composites by means of the primary frequency content of the acoustic emission event". In: *Composites Science and Technology* 64.12 (Sept. 2004), pp. 1819–1827. issn: 0266-3538. doi: 10.1016/J.COMPSCITECH.2004.01.008.

[300] Kötter, Benedikt, Endres, Janina, Körbelin, Johann, Bittner, Florian, Endres, Hans-Josef, and Fiedler, Bodo. "Fatigue and fatigue after impact behaviour of Thin- and Thick-Ply composites observed by computed tomography". In: *Composites Part C: Open Access* 5 (2021). doi: 10.1016/j.jcomc.2021.100139.

[301] Philippidis, Theodore P. and Vassilopoulos, Anastasios P. "Life prediction methodology for GFRP laminates under spectrum loading". In: *Composites Part A: Applied Science and Manufacturing* 35.6 (2004), pp. 657–666. issn: 1359-835X. doi: https://doi.org/10.1016/j.compositesa.2004.02.009. url: https://www.sciencedirect.com/science/article/pii/S1359835X04000466.

[302] Bendouba, Mostefa, Aid, Abdelkrim, and Benguediab, Mohamed. "Fatigue life prediction of composite under two block loading". In: *Engineering, Technology & Applied Science Research* 4.1 (2014), pp. 587–590.

[303] Batsoulas, Nikolaos D. and Giannopoulos, Georgios I. "Cumulative Fatigue Damage of Composite Laminates: Engineering Rule and Life Prediction Aspect". In: *Materials* 16.8 (2023). issn: 1996-1944. doi: 10.3390/ma16083271. url: https://www.mdpi.com/1996-1944/16/8/3271.

[304] Saito, H., Morita, M., Kawabe, K., Kanesaki, M., Takeuchi, H., Tanaka, M., and Kimpara, I. "Effect of ply-thickness on impact damage morphology in CFRP laminates". In: *Journal of Reinforced Plastics and Composites* 30.13 (2011), pp. 1097–1106. issn: 0731-6844. doi: 10.1177/0731684411416532.

[305] Chen, Bo Yang, Soh, Su Kiat, Lee, Heow Pueh, Tay, Tong Earn, and Tan, Vincent B.C. "A vibro-acoustic modulation method for the detection of delamination and kissing bond in composites". In: *J. Compos. Mater.* 50.22 (2016), pp. 3089–3104. issn: 1530793X. doi: 10.1177/0021998315615652.

[306] Ehrlich, Paul, Amborski, LE, and Burton, RL. "Dielectric properties of teflon from room temperature to 314 C and from frequencies of 102 to 105 c/s". In: *J. Res. Nat. Bur. Stand* 51 (1953), pp. 185–188.

7 Appendix

7.1 Initial measurements of UD specimens

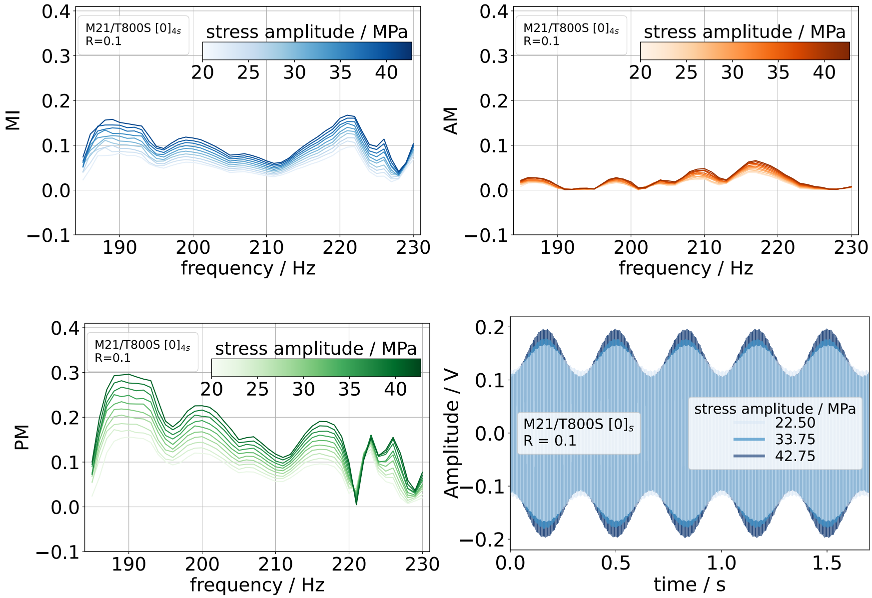

Figure G.1: Vibro-acoustic response signal of an UD specimen with varied stress amplitude and mean stress with constant stress ratio R=0.1 – top left: as MI; top right: as AM; bottom left: as PM in the frequency domain and bottom right: as modulated signal in time domain.

7.2 Fatigue measurements of unnotched QI specimens

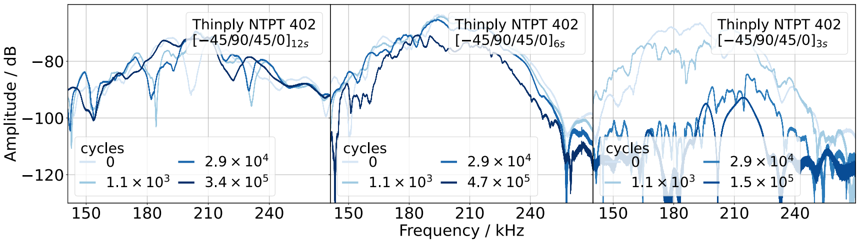

Figure G.2: Chirp signal of CFRP thinply laminates at 3 Hz after initial and continuous fatigue measurement with fibre areal weight of 30, 60, 120 g/m^2 (from left to right).

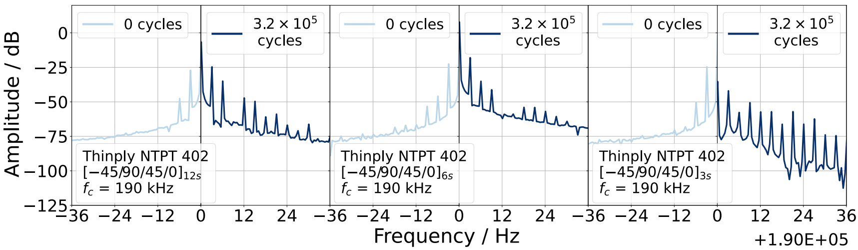

Figure G.3: FFT signal of CFRP thinply laminates at 3 Hz after initial and continuous fatigue measurement with fibre areal weight of 30, 60, 120 g/m^2 (from left to right). The FFT signal displays negative (left half-image) and positive sidebands (right half-image), which illustrate the damage propagation from the initial to continous number of fatigue cycles.

7.3 Fatigue measurements of notched QI specimens

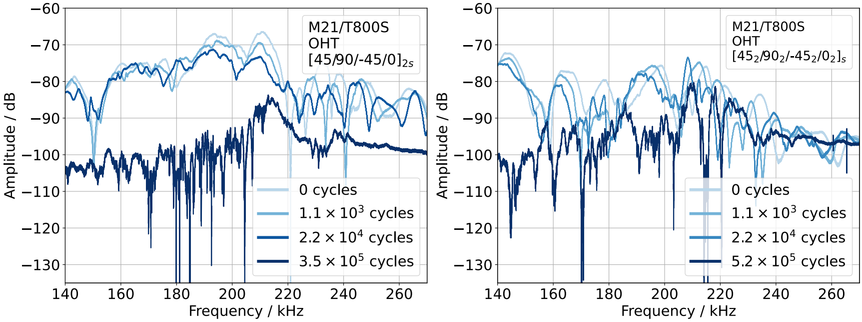

Figure G.4: Chirp signal of CFRP OHT laminates at 3 Hz after initial and continuous fatigue measurement with sub- and ply-scaling configuration (from left to right).

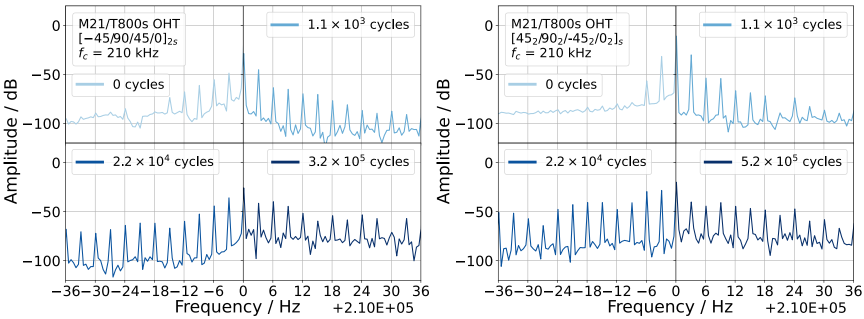

Figure G.5: FFT signal of CFRP OHT laminates at 3 Hz after initial and continuous fatigue measurement with sub- and ply-scaling configuration (from left to right). The areas of the negative and positive sidebands are shown in the respective quadrants according to the associated fatigue cycles.

7.4 Fatigue measurements of FAI Thinply specimens

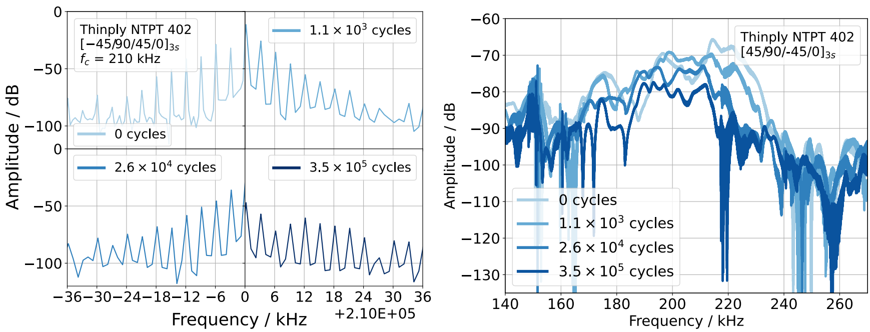

Figure G.6: FFT signal (left) and chirp signal (right) of a CFRP thinply laminate with 120 g/m^2 fibre areal weight and 5 J impact energy at 210 kHz carrier frequency and 3 Hz pump frequency after initial and after continuous fatigue cycles. The areas of the negative and positive sidebands are shown in the respective quadrants according to the associated fatigue cycles.

7.5 Fatigue measurements of adhesive bonded CFRP structures

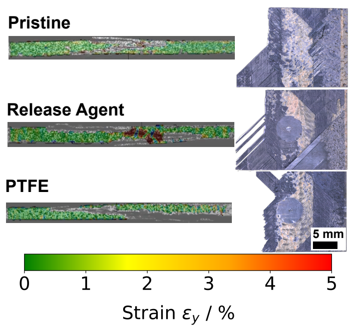

Figure G.7: Comparison of fracture patterns and DIC images of the bonded CFRP specimens with Sc configurations after final failure at fatigue test. From top to bottom, the figure displays a pristine specimen, as well as specimens with PTFE and release agent defects.